Conjugated Polymer-Based Organic Solar Cells

3 AUTHORS, INCLUDING:

Serap Günes

Yildiz Technical University

38 PUBLICATIONS   **5,147** CITATIONS

SEE PROFILE

11
Conjugated Polymer-Based Organic Solar Cells

Gilles Dennler, Niyazi Serdar Sariciftci, and Christoph J. Brabec

11.1
Introduction

11.1.1
Photovoltaics

Photovoltaics (PVs) consists of the harvesting of energy from sunlight and its conversion into electrical power. This technology is being increasingly recognized as one of the key components in our future global energy scenario. Limited fossil fuel resources and steadily increasing costs of supplying fossil fuels to the market induce a natural limit where renewable energies will begin to kick in as major energy suppliers. In addition, the detrimental long-term effects of CO_2 and other emissions from burning fossil fuels into our atmosphere underscore the multiple benefits of developing renewable energy resources and commercializing them.

The worldwide photovoltaics (PV) industry reached a cell/module production of 1200 MW_p in 2004, exhibiting an average annual growth of 40% over the last 5 years [1]. The same year, this market recorded a spectacular increase of 58.5% (US\$ 5.8 billion), making the industry one of the fastest growing worldwide at present. As shown in Fig. 11.1, this development is not only in Japan, but also in Europe and the USA. Besides, most Japanese, USA and European forecasts seem to agree on one point: This trend is expected to last at least for the next 30 years to come [1]. A significant capacity of about 200 GW_p is forecast to be operational around the globe in 2020. This number is the equivalent of 200 state-of-the-art nuclear power plants.

PV technology is only one of many alternative renewable energies such as wind, biomass, and water. However, though all of these technologies are expected to contribute significantly to the world's energy supply in the next century, PVs possesses three key properties which make it unique:

<QA> 1. Figure legend; 11.1.1 / Fig. 11.1; The worldwide photovoltaic industry / Please define MWp
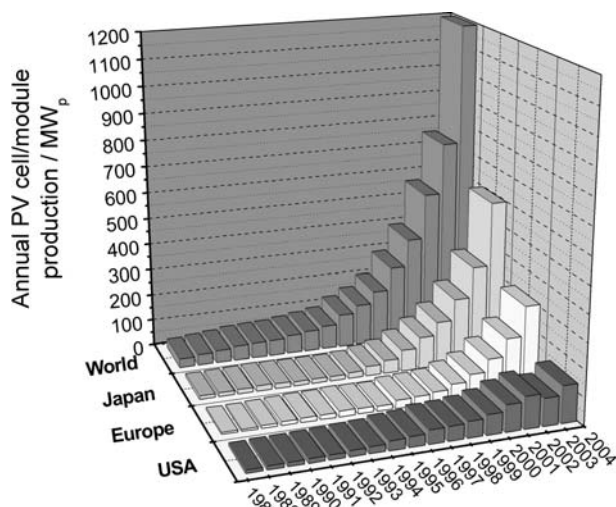
Fig. 11.1 Annual photovoltaic (PV) cell/module production from 1988 to 2003 (data from [1]), expressed in MW_p.

<QA> 1. Figure legend; 11.1.1 / Fig. 11.1; The worldwide photo-voltaic industry / Please define MWp

- It directly generates electricity, without the need of generators.
- It is an outstanding flexible technology, supplying electrical power in form of portable modules in the milliwatt scale up to entire power plants with peak capacities in the multiple megawatt regime.
- It is the only renewable energy which can be customized, i.e., handled by individuals.

Thus, it is not surprising that PVs is becoming increasingly recognized as part of the solution to the growing energy challenge and an essential component of future global energy production. The big drawback of current PV technologies is their rather high production cost. Currently, electricity from PVs is about 10 times more expensive than energy from fossil fuels and about 3 times more expensive than other renewable energies. Provided that PVs can be made truly economically competitive with fossil fuels, large-scale manufacturing of these devices offers a pathway to a sustainable energy source that could supply up to 20% of our energy needs.

11.1.2
Technology Overview and Forecasts

To address the economics of PV technology, Martin Green from University of New South Wales originally developed the concept of third-generation PVs (Fig. 11.2). This third generation currently comprises two categories. The first one (IIIa) consists of novel approaches that strive to achieve very high efficiencies. Key words for
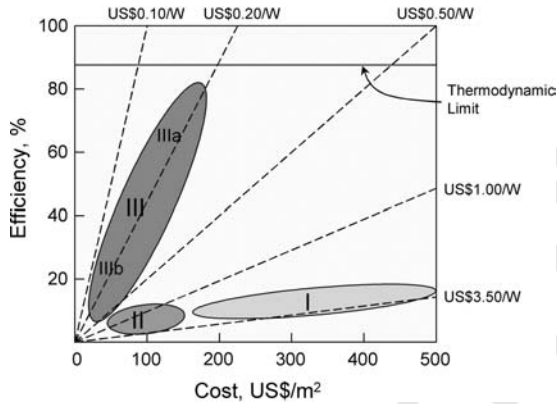
Fig. 11.2 Overview of the different PV technologies currently followed: first generation (I) are thick film Si devices and second generation (II) are inorganic thin-film technologies; third-generation technologies (III) are described in more detail in the text.

IIIa technologies are hot carriers, multiple electron–hole pair creation, concentrator cells and thermophotonics. All these concepts have theoretical maximum efficiencies well above the 31% limit for single-junction devices. Hence, these high-efficiency cells can afford higher costs and still show a favorable €/Wp balance. In the second type of third-generation device (IIIb), the goal is exactly opposite. A low €/Wp balance would be achieved via moderate efficiencies (15–20%), but at very low cost. This will require inexpensive semiconductors materials, packaging solutions, and production processes (low-temperature atmospheric routes), as well as high fabrication throughput, low or no investment into the production facility and a production-on-demand scenario.

Several promising technologies for these third-generation low-cost PVs are currently available and grouped under the appellation organic PVs (OPVs). They all have in common that at least one of the key functionalities for PV energy conversion is handled by organic semiconductor or conductor.

The most prominent and mature technology is that of the so-called dye-sensitized nanostructured oxide solar cells (DSSCs) [2]. DSSCs use an organic dye to absorb light and undergo a rapid electron transfer to a nanostructured oxide such as anatase TiO_2. The mesoscopic structure of the TiO_2 allows processing of rather thick, nanoporous films. At an active-layer thickness of several micrometers, the whole of the light is absorbed and these devices reach external quantum efficiencies of over 80%. The hole transport is achieved by a redox couple, such as iodide/triiodide (I^-/I^{3-}). There is a lot of interest in replacing the liquid electrolyte by a solid-state hole transporter; however, current progress is limited by the transport properties of the solid-state system.

Solid-state bulk-heterojunction devices (BHJs) are also one of the very successful recent technologies. Though several different bulk-heterojunction approaches are investigated, those employing a conjugated polymer such as

<QA>18. 11.1.2
Hence, these high-efficiency / Does this mean cost–power balance? I think it is better if you use that phrase, if so.

poly(3-hexylthiophene) as the donor and a fullerene derivative as the acceptor are among the most interesting to date. The closest hybrid alternatives to the fully organic BHJ are organic–inorganic composites. These devices combine a light-absorbing conjugated polymer as the donor and hole transporter with a nanostructured, inorganic semiconductor such as CdSe, CdS, PbS, TiO_2 or ZnO as the acceptor and electron transporter (see Section 11.5.3). Depending on the choice of semiconductor, both components can efficiently absorb light, and the band gap of the nanocrystals can be tuned by growing them to different sizes.

One step further are hybrid BHJs, where the electron acceptor and transporter is grown in self-organized structures on a substrate, filled up with conjugated polymers as hole transporters. These cells work similarly to the bulk heterojunctions; however, the gross morphology of the mixture is determined by that of the nanostructured oxide. It should be noted that this approach is relatively close to the solid-state DSSC devices (see Section 11.5.3).

Though all these technologies are under active development, none of them has achieved full commercialization yet. Comparison of their respective performances and forecasts is not always objective. Such forecasts may only reflect the current situation which is frequently a mirror of the man-years and development-dollars invested in a technology program. Nevertheless, it is sometimes
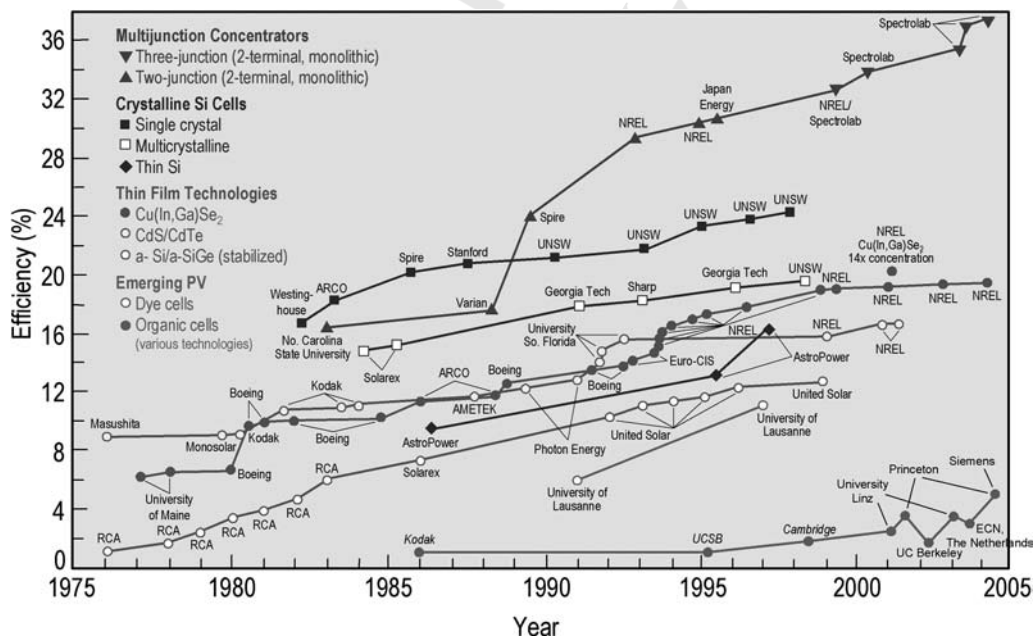

Fig. 11.3 Forecast for prominent PV technologies. Organic bulk-heterojunction devices (BHJs) and dye-sensitized nanostructured oxide solar cells (DSSCs) data have been added to this forecast by ● AQ2 NREL.

<QA>2. Figure legend Fig. 11.3 / Please define NREL, ARCO, UNSW, AME-TEK.

helpful to use these forecasts for orientation as to where a technology has come from, as depicted in Fig. 11.3.

11.1.3
Motivation for OPV

The strongest argument for the third-generation organic technologies is certainly their promise for ultralow costs. The vision of PV elements based on thin plastic carriers, manufactured by printing and coating techniques from reel to reel, and packaged by lamination techniques is not only intriguing, but highly attractive from an economic standpoint. To achieve such goals, high-volume production technologies for large area coating must be applied to a low-cost material class. Solution-processable organic and inorganic semiconductors have a high potential to fulfil these requirements. Flexible chemical tailoring allows the design of organic semiconductors with the desired properties, and printing or coating techniques like screen, inkjet, offset or flexo printing are being established for semiconducting polymers today, driven by display or general electronic demands (see Section 11.5.1). Altogether, OPVs possess many attractive features, among them:

- the potential to be flexible and semitransparent,
- the potential to be manufactured in a continuous printing process,
- large-area-coating potential,
- easy integration in different devices,
- significant cost reduction compared to traditional solutions,
- substantial ecological and economic advantages.

Though these features are beneficial for commercialization, OPVs has to fulfil the basic requirements for renewable energy production, like its classical counterpart. In the energy market the competitive position of each solar technology is mainly determined by the three factors: efficiency, lifetime, and costs (per Wp). The potential of OPVs must be judged by these key figures.
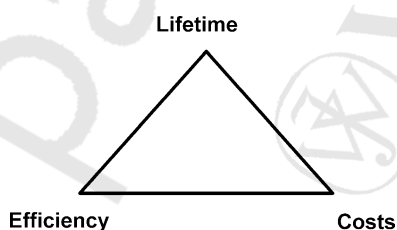

Fig. 11.4 The critical triangle for PVs. Organic solar cells have to fulfil all requirements simultaneously, namely lifetime, efficiency and costs, otherwise they will be limited to niche markets. Additional criteria like semi-transparency, flexibility or very short breakeven times are beneficial, but cannot make up for a significant deficiency in one of the triangle's corners.

It is more likely that once OPVs realize a certain technological profile, there will be substantial freedom for commercialization. Figure 11.4 summarizes the restrictions within which OPVs can be commercialized. The important message of this figure is that successful commercialization can be realized only if all three technology-driving aspects are fulfilled simultaneously. A product development succeeding in only two aspects e.g., competitive costs and reasonable efficiency, will only be able to address niche markets unless the third parameter, in that case, lifetime, is also optimized.

In this contribution, we will focus on the science and technology of conjugated-polymer/fullerene BHJs as a highly promising technology for third-generation PVs. However, other OPV approaches will be briefly discussed in Section 11.5.3.

11.2
Conjugated Polymers as Photoexcited Donors

An important difference between inorganic and organic solar cells lies in the nature of the primary photoexcited state [3]. In the former, the absorption of photons leads directly to the creation of free electrons and holes at room temperature. The charge carriers can then diffuse and/or drift to their respective collective electrodes.

In organic semiconductors the situation is somewhat different and still the object of strong debate within the scientific community [4]. It is generally accepted that the absorption of a photon induces mainly excitons with binding energies ranging from 0.05 eV up to >1 eV [5]. According to the Onsager theory [6], which can be invoked as a first approximation in organic semiconductors, photoexcited electrons and holes are coulombically bound (excitons) and perform a Brownian random walk [5, 7]. Once excitons have been created by the absorption of photons, they can diffuse over a length of approximately 5–15 nm [8–12]. Then they decay either radiatively or nonradiatively. The former route gives rise to luminescence that occurs within 500–800 ps for singlet excitons (fluorescence) and several hundreds of nanoseconds for triplet excitons (phosphorescence) at room temperature.

For PV purposes, excitons have to be separated into free charge carriers before they decay. That can be achieved by several different ways:

- Dissociation by trap sites in the bulk of material [3].
- Dissociation by an externally applied electric field [13].
- The "hot exciton" [14] dissociation: the excess energy of the photons can quickly be distributed over the conjugation segment of the polymer leading to local temperatures (thermal bath) high enough for a very short period of time (in the femtosecond range [15]) to provide the activation energy for exciton dissociation.
- Exciton dissociation at the discontinuous potential drops at the interfaces between donors and acceptors as well as between semiconductors and metals [16].

Independently, the Dupont company [17], Santa Barbara and Osaka groups reported studies on the photophysics of mixture and bilayers of conjugated polymers with fullerenes [18–26]. The experiments clearly evidenced that when an exciton reaches the interface between a conjugated polymer (donor) and a C_{60}-based material (acceptor) an ultrafast electron transfer occurs from the lowest unoccupied molecular orbital (LUMO) of the donor to the lower lying LUMO of the acceptor, leaving a hole on the highest occupied molecular orbital (HOMO) of the donor. Thus, electrons and holes are separated, and the free charge carriers produced can diffuse in their respective environments during their life time (up to a millisecond). The forward electron transfer was observed to happen within 45 fs [27]; that is much faster than any competing relaxation processes. Therefore its efficiency is about 100%.

11.2.1
Optical Properties

11.2.1.1   Linear Optical Properties
Figure 11.5 shows the optical absorption spectrum of a poly[2-methoxy, 5-(2′-ethyl-hexyloxy)-p-phenylenevinylene) (MEH-PPV)/C_{60} film with different C_{60} concentrations as well as the optical absorption spectrum of the components alone [28]. The spectrum obtained with the blend displays a peak at 2.5 eV, identified as the π–π^* absorption of MEH-PPV and another one at 3.75 eV, identified as the first dipole-allowed transition in C_{60}. Hence the spectrum is a simple superposition of the two components. Furthermore, the positions of the absorption maxima of the single components in the composite are not shifted compared to the pristine materials. Thus, there is no indication of states below the π–π^* gap of the conjugated polymer that might arise from ground-state interactions like doping.

Figure 11.6 shows the intensity of the photoluminescence (PL) as a function of the fullerene concentration in poly[2-methoxy-5-(3′,7′-dimethyloctyloxy)-1,4-phenylenevinylene] (MDMO-PPV)/(1-(3-methoxycarbonyl) propyl-1-phenyl [6,6]C_{61} (PCBM) composites. The luminescence quenching is found to start with fullerene concentrations as low as 0.1 mol%. This indicates that excitons can reach the donor–acceptor interface within their lifetime, even at such low acceptor concentration. The inset in Fig. 11.6 shows the luminescence spectrum of MEH-PPV:C_{60} composites compared to MEH-PPV alone [18]. The strong PL of MEH-PPV is quenched by a factor in excess of 10^3, but no significant changes in the shape of the spectrum are observed. Moreover, the luminescence decay time is reduced from $\tau = 550$ ps to $\tau \ll 60$ ps (the instrumental resolution), indicating the existence of a rapid quenching process, e.g., subpicosecond electron transfer.
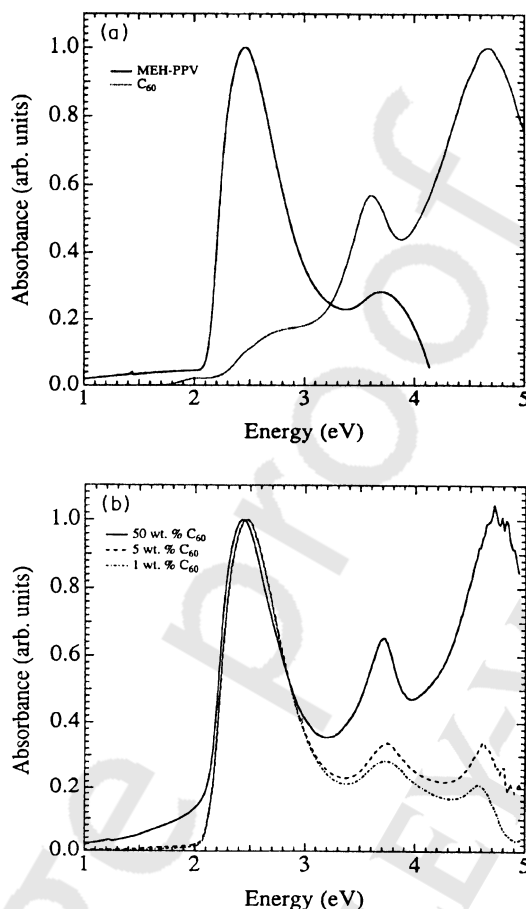
Fig. 11.5 (a) Optical absorption spectra of poly[2-methoxy, 5-(2′-ethyl-hexyl-oxy)-*p*-phenylenevinylene) (*MEH-PPV*) and C_{60}. (b) Optical absorption spectra of MEH-PPV:C_{60} films with different concentrations of C_{60}. (Reproduced, with permission, from [28]).

11.2.1.2 **Photoinduced Absorption**

The occurrence of luminescence quenching can be explained by various mechanisms: (a) nonradiative relaxation of the excited singlet state to the ground state (thermal heating), (b) energy-transfer, or (c) electron-transfer processes. Since the absorption and luminescence studies demonstrate that the excited state of the conjugated polymers strongly interacts with C_{60}, a comparative spectroscopic study of this excited state is necessary. The first results on the excited-state spectroscopy of these composites originate from near-steady-state photoinduced absorption (PIA) studies. To clearly distinguish the spin multiplicity of the PIA peaks, PIA-detected magnetic resonance experiments were performed [29]. The full spectral range of PIA spectra are displayed in Fig. 11.7. The results
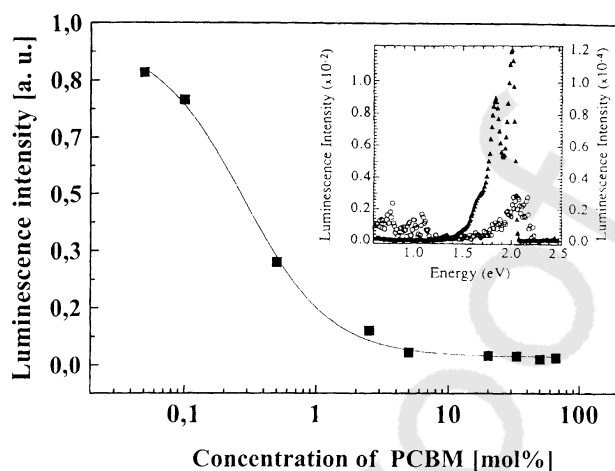
Fig. 11.6 Intensity of the photoluminescence (PL) as a function of the 1-(3-methoxycarbonyl) propyl-1-phenyl$(6,6)C_{61}$ (*PCBM*) concentration in MEH-PPV:PCBM blends. The inset shows the luminescence of pristine MEH-PPV (solid triangles, left-hand axis) and a MEH-PPV:C_{60} blend (open circles, right-hand axis). The inset is adapted from [18].
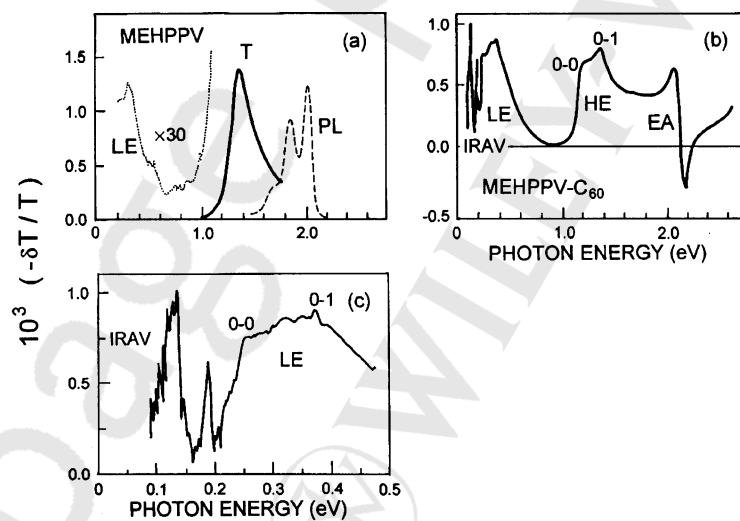

Fig. 11.7 (a) Photoinduced absorption (PIA) and PL spectra of MEH-PPV at 80 K. (b,c) PIA spectra of MEH-PPV:C_{60} at 4 K with argon ion laser at 514.5 nm modulated at 200 Hz. *T* Triplet–triplet absorption, *LE* low-energy band, *HE* high-energy band, *EA* electroabsorption features, *IRAV* infrared activated modes. (Reproduced with permission from [29]).
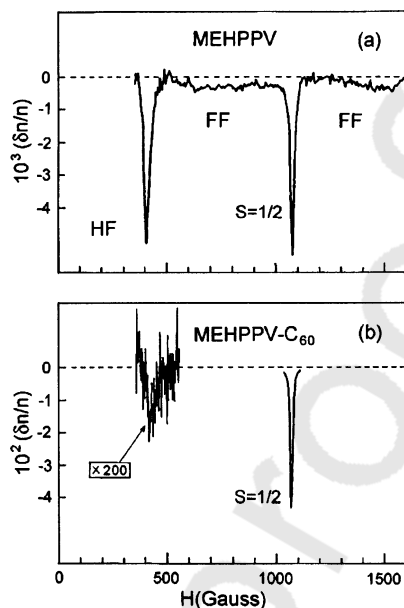
Fig. 11.8 (a) PIA-detected magnetic resonance (ADMR) spectrum of MEH-PPV. Half-field (*HF*) and full-field (*FF*) powder pattern for the triplet ($S=1$) resonance. (b) ADMR spectrum of MEH-PPV : C_{60} composite film. Both spectra were measured at probe energy 1.35 eV, $T=4$ K and 3 GHz resonant microwave frequency. (Reproduced with permission from [29]).

show that the PIA bands centered at about 0.3 eV and 1.1 eV are significant only in the composite material. Pure MEH-PPV shows the single PIA band from the triplet–triplet absorption, as assigned earlier [30]. The PIA of C_{60} is neglected in this comparison because the magnitude of the signal is 10^2 times smaller when photoexcited with 2.5 eV as a result of the very low optical density of C_{60} in this region.

In absorption-detected magnetic resonance studies, the PIA band at 1.35 eV in the pure MEH-PPV shows a strong response at the (forbidden) half-field resonance of spin = 1 ($\Delta m = 2$), indicating triplet character for this PIA band and dominance of the neutral photoexcitations in MEH-PPV (Fig. 11.8). A residual spin = 1/2 response within the pure MEH-PPV shows the presence of photoinduced radicals. Upon adding C_{60}, the triplet signal for the 1.35 eV PIA band is completely quenched. A strong spin = 1/2 signal dominates, indicating charged polarons as photoexcitations on the polymer. This shows that the photoinduced electron transfer occurs on a timescale sufficiently fast to quench the intersystem crossing to the triplet state.

11.2.1.3 **Time-Resolved Photoinduced Studies**

It is still not clearly understood, why the forward electron transfer is so fast while the back-transfer is several orders of magnitude slower. Theoretical models for the photoinduced charge transfer in conjugated-polymer/C_{60} composites have been developed to estimate the time constant of the transfer. A model based on the assumption that the charge transfer is a pair-process of purely electronic origin proposes a transfer rate in the picosecond regime [31]. Approaches taking into account electron–phonon interactions for coupled Su-Schrieffer-Heeger models [32] but neglecting electron–electron interactions indicate that the photoinduced electron transfer should take place between 200 and 300 fs [33].

Subpicosecond PIA studies were employed to demonstrate the speed of the photoinduced electron transfer. Upon addition of C_{60} to poly(3-octylthiophene) (P3OT), the PIA spectrum, decay kinetics, and intensity dependence change
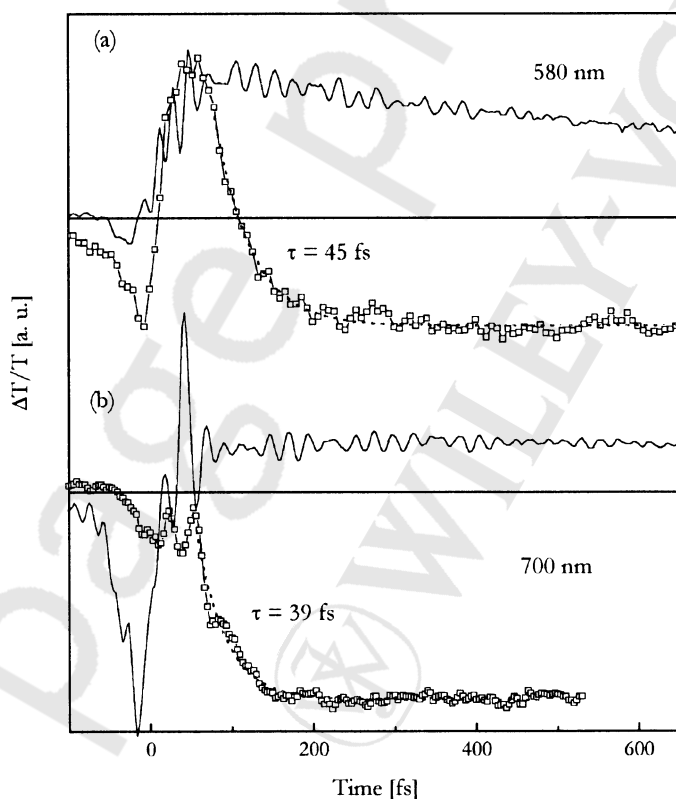
Fig. 11.9 Time resolution of photoinduced charge-transfer transient $\Delta T/T$ for pure poly[2-methoxy-5-(3'7'-dimethyloctyloxy)-1,4-phenylene vinylene] (MDMO-PPV) (solid line) and MDMO-PPV : PCBM (squares) at probe wavelengths of 580 nm and 700 nm. (Reproduced with permission from [35]).

<QA>3. Figure legend Fig. 11.9 / Please define τ

dramatically [34]: 1 ps after photoexcitation by a 100-fs pump pulse at 2.01 eV, charge transfer is observed in P3OT/C_{60} (1%). Similar results were found for MEH-PPV:C_{60} composites. Recently, Brabec et al. reported ultrafast pump–probe measurements performed on MDMO-PPV:PCBM blends [35] with a few optical-cycle laser pulses (5–6 fs) obtained by broadband frequency conversion techniques [36]. Figure 11.9 shows the transient $\Delta T/T$ signal at 580 nm for pure MDMO-PPV and MDMO-PPV:PCBM blends. In the case of pristine-conjugated polymer, the signal rises within 100 fs and decreases in a very slow decay. This phenomenon is related to the PL of the polymer. In the case of the donor–acceptor blend, the same rapid rise is observed but directly followed by a fast exponential decay until the signal stabilizes on negative $\Delta T/T$, indicating PIA of the charge-transferred state. By an exponential fit of the decay, a time constant for the electron-transfer process of 45 ± 3 fs can be calculated [35].

11.2.1.4 Photoinduced Infrared-Activated Modes Studies

In semiconducting, conjugated polymers, the quasi-one-dimensional electronic structure is strongly coupled to the chemical (geometrical) structure. As a result, the nonlinear excitations (solitons, polarons and polaron pairs) are dressed with local structural distortions creating states at energies within the forbidden π–π^* gap. "New" vibrational infrared absorption bands with large intensities [infrared-activated modes (IRAV modes)] are induced by doping and/or photoexcitation. Solitons and polarons can be considered as charged "defects" which break the local symmetry and therefore make Raman modes infrared-active. IRAV doping studies of P3OT [37, 38] showed significant differences among the IRAV bands depending on the doping mechanism (i.e., chemical, electrochemical, photodoping). In the theoretical framework of the model presented by Zerbi et al. [39, 40], the IRAV bands correspond to totally symmetric Raman-active vibrational A_g modes, which couple to the π-electron system along a so-called "effective conjugation coordinate". The charge distribution in the formed polaronic or bipolaronic state causes high dipole moment changes during vibration, thereby breaking the symmetry. In general, in the frequency range 1600–800 cm^{-1}, four A_g modes exist in polythiophene. In unsubstituted polythiophenes, these modes give rise to a pattern of three main Raman bands and three strong bands in the PIA spectrum [41] and in the doping-induced absorption spectrum [42]. Ehrenfreund and Vardeny [43] established a link between the doping-induced electronic state within the semiconducting π–π^* energy gap and the IRAV bands of doping-induced infrared spectrum based on a linear response theory by Girlando et al. [44]. Linear infrared absorption studies proved that there is no interaction between the conjugated-polymer backbone and the C_{60} molecule in the ground state, as already found by UV/vis absorption measurements. The infrared spectrum, which is dominated by the vibrational absorptions of the conjugated-polymer backbone, shows no change upon addition of 5% C_{60} in the dark. However, upon photoexcitation, the photoinduced electron transfer creates long-lived charges in the conjugated-polymer/C_{60} composites. The high concentration and
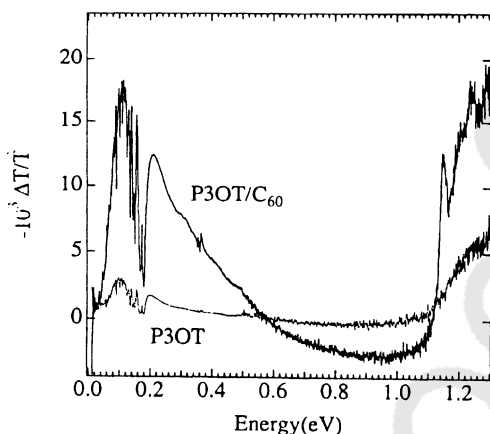
Fig. 11.10 Photoinduced infrared absorption spectra of poly(3-octylthio-
phene) (*P3OT*) and P3OT/C_{60} (5%) at 80 K obtained by pumping with an
argon ion laser at 2.41 eV. (Reproduced with permission from [45]).

the longer lifetime of the photoinjected charges on the polymer backbone
strongly enhance the IRAV modes. In Fig. 11.10, the PIA spectrum of a P3OT
composite with C_{60} is compared to a spectrum of a pristine P3OT film. Addi-
tion of few weight percents of C_{60} strongly enhances the intensity of the IRAV
bands and the lower polaron peak of the polymer [45]. Additionally, two elec-
tronic absorption bands, located at 1.15 and 1.25 eV, are detected. These bands
are associated with the formation of the C_{60}^- anion. The quenching of the triplet
peak around 1.35 eV cannot be seen in this figure.

11.2.2
Sensitivation of Conductivity

Figure 11.11 shows on a semilog plot the spectral response of the steady-state
photoconductivity (PC) of pristine MEH-PPV and MEH-PPV:C_{60} blends for dif-
ferent concentrations of C_{60} [28]. These room temperature data are normalized
to the constant incident photon flux of about 7.5×10^{14} photons cm^{-2} s^{-1}. The
admixture of 1% of C_{60} results in an increase of initial photocurrent by one or-
der of magnitude. This observation is in full agreement with the photoinduced
electron-transfer phenomenon which leaves metastable positive polarons on the
polymer backbone after the electron transfer, i.e., "*photodoping*". Moreover, tran-
sient PC studies revealed that beyond an increase of the number of charge car-
riers, the addition of C_{60} in MEH-PPV does increase the lifetime of the charge
carriers detected by this method up to several nanoseconds [28].

<QA>19. 11.2.3
Title / Is "sensiti-
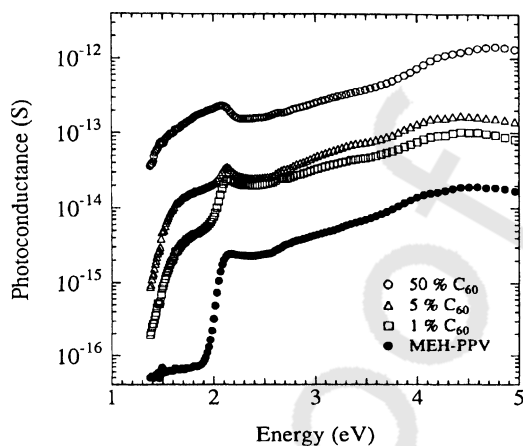vation" the correct
word here? Please
check.

Fig. 11.11 Spectral response of the steady-state photoconductivity of pristine MEH-PPV and MEH-PPV:C_{60} blends for several C_{60} concentrations at 300 K and a biasing field of 10^4 V cm^{-1}. (Reproduced with permission from [28]).

11.2.3
Magnetic Properties

Light-induced electron spin resonance (LESR) is a very powerful method for investigating photoinduced charge-transfer systems. Definitive evidence of charge separation has been obtained from such experiments. Figure 11.12 shows the ESR signal upon illuminating a MDMO-PPV:PCBM blend with light of $hv = E_{\pi-\pi*}$ where $E_{\pi-\pi*}$ is the energy gap of the conjugated polymer (donor) [46]. Two photoinduced ESR signals can be resolved: One at $g = 2.0026$ and the other
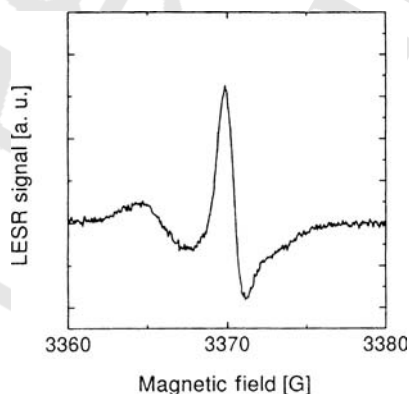

Fig. 11.12 Light-induced electron spin resonance (*LESR*) spectra of a MDMO-PPV:PCBM blend upon illumination with a 2.41 eV argon ion laser. (Reproduced with permission from [46]).

at $g = 1.9997$. The higher g-value line is assigned to the conjugated-polymercation (polaron) and the lower g-value line to C_{60}^{-} anion. The assignment of the lower g-value line to C_{60}^{-} is unambiguous, for this atypically low g value is characteristic for fullerene anions [47]; the higher g value is typical of conjugated polymers. At 200 K, the LESR signals have nearly vanished, demonstrating the reversibility of the photoinduced generation of radicals. Subsequent LESR measurement cycles of heating to 290 K, cooling down to 100 K, illumination with light, switching light off and heating up again yield identical results. More information on the relaxation behavior of the two photoinduced radicals is gained from the integrated LESR signal: It shows two peaks with comparable areas, indicating that both radicals have equal amounts of spin [46].

11.3
Bulk-Heterojunction Solar Cells

11.3.1
Basics of Organic Solar Cells

Conjugated-polymer thin films sandwiched between two metal electrodes are usually described using a metal–insulator–metal picture (MIM) [48]. As illustrated in Fig. 11.13 a, the vacuum levels (E_{vac}) of the stacked materials will align themselves (Schottky-Mott model). This argument is currently under strong debate within the scientific community [49], since it has been reported that interface dipoles [50] can appear between metal and organic semiconductor [51] inducing E_{vac} discontinuity, strong local field and Fermi-level alignment. Nevertheless, since the MIM picture provides a first approximation allowing one to draw a simple scheme of the energetic levels within the device, we shall use this model to describe in a simple manner the working principle of organic solar cells. Moreover, for simplicity, we consider in the following paragraph that the photoactive layer is made of one single material, possessing one HOMO and one LUMO.

Figure 11.13 a represents the energetic diagram of an organic solar cell in open-circuit (OC) condition. The E_{vac} of the different materials are aligned as explained above and no electrical field is present within the device. Figure 11.13 b shows the short-circuit (SC) condition: The Fermi levels of the two electrodes align themselves and a built-in field is induced in the bulk of the organic layer due to the asymmetry of the work function of the electrodes: a constant slope appears for the HOMO, the LUMO, and the E_{vac} levels of the organic layer. When the device is polarized in the forward direction (high-work-function electrode (HWFE) connected to positive and low-work-function electrode (LWFE) connected to negative) as in Fig. 11.13 c, electrons can be injected from the LWFE to the LUMO of the organic layer, and holes from the HWFE to the HOMO or the organic layer. The effective field in the device will ensure the drift of electrons from LWFE to HWFE and holes from HWFE to LWFE. Actually, the efficiency of the charge in-
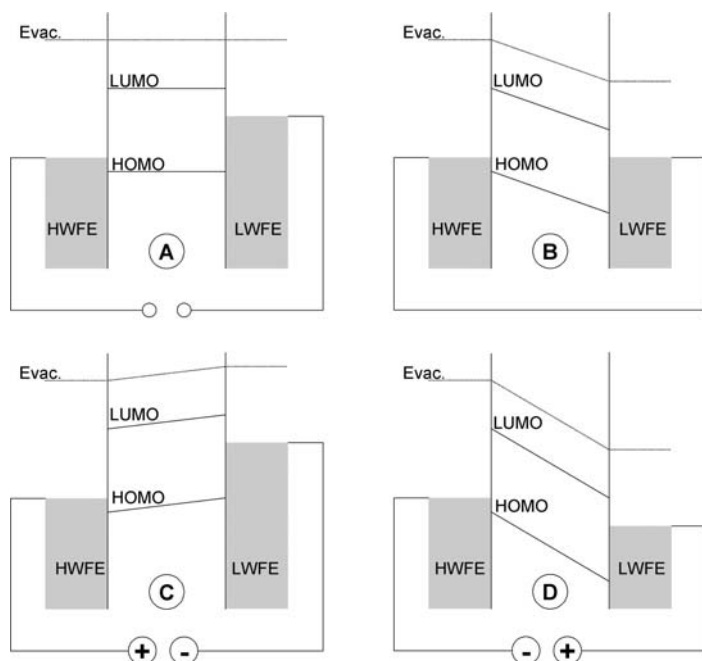
Fig. 11.13 Operating modes of a simple diode made out of a single active material sandwiched between high-work-function (*HWFE*) and low-work-function (*LWFE*) electrodes. (a) Open circuit condition. (b) Short circuit condition. (c) Forward bias. (d) Reverse bias. *HOMO* Highest occupied molecular orbital, *LUMO* lowest unoccupied molecular orbital.

jection is driven by the energetic mismatch (ϕ_b) between the Fermi levels of the electrodes and the level of the band in which the charge are to be injected. If a contact is ohmic ($\phi_b = 0$ [52]), the injection is mostly space-charge-limited (SCL) [53]: the electrode supplies more charge carriers per unit time than the organic semiconductor can transport because of too-low mobility, hence space charges appear in the vicinity of the electrode. On the other hand, if ϕ_b is important, the injection is limited by thermally assisted hopping from the Fermi level of the electrode into localized states of the semiconductor [54, 55]. These states are usually described as belonging to a Gaussian density-of-states (DOS) broadened by energetic disorder [56]. Finally, when the device is polarized in the reverse direction (HWFE connected to negative and LWFE connected to positive) (Fig. 11.13 d), charge injection is hindered by the field that reigns in the device.

Solar cells are operated between OC and SC conditions (fourth quadrant in the current–voltage characteristics), as shown in Fig. 11.14. It should be mentioned that in this particular region, the driving force of charge collection in organic solar cell still remains under discussion, as will be shown in Section 11.4.5 However, the general principle can be generally assigned to the gradient in electrochemical potential present within the device [3, 5, 57].

<QA>30. 11.3.1 It should be mentioned that / Please check this change. Because there were originally two sections 4.3, section numbers have been altered.
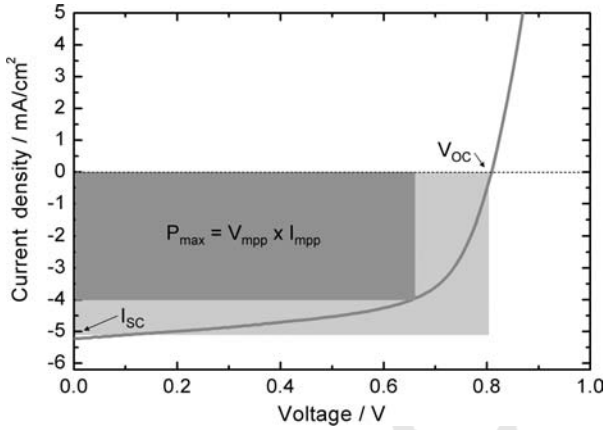
Fig. 11.14 Third and fourth quadrant of a typical *I–V* curve observed for a glass/ indium-tin-oxide (ITO)/poly(3,4-ethylene-dioxythiophene) (PEDOT) : poly(styrene sulfonate) (PSS) (90 nm)/MDMO-PPV : PCBM (1 : 4150 nm)/Al(100 nm) solar cell. Shown are the SC current (I_{SC}), the OC voltage (V_{OC}), and the voltage (V_{mpp}) and current (I_{mpp}) at maximum power point (P_{max}).

The overall efficiency of a solar cell can be expressed as follows:

$$\eta = \frac{V_{OC} \cdot I_{SC} \cdot FF}{P_{in}} \tag{1}$$

where V_{OC} is the OC voltage (voltage for $I=0$), I_{SC} is the SC current (current for $V=0$), and P_{in} the incident light power. In order to allow objective comparison, device characterization has to be performed in the same conditions [58]. The accepted standard for solar-cell testing is the so-called AM 1.5 [59], which is a 100 mW cm^{-2} white light with a spectral intensity distribution matching that of the sun on earth's surface at a tilted angle of 37°.

The *Fill Factor* (*FF*) of a device is given by:

$$FF = \frac{I_{mpp} \cdot V_{mpp}}{V_{OC} \cdot I_{SC}} \tag{2}$$

where I_{mpp} and V_{mpp} represent the current and voltage at the maximum power point (P_{max}) in the fourth quadrant, respectively (Fig. 11.14).

Finally, a last important parameter experimentally accessible is the variation of I_{SC} with the wavelength λ of incident light. This value, called the external quantum efficient (EQE) or incident photon to collected electron (IPCE) gives the ratio of collected charge carriers per incident photons:

$$EQE = \frac{1240 \cdot I_{SC}}{\lambda \cdot P_{in}} \tag{3}$$

where λ is expressed in nanometers, I_{SC} in amperes per meter squared, and P_{in} in watts per meter squared. This value can be further corrected by different losses like reflection from the glass surface and absorption by different nonphotoactive layers involved in the device (substrate, electrode, etc.) to illustrate the internal quantum efficiency (IQE).

11.3.2
Pure Conjugated-Polymer Photovoltaic Devices

As mentioned above, photogenerated excitons in a conjugated polymer have to be dissociated into free charge carriers to participate to the extracted current. In the case of pristine polymers, the only efficient way to ensure this dissociation is the action of an electric field. In the simple MIM picture [48], the number of charge carriers present in the device is small enough to ensure rigid, straight HOMO and LUMO bands. On the other hand, if the organic semiconductor is doped, band bending can appear, inducing Schottky contact at the metal–electrode interface. In any case, an electric field does appear in the device under the SC condition, if the work functions of the electrodes are asymmetric. In the former case, the electric field present in the device is constant throughout the entire thickness of the device. In the latter case, the field drops in the depletion zone (Fig. 11.15) but is larger over a smaller thickness. Since large electric fields are mandatory to dissociate excitons, Schottky devices are expected to enhance the charge generation in pristine-conjugated polymer.

The very first efforts to achieve PV devices using conjugated polymers were performed on polyacetylene [60] and some polythiophenes [61, 62]. However, from the conjugated polymers of the first generation, PPV appeared to be the
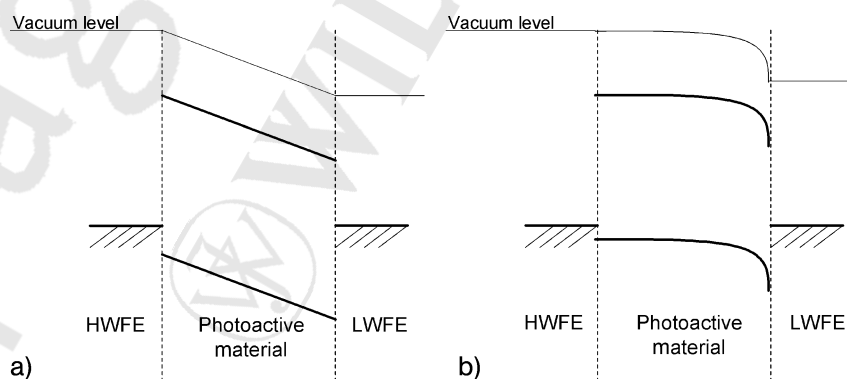

Fig. 11.15 Energetic diagram of (a) undoped and (b) *p*-doped organic semiconductor sandwiched between a HWFE and a LWFE, under SC condition. In (a), the electric field is homogeneous throughout the entire device thickness, while in (b) the field drops linearly in the depletion zone present in the polymer on the LWFE side.

most successful candidate for single layer polymer PV devices [63]. The radiative recombination channels of the injected electrons and holes within PPV and its derivatives which resulted in light-emitting diodes (LEDs) [64, 65] suggested this class of materials for PV devices. Interestingly it was found that the same devices exhibit excellent sensitivity as photodiodes under reverse bias, with quantum yields above 20% (electron/photon) at –10 V reverse bias [66]. This observation opened a route to elaborating monolithic device that can act as light emitter *and* detector. Moreover, devices based on derivatives of polythiophene exhibited an even better photoresponse (80% electron/photons at –15 V), competitive with UV-sensitized Si photodiodes [66–68], but in both cases, externally applied voltage was necessary to extract significant amount of charges.

For PV effect, it appeared that the intrinsic field induced by the asymmetry of the work function of the electrodes could not be large enough to generate significant power. Antoniadis et al. [69, 70] reported the observation of an IPCE maximum of 5% in indium-tin-oxide (ITO)/PPV/Al photodiodes and of a power conversion efficiency of approximately 0.1% under low light intensities of 1 mW cm^2. The typical film thickness of the devices was varied between 100 and 600 nm. The OC voltage as defined with respect to the ITO electrode was measured to be 1.2 V; this negative OC voltage was explained by the formation of a Schottky barrier at the Al/PPV interface.

The formation of a Schottky barrier at the Al/PPV interface was also observed by other groups. The PPV photodiodes prepared by Karg et al. appeared to be considerably more conducting [71]. The properties of the devices studied by this group could be modeled by considering a Schottky junction at the top electrode. The observation of a depletion layer at the Al interface and its dependence on the applied voltage allowed estimation of the intrinsic hole concentration as high as 10^{17} cm^{-3} [72]. Subsequently, Riess et al. [73] observed PV effect in PPV Schottky diodes with a power conversion efficiency between 0.1% to 1% for devices with a thickness varying from 100 to 500 nm at very low light intensities. The voltage at OC condition V_{OC} of these ITO/PPV/Al devices varied between 0.7 and 1.3 V. The low *FF* (0.22) indicated the formation of a back-diode interface between the PPV and one of the metal electrodes. Detailed information about the structure of the devices could be obtained by complex impedance measurements (Fig. 11.16). The observation of two semicircles in the impedance plane is proof of the existence of different RC circuits, representing the bulk and the junction. The high resistance of the junction dominates at low bias while with increasing forward bias the junction resistance decreases, whereas the bulk resistance is nearly unaffected.

<QA>21. 11.3.2 The observation of two semicircles in / Please define RC.

Though it appeared that the creation of a Schottky contact could enhance the generation of charge carriers, the depletion zone is usually too small to allow a large absorption of light in it. Thus, while allowing the realization of efficient photodetectors operated under externally applied voltage, simple layers of pristine-conjugated polymer were shown to be unable to produce significant PV effect.
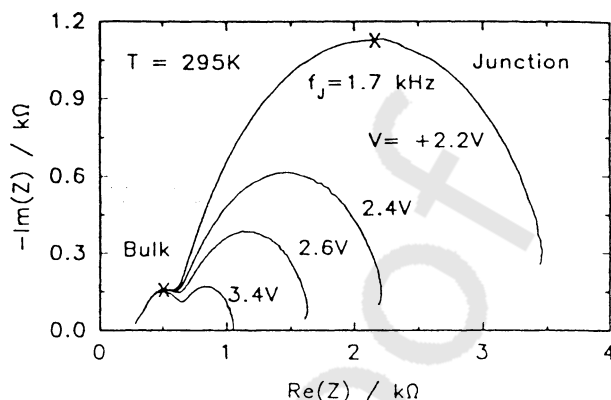
Fig. 11.16 Impedance plots of an ITO/PPV/Al diode under various forward biases. The thickness of the device is about 350 nm. (Reproduced with permission from [73]).

11.3.3
Conjugated Polymer-Based Bilayer Devices

<QA>22. 11.3.3 However, bearing in mind what / Please check the Section number inserted.

Analysis of pure conjugated polymer single-layer devices reveals that exciton dissociation by the simple action of the built-in film is not efficient enough to generate appreciable PV effect. However, bearing in mind what has been presented in the Section 11.3.2, it appears obvious that PV devices might be achievable by the simple superposition of a donor and an acceptor material. Indeed, the photogenerated excitons can diffuse and reach the interface between the two materials and then dissociate into charge carriers via charge transfer.

The use of organic bilayers with photoinduced electron transfer at the interface has been much investigated over the last decades (for a summary of the early reports see, for example, [74–76]). In 1979, Tang et al. demonstrated PV activity in small molecular bilayers which were vacuum-evaporated [77]. In this pioneering work, the authors used a vacuum-evaporated copper–phthalocyanine (250 Å) and a perylene-derivative (450 Å) system sandwiched between In_2O_3 and silver electrodes [78]. This bilayer device showed a current–voltage characteristic with a high rectification, high *FF* and a PV power conversion efficiency of around 1%. Until recently the Tang cell was the most efficient organic solid-state PV cell. In the following we will discuss the realization of a Tang-cell-like structure based on conjugated polymer- and fullerene-based materials.

The first realization of a conjugated polymer/fullerene diode was achieved shortly after the detection of the ultrafast photoinduced electron transfer between MEH-PPV and C_{60} [79]. Figure 11.17 gives a schematic description of the device used at that time, which comprised a 100-nm MEH-PPV layer, and a 100-nm C_{60} layer, sandwiched between ITO and Au. The current–voltage characteristics of such a bilayer in the dark at room temperature can be observed in Fig. 11.18. A rectification ratio of approximately 10^4 at ± 2 V was found. Illumination by visi-
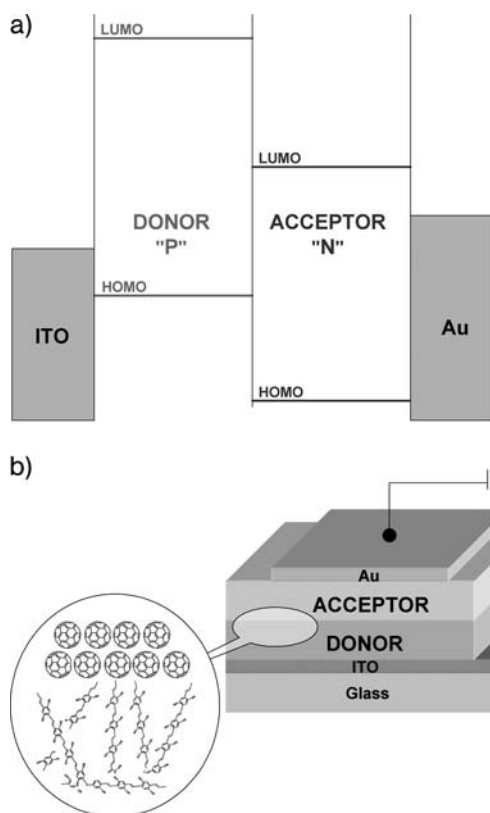
Fig. 11.17 Band diagram (a) and schematic cross section (b) of the ITO/MEH-PPV/C$_{60}$/Au bilayer donor–acceptor, as studied in [79].

ble light drastically modified the current–voltage behavior (Fig. 11.19): an OC voltage (V_{OC}) of 0.44 V and a SC current density (J_{SC}) of 2.08×10^{-6} A cm^{-2} were measured. Assuming a *FF* of 0.48 a power conversion efficiency of 0.04% was calculated. In the meantime, Morita and coworkers reported the optical response of a heterojunction device comprising a P3OT and C$_{60}$ bilayer [22]. The photoresponse of these devices showed an enlarged excitation profile than in the case of devices based on PPV derivatives, as will be detailed later.

An important limitation for bilayer devices arises from the fact that the effective zone of the photoactive layer is comprised within the exciton diffusion range from the interface between the donor and the acceptor material. Therefore, the electromagnetic field that has to be absorbed should be optimized in this area. The weak absorbing properties of C$_{60}$ in the visible part of the spectrum allows its usage as a spacer layer between the absorbing conjugated polymer layer and the back reflecting metallic electrode [80, 81]. The thickness of the layer can be chosen to give constructive interference from the back-reflected beam with the incident beam. Halls et al. prepared heterojunction cells by spin
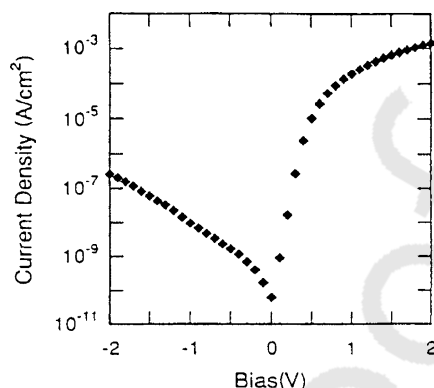
Fig. 11.18 Dark current versus voltage characteristics of an ITO/MEH-PPV/
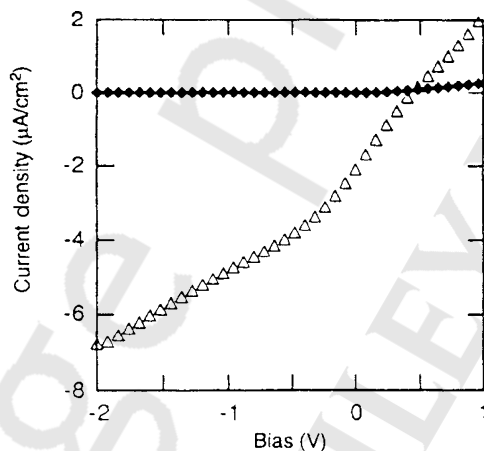C_{60}/Au device at room temperature. As studied in [79]. (Reproduced with
permission).

Fig. 11.19 Current versus voltage characteristics of an ITO/MEH-PPV/C_{60}/
Au device in dark (diamonds) and upon illumination with a 514.5 nm line
of an argon-ion laser of 1 mW cm^2 (triangles), as studied in [79].
(Reproduced with permission from [79]).

casting PPV precursor onto ITO glass. After the heat conversion, C_{60} was evapo-
rated on top of the PPV and finally Al contacts were evaporated. ITO/PPV/C_{60}/
Al devices were studied with various thicknesses of the single organic layers.
The highest IPCE efficiency of 9% was reported for a device with 65 nm PPV
and 40 nm C_{60}. The V_{OC} approached 0.8 V under full illumination. Similar high
IPCE efficiencies of 6% were reached when C_{60} was replaced by bis(phenethyli-
mido)perylene [82].

In order to maximize the energy of the exciting optical electric field at the
polymer/C_{60} interface, Roman et al. performed some optical modeling and cal-
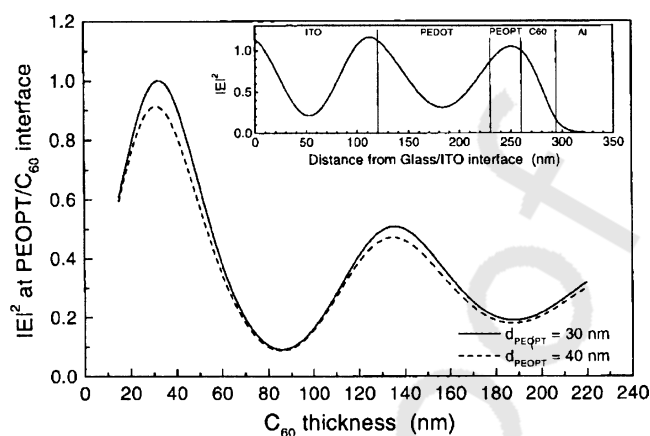
Fig. 11.20 Calculated values of the square of the normalized electrical field $|E|^2$ at the C_{60}/ poly{3-[4′-(1′,4′)-7′-trioxaoctyl]phenyl-thiophene} interface for PEOPT thicknesses d_{PEOPT} of 30 nm (solid line) and 40 nm (dashed line) versus thickness of the C_{60} layer at a wavelength of 460 nm. The inset shows the calculated distribution of the square of the normalized optical field $|E|^2$ inside an ITO (120 nm)/PEDOT-PSS (110 nm)/PEOPT(30 nm)/C_{60} (32 nm)/Al device at the same wavelength. (Reproduced with permission from [81]).
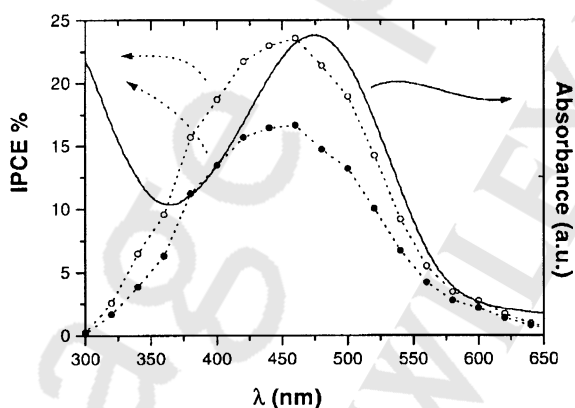
Fig. 11.21 Spectral response of devices made with different PEOPT polymer thicknesses: Al/C_{60} (35 nm)/PEOPT (30 nm)/PEDOT-PSS (110 nm)/ITO (120 nm)/glass (solid circles) and: Al/C_{60} (35 nm)/PEOPT (40 nm)/PEDOT-PSS (110 nm)/ ITO (120 nm)/glass (open circles). The absorption spectrum of the PEOPT polymer is plotted for comparison (solid line).*IPCE* Incident photon to collected electron. (Reproduced with permission from [81]).

culated the electric field (square) distribution inside the device [81]. Figure 11.20 shows the evolution of $|E|^2$ at the very interface between donor and acceptor versus the thickness of the fullerene layer for two different thicknesses of the conjugated polymer poly{3-[4′-(1′,4′),7′-trioxaoctyl]phenylthiophene} (PEOPT) layer.

It can be seen that $|E|^2$ shows a periodic variation with the thickness of the C_{60} layer, having a global maximum at about 32 nm of C_{60}. This maximum was found to be independent of the thickness of the conjugated polymer layer, yet the amplitude of $|E|^2$ is larger for the thinner PEOPT case. The realization of the devices confirmed the theoretical calculations. The spectral response of two devices with different thin PEOPT layers is shown in Fig. 11.21. The IPCE for the 30 nm PEOPT device shows a maximum of 23%, while the 40 nm PEOPT device reaches only 17%.

Thus, the results mentioned above suggest that the bilayer concept is drastically limited by the short diffusion range of the excitons [8, 11, 12]: Only the ones created close enough to the donor–acceptor interface (5–15 nm) are able to dissociate and release some charge carriers. Although the overall performances of such devices can be enhanced by optimizing the electromagnetic field distribution [81, 82] or by stacking several cells by series connection [83, 84], the bilayer concept appears not to exploit entirely the opportunities offered by the donor–acceptor approach.

11.3.4
Conjugated Polymer-Based Bulk-Heterojunction Devices

To overcome the limitations of the bilayer concept, the surface area of the donor–acceptor interface needs to be increased. This can be achieved by creating a mixture of donor and acceptor materials with a nanoscale phase separation resulting in a three-dimensional interpenetrating network: the so-called *bulk heterojunction* (Fig. 11.22). The rather poor solubility of pure C_{60} in organic solvent and its tendency to crystallize during film formation [85] limits high concentration loading. The synthesis of 1-(3-methoxycarbonyl)propyl-1-phenyl[6,6]C_{61} (PCBM) [86], a soluble and processable derivative of fullerene C_{60}, allowed the realization of the first bulk-heterojunction solar cell by blending it with MEH-PPV [87]: With this soluble derivative, it is possible to prepare more than 80 wt% fullerene-loaded PPV films. Figure 11.22a illustrates the energetic diagram under the OC condition for the MEH-PPV:PCBM bulk heterojunction studied by Yu et al. [87]. Contrary to the situation in Fig. 11.17a, excitons ideally experience dissociation wherever they are created within the bulk, since the next interface between donor and acceptor phases is potentially present within the exciton diffusion length everywhere in the device. After having been created throughout the bulk, the free carriers have to diffuse and/or be driven to their respective electrode. Despite the fact that the PL of the MDMO-PPV:PCBM blend is already quenched for a PCBM concentration as low as 1% (Fig. 11.6), the onset of the photocurrent was shown to appear for an acceptor amount about 17% weight (assuming similar densities, this corresponds to percentage volume). Interestingly this number corresponds to the calculated percolation ratio of spherical metallic particles embedded in a continuous matrix [88, 89]. In other words, to be efficient, the bulk heterojunction has to ensure a bicontinu-
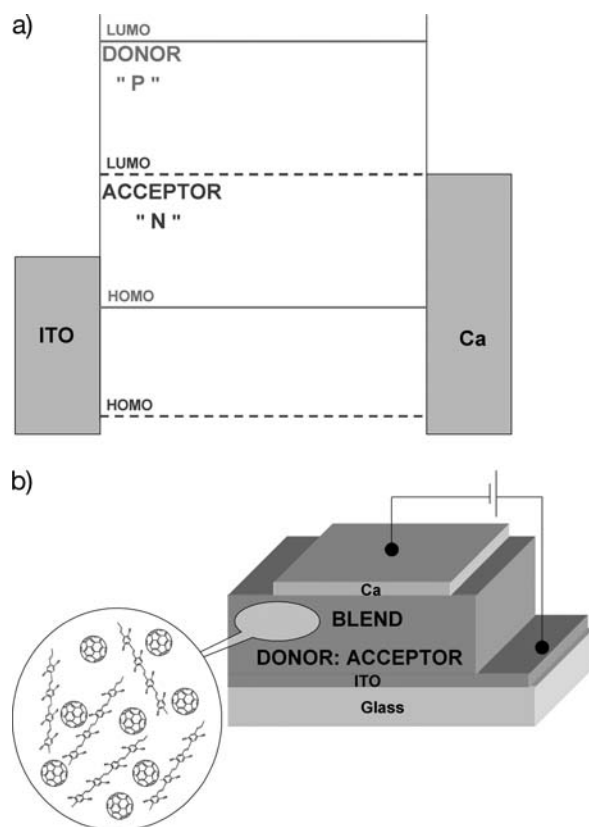
Fig. 11.22 Band diagram (a) and schematic cross section (b) of the ITO/
MEH-PPV/C$_{60}$/Au bilayer donor–acceptor studied in [87].

ous path for electrons and holes to their respective electrode. In the case of this
very first ITO/MEH-PPV:PCBM/Ca bulk-heterojunction device, Yu et al. re-
ported a maximum IPCE efficiency of about 29%. Further optimization of the
device using the very same active materials has been achieved. For example, the
introduction of a thin ($\sim$ 90 nm) layer of poly(3,4-ethylenedioxythiophene)
doped with poly(styrene sulfonate) (PEDOT:PSS) between ITO and the active
material was found to improve drastically the diode quality. Being a highly hole-
conducting metal-like polymer, this material eases the injection of holes by low-
ering the intrinsic energetic barrier between the ITO work function and the
HOMO of the active material [90]. Moreover, this layer acts as a potentially
semipermeable membrane for holes, blocking the extraction of electrons on the
ITO side. But PEDOT:PSS also allows smoothing of the ITO surface, usually
quite rough, and hence reduces the risks of shortcuts within the device [91].
The addition of a very thin layer of LiF (0.6 nm) between the active organic
layer and the metallic electrode is also known to drastically improve the devices

[92]. Initially employed in organic light-emitting diode (OLED) technology [93], this intermediate ionic salt layer not only increases the *FF* but also the V_{OC} of the device [92], though the reasons for its effectiveness are not yet fully understood [94]. Finally, enhancement of the transport properties of the PPV derivative by chemical synthesis [95, 96] and optimization of the solvent used to prepare the PPV-derivative-PCBM blends led to MDMO-PPV:PCBM bulk-heterojunctions solar cells with efficiency up to 2.5% under AM1.5 [95, 97].

Before separately addressing the different parameters that influence the efficiency of conjugated polymer:fullerene solar cells, we should mention another approach that has been proposed to realize conjugated-polymer-based devices. This one, based on the use of polymers as both donor and acceptor components, offers several advantages. Firstly, since entropy of mixing for macromolecules is extremely small, phase separation is expected in polymer blends, leading to microstructured donor–acceptor junctions and potential continuous paths for charge carriers. Moreover, by using donor and acceptor polymers with different band gaps, one can design the photosensitivity of the cell over the whole visible range and, thus, overcome the drawback of C_{60}-based materials that are almost nonabsorbing in the visible.

Two different groups reported simultaneously the construction of a PV bulk heterojunction formed between two different conjugated polymers [98, 99]. Both approaches used MEH-PPV as donor blended with a cyanosubstituted MEH-PPV used as an acceptor. Yu et al. reported monochromatic power conversion efficiencies around 1% and IPCE around 6% at low light intensities [98]. The best results for PV devices were obtained with approximately 5 wt% CN-PPV in the composite. On the other hand, Granström et al. announced 4.8% monochromatic power conversion efficiencies and an IPCE of 29% observed in a polymer–polymer device fabricated via lamination [100]. This well-known technique from polymer processing does facilitate the melt-blending of two different polymer layers under applied pressure. The necessary requirement of melt-processable materials was met by using a poly(3-phenyloctylthiophene) as donor polymer and a cyanosubstituted MEH-PPV as acceptor moiety. Two glass substrates were coated with low- and high-work-function metals as well as with acceptor-rich (19:1) and donor-rich (1:19) polymer composite layers. This different stoichiometry for the two layers induces a gradient for hole-conducting and electron-conducting components in the bulk heterojunction. The two glass slides were then pressed while heated and the two polymer films were blended by lamination. This method clearly demonstrated the large potential of polymer technology utilized in PV devices using conjugated polymers.

11.4
Determining Parameters of Bulk-Heterojunction Solar Cells

11.4.1
Voltage at Open Circuit

Being a major parameter of any solar cells, the OC voltage (V_{OC}) has been the object of numerous studies. It is commonly accepted that the appearance of the V_{OC} is induced by the splitting of the electron and hole quasi-Fermi level [3, 101]. Therefore, it is directly correlated to the built-in potential V_{bi} of a given device [102]. According to the MIM picture [48], the V_{bi} should be given by the difference of the work functions of the metal electrodes (ϕ_{ME}). In the case of semi-transparent insulators (or totally depleted semiconductors), an elegant way of studying the V_{bi} is offered by electroabsorption (EA) spectroscopy. EA is based on the distortion of the electron cloud of molecules and the altering of the dielectric function of the material by an applied electric field. Since semiconducting polymers are based on π-conjugated centrosymmetric systems, the induced changes scale with the square of the applied electric field (dc Kerr effect) [103] and are proportional to the imaginary part of the third-order nonlinear susceptibility [Im$\chi^{(3)}$]. Considering a sinusoidally modulated applied voltage of frequency ω, the following proportionality is found for the normalized change in transmission of the first harmonic EA response [104]:

$$\frac{|\Delta T|}{T}(hv) \propto (V_{DC} - V_{bi}) \cdot V_{AC} \cdot \sin(\omega t) \tag{4}$$

To determine V_{bi}, the ac amplitude (V_{ac}) and the probe light wavelength are kept constant, while the dc offset (V_{dc}) is changed in steps. A $\Delta T/T$ equal to zero indicates that the internal electric field is cancelled by the externally applied field. Brown et al. used EA to investigate the impact of intermediate layer like PEDOT PSS, LiF and CsF on the built-in field of single-conjugated layer devices. They observed that the highly doped PEDOT tends to increase the built-in field of the devices because of its lower lying Fermi level compared to ITO [105]. Moreover, they reported that the use of an ionic salt like LiF does significantly reduce the barrier injection at the cathode, increasing the built-in field as well (Fig. 11.23) [106, 107].

In the case of single polymer-layer PV devices, the influence of the work function of the electrodes has been investigated, for example, by Marks et al. [63]. For ITO/PPV/Mg devices, the fully saturated OC voltage was 1.2 V and 1.7 V in the case of an ITO/PPV/Ca device. These V_{OC} values are almost equal to the difference in the work function of Mg and Ca with respect to ITO. This observation tends to confirm the applicability of the MIM picture in the case of pristine, undoped polymers [108]. It has been reported that in the case of bilayer device, the V_{OC} also scales with the difference of the electrode work function. However, an additional light-intensity-dependent contribution has been identi-
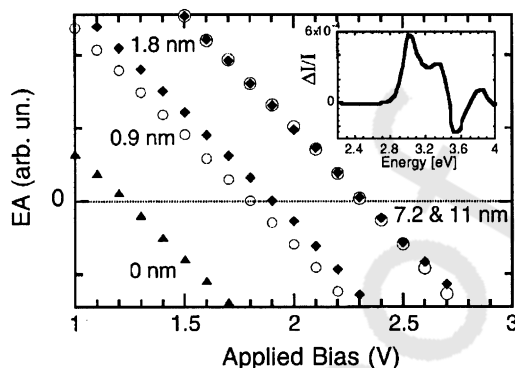
Fig. 11.23 Electroabsorption response at $hv=2.95$ eV and $V_{ac}=0.1$ V versus dc bias applied on an ITO/PEDOT:PSS/polyarylene/LiF/Al with different LiF thicknesses. The built-in potential corresponds to the bias at which the EA response intersects with the zero axis. The spectral dependence of the signal is shown in the inset. (Reproduced with permission from [106]).

fied. This additional contribution is attributed to photoinduced generation of charge carriers at the very interface between the donor and the acceptor, whereby an accumulation of charge carriers results in a dipole across the interface. This dipole gives rise to a diffusion current that must be counterbalanced by a drift current under OC conditions [109].

On this basis, a typical MDMO-PPV:PCBM bulk-heterojunction sandwiched between ITO ($\phi_{ITO} \approx 4.7$–4.9 eV) and aluminum ($\phi_{Al} \approx 4.3$) is expected to show a maximum V_{OC} of about 0.4–0.6 V. In reality, V_{OC} reaches values up to 0.8 V in this case (Fig. 11.14). Actually, the maximum value of V_{OC} appears to be limited by the energy difference between the HOMO of the donor and the LUMO of the acceptor. Indeed, they represent respectively the lowest and highest values that the quasi-Fermi levels of holes and electrons can potentially reach, knowing that the splitting of these levels accounts for the V_{OC}. It has been observed that in the case of Al top electrodes the V_{OC} of MDMO-PPV:fullerene cells varies almost linearly with the acceptor's first reduction potential (LUMO level) (Fig. 11.24) [110]. Along the same lines, combining different PPV derivatives with always the same acceptor (PCBM in this case) was shown to induce a V_{OC} that follows linearly the evolution of the HOMO of the donor [111]. The same exercise was performed with several polythiophenes of different oxidation potentials mixed with PCBM, confirming the linear influence of the HOMO of the donor on the V_{OC} (Fig. 11.25) [112].

On the bottom electrode side, it has been observed that the work function of polyethylene dioxythiophene-polystyrene sulfonate (PEDOT:PSS) has an impact on V_{OC} with a proportionality factor of 0.8 [113]. The realization of an "inverted" solar cell by choosing a dedoped PEDOT having a work function smaller than the LUMO of the PCBM confirmed the validity of the MIM picture in this case.
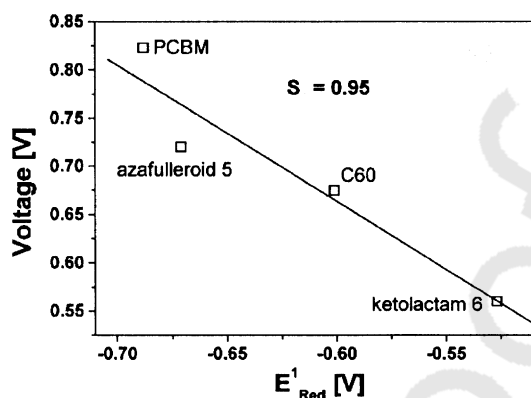
Fig. 11.24 V_{OC} versus acceptor strength. The slope (S) of the linear fit to the data is 0.95. (Reproduced with permission from [110]).
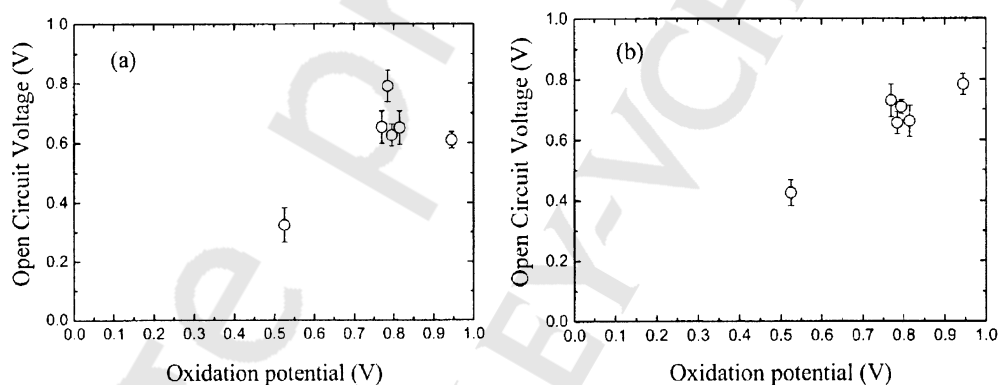

Fig. 11.25 V_{OC} versus oxidation potential of the polythiophenes used in polythiophene:PCBM BHJs with (a) Al, and (b) LiF/Al cathode. The open circles represent the mean value of all the measurements. (Reproduced with permission from [112]).

Although the observations reported above are commonly accepted, the influence of the top electrode is still under debate. Brabec et al. reported that the work function of the top electrode influences V_{OC} only very slightly (Fig. 11.26) [114]. This effect was attributed to a pinning [115] of the metal work function towards the LUMO of the fullerene, due to numerous surface states in the latter [116]. The potential effect of surface dipoles [51] was ruled out in this case [49]. On the other hand, Mihailetchi et al. concluded that the MIM picture is respected for metals forming nonohmic contacts with the photoactive material [117]. In the case of ohmic contact, charge-carrier transfer from the metal to the semiconductor would explain a loss in the V_{OC} and a deviation from the MIM theory. Nevertheless, both approaches agree on the pinning effect induced by a

<QA>16. 11.4.1 / 11.4.3.2 / On the other hand .../ According to the ... / I have changed this name to agree with the reference list; please check.
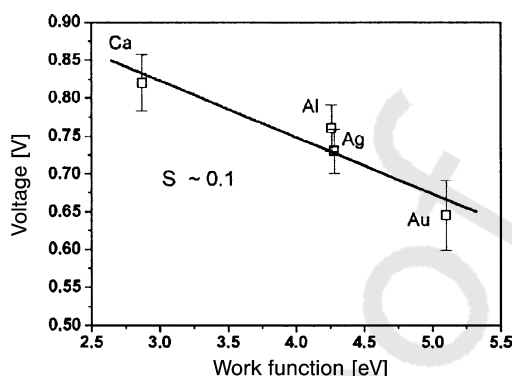
Fig. 11.26 V_{OC} versus top electrode work function. The slope of the linear fit to the data is 0.1. (Reproduced with permission from [110]).

small amount of LiF [93] used as an intermediate layer between the active material and the top electrode, which results in a considerable increase of the V_{OC} [92]. It should be added here that Mihailetchi et al. observed that the photocurrent calculated from the measured dark and light *I–V* curves, when plotted against the effective applied voltage ($V_{OC}-V_{applied}$), does not depend on the metal used for the top contact. This tends to show that the effective voltage present within the device is the very parameter controlling the photocurrent generation (Fig. 11.27) [118].

<QA>5. Figure legend Fig. 11.27 / Please define J_{ph}.

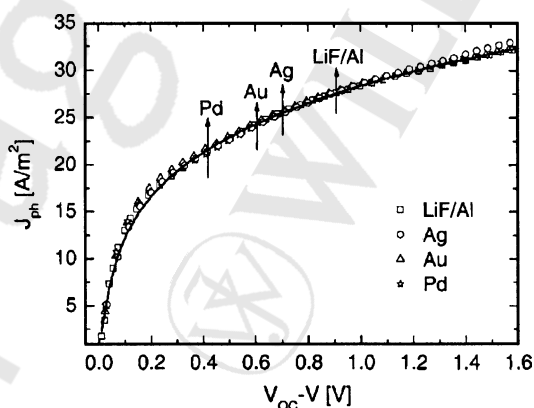**Fig. 11.27** Photocurrent versus effective applied voltage ($V_{OC}-V$) of poly[2-methoxy-5-(3′,7′-dimethyloctyloxy)-1,4-phenylene vinylene] (MDMO-PPV) : PCBM devices with four different top electrodes at 295 K. The solid line represents some numerical calculations, and the arrows indicate the SC current densities and corresponding V_{OC} of these devices. (Reproduced with permission from [118]).

Finally, it is important to notice that the V_{OC} has been shown to be affected by the ratio donor:acceptor [119], and by the morphology of the photoactive blend [108], induced for example during a heat treatment [120].

As mentioned above, the V_{OC} originates in the splitting of the respective quasi-Fermi level of electrons and holes. Therefore, one can expect light intensity and temperature dependences. V_{OC} is known to increase with increasing light intensity, usually following a logarithmic evolution until it reaches saturation: This saturation is dictated by the band gap of the photoactive material. Moreover, the V_{OC} was reported to decrease linearly with increasing temperature, with a slope nkT/q, n having been reported being between 2 and 1 [121, 122].

11.4.2
Light Harvesting

Despite the rather large optical gap of MDMO-PPV (2.2 eV), efficiencies up to 2.5% under AM 1.5 were reported for MDMO-PPV:PCBM blends [97]. However, these cells just harvest the photons that have wavelengths below 550 nm, that is, a very small part of the solar spectrum (Fig. 11.28). One obvious route to increase the solar-cell efficiency is to chemically engineer the band gap [123] of the macromolecules. For example, polythiophene derivatives [124, 125] like poly(3-hexylthiophene) (P3HT) were found to give solar cells with higher efficiency. Indeed, having an optical gap of 2 eV, this material allows EQE onset at about 650 nm, which is 100 nm above that of MDMO-PPV (Fig. 11.29). Thus,
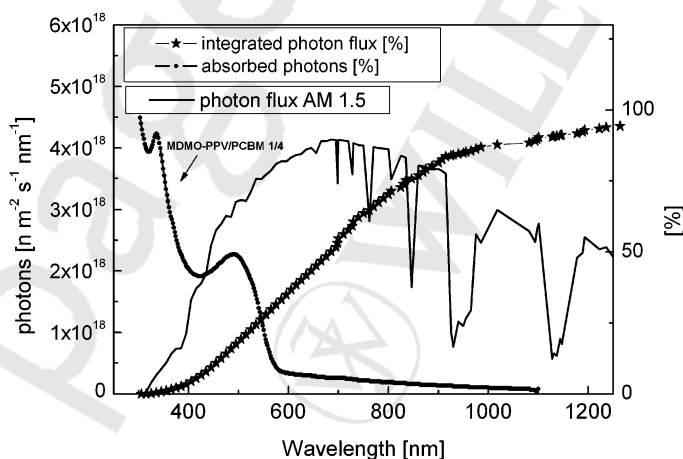

Fig. 11.28 AM 1.5 spectrum (see Section 11.30.1 for explanation) in comparison with the absorption profile of a MDMO-PPV:PCBM (1:4) film. The dots show the total photon flux, i.e., the percentage of photons available for materials with a certain optical band gap. (Reproduced with permission from [129]).
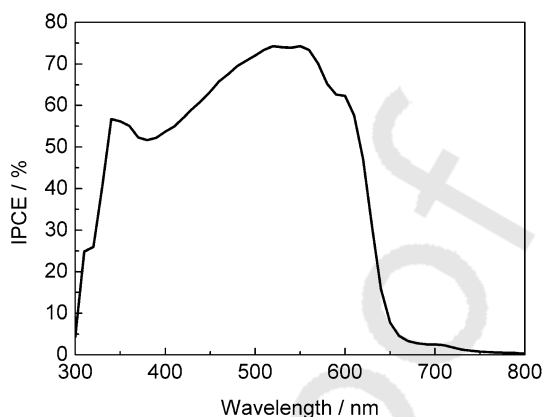
Fig. 11.29 IPCE of an ITO/PEDOT:PSS/poly(3-hexylthiophene) (P3HT):PCBM/Al device showing maximum up to 75%.

devices based on P3HT:PCBM were found to achieve EQE with a 76% maximum at 550 nm [126] (suggesting internal quantum efficiency close to unity at this wavelength), I_{SC} about 10 mA cm^{-2} [127] and an overall efficiency about 4% under AM 1.5 [126–128].

Currently, intense effort is being invested by synthetic chemists to create new materials that do absorb light in the red and infrared regions, i.e., "low-band-gap" materials [129]. Actually, yet more intermolecular interactions can further influence the band gap in the solid state: the intrinsic band gap of conjugated polymers is generally ascribed to four contributions related to the polymer backbone (Fig. 11.30) [129, 130]:

- the bond-length alternation E_1 which is directly related to the Peierls gap;
- the aromaticity (RE) of the structure, which competes with the delocalization by inducing a confinement of the π-electron;
- the conjugation length (E_{rot}), which decreases the gap when getting larger;

<QA>6. Figure legend Fig. 11.30 / Please define E_{SUB}, E_{ROT} and E_R.

Fig. 11.30 Influences of the chemical structure and conformation on the band gap of the conjugated polymer, here for example poly(paraphenylene). (Reproduced with permission from [129]).

- the substituent effect (E_{sub}), which can modify the energetic position of the HOMO and the LUMO levels.

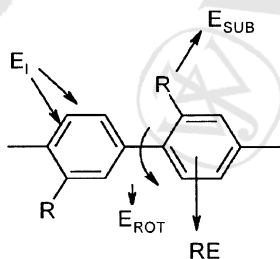Several interesting works have reported the extension of the IPCE of bulk-heterojunction solar cells toward the red. Among numerous polythiophene derivatives [131, 132], poly-3-{4-[2-(2-methoxy-ethoxy)ethoxy]phenyl}thiophene (PEOPT) was the object of intensive investigation. This material, reported to present a noncrystalline phase and an optical band gap of 2.1 eV in the solid state, was shown to be convertible into an ordered phase by heat treatment, accompanied by a decrease of the optical band gap down to 1.7 eV [133, 134]. The same heat-induced conversion phenomenon could be observed in PEOPT blended in PCBM. Unfortunately, the heat-induced conversion has been reported to decrease the overall film quality, and only poor PV performances could be achieved with this new material [134]. Another interesting attempt was performed with a electron-donor polymer consisting of alternating electron-rich *N*-dodecyl-2, 5-bis(2'-thienyl)pyrrole (TPT) and electron-deficient 2,1,3-benzothiadiazole (B) units, named PTPTB [135]. The material has been reported to show a band gap of 1.7 eV. When blended with PCBM, IPCE onsets at about 750 nm were observed, with overall efficiency close to 1% [129]. Finally, we would like to mention the work performed by Zhang et al. [136], and Wang et al. [137, 138] who have been able to extend IPCE spectra of bulk-heterojunction solar cells up to 850 and 1000 nm respectively, using copolymer of fluorene and donor–acceptor–donor moieties. In the latter case, IPCEs of 28% at 400 nm, 8.8% at 850 nm and 7% at 900 nm have been reported, as shown in Fig. 11.31.

On the acceptor side, several attempts have been carried out to increase the performance obtained with PCBM [139]. The most successful was a direct appli-
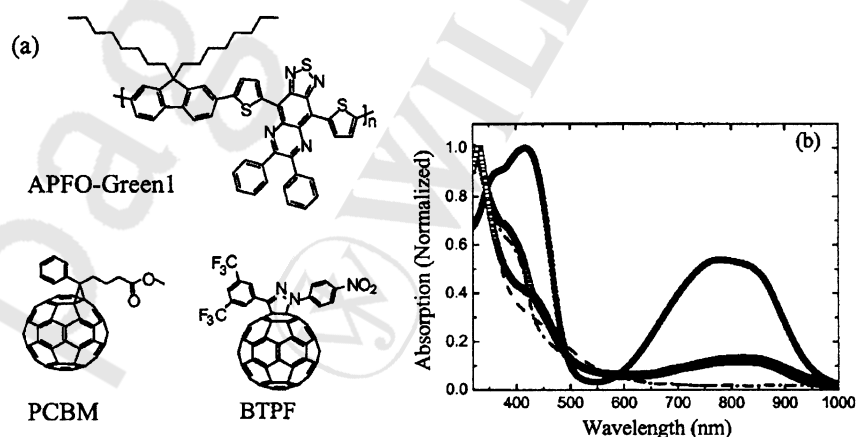

Fig. 11.31 Chemical structures of APFO-Green1, PCBM, and BTPF (a) and photocurrent spectral response of APFO-Green1 : PCBM (1 : 4) (open circles) and APFO-Green1 : BTPF (1 : 4) (solid circles)-based solar cells (b). (Reproduced with permission from [138]).

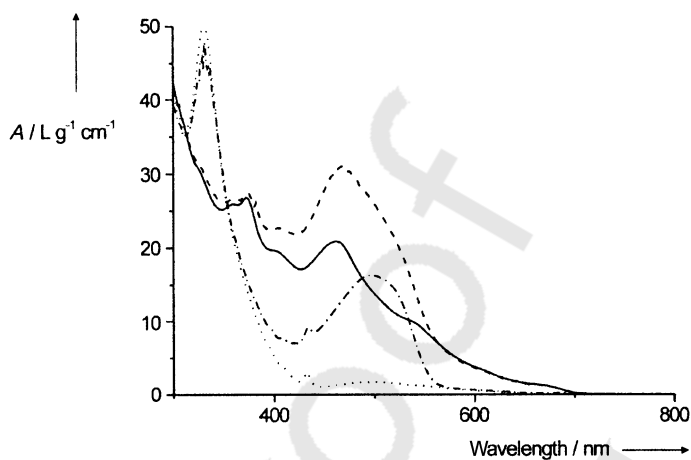<QA>7. Figure legend Fig. 11.31 / Please define APFO and BTPF.

Fig. 11.32 UV–Vis spectra of [70]PCBM (solid line) and [60]PCBM (dots), both in toluene. To illustrate the contribution of MDMO-PPV to the absorption, the normalized spectra of MDMO-PPV:[70]PCBM (dashes) and MDMO-PPV:[60]PCBM (dashes-dots) (1:4) in toluene are presented as well. (Reproduced with permission from [140]).

cation of a Wang et al. suggestion [17]: Wienk et al. synthesized a PCBM based on C_{70} in order to exploit the larger absorption spectra of this molecule compared to C_{60} [140]. While the low absorption of C_{60} derivative can be attributed to a high degree of symmetry making the lowest energy transition forbidden, the breakage of symmetry in C_{70} allows this transition, which drastically increases the light absorption in the visible (Fig. 11.32) [141]. Thus, values of I_{SC} about 7.6 mA cm^{-2} were measured on a MDMO-PPV:[70]PCBM (1:4 ratio) indicating a 50% increase of the SC current compared to optimized MDMO-PPV:[60]PCBM.

Nonetheless, in spite of widespread effort to enlarge the absorption spectrum of the photoactive materials, the best bulk-heterojunction solar cells achieved so far are based on P3HT:PCBM blends, duly annealed [126–128].

<QA>31 Please check number of refs.

Beyond chemical considerations, other concepts can be explored to enhance the light harvesting. For example, light-trapping systems have been proposed to increase the number of photons absorbed at wavelengths where the active materials can harvest the light, yet they do not allow better absorption toward the red [142–144]. Moreover, it should be noted that bulk-heterojunction solar cells are complex optical systems, comprising a thick transparent substrate on which several semitransparent layers with different refractive indices [145] are stacked. This structure ends with a strongly reflective metallic electrode. Therefore, as in the case of bilayer device, constructive and destructive optical interferences occur within the device [146]. A careful optimization of layer thicknesses is necessary to place the maximum of the optical field in the photoactive material and maximize absorption of incident photons [147].

11.4.3
Morphology of the Photoactive Donor: Acceptor Blends

Excitons photogenerated in the donor (D) or the acceptor (A) material, only dissociate and release some free charge carriers at the very D–A interface. In order to ensure a maximized charge generation, D–A dyads [148, 149] and so-called double-cable D–A polymers [150, 151] were synthesized and incorporated in solar cells devices.

On the bulk-heterojunction side, over the last 5 years numerous studies have focused on the morphology, in order to understand and enhance the device performances. Shaheen et al. observed that by optimizing the solvent used to spin cast a blend of MDMO-PPV:PCBM, a doubling of the efficiency of the solar cell could be achieved [97]. This effect appeared to be directly induced by the modification of the morphology of the active blend: using toluene leads to a coarse phase separation whereas chlorobenzene allows the formation of a much finer morphology. Further investigations have confirmed these observations. Hoppe et al. reported that phase separation can be observed for a MDMO-PPV:PCBM ratio as low as 2 when prepared with toluene (Fig. 11.33) [152]. In this case, PL signal from PCBM was detectable, indicating that the 200–500 nm clusters might be almost pure PCBM [152], whereas the matrix might contain a mixture

<QA>23. 11.4.3 Excitons photogenerated in the donor / Please check that the meaning of this sentence is the one you intended (I have removed the word "do").

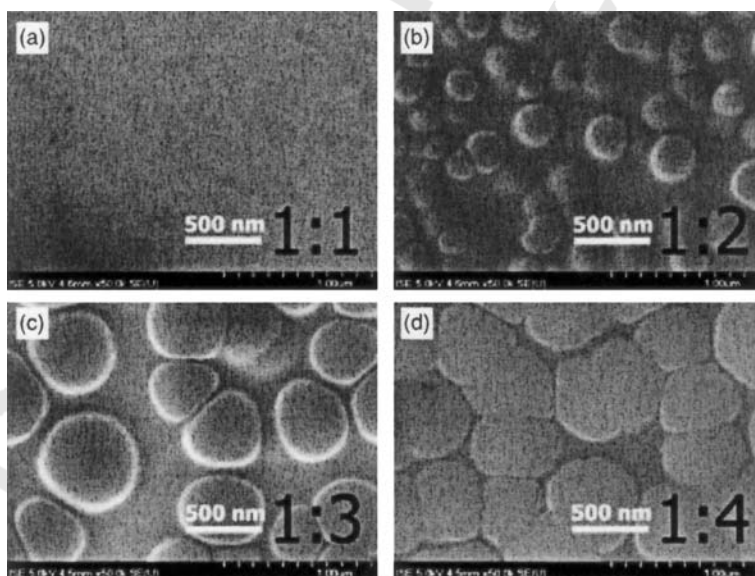**Fig. 11.33** Top views of films cast from toluene with various weight ratios of MDMO-PPV to PCBM realized with a scanning electron microscope. The surface of the 1:1 film (a) appears flat and does not show any features. For the films containing a larger amount of PCBM (b–d), nanoclusters are visible, increasing in size with increasing PCBM concentration. (Reproduced with permission from [152]).

of polymer and fullerene [153]. This statement has been substantiated by transmission electron microscopy (TEM), as shown in Fig. 11.34 [154]. The strong contrast observable in Fig. 11.34 arises from the higher electron-scattering density of PCBM than that of MDMO-PPV [155]. Despite the films spin cast from toluene and chlorobenzene showing drastically different morphologies, the Debye-Scherrer rings observed indicate that the crystalline structure of PCBM is the same in both films [154]. Systematic studies of the morphology of MDMO-PPV : PCBM blends cast from chlorobenzene versus PCBM concentration revealed that phase separation occurs as well, but for much higher PCBM content. Figure 11.35 indicates that while the mixture looks homogeneous for PCBM concentration up to 70% (in weight), large PCBM-rich clusters of densely packed PCBM nanocrystals appear for higher PCBM amounts [154, 156]. This appearance of clusters coincides with a drastic onset of the SC current observed in the operating device [119].

An important question for solar cell application resides in the thermal stability of the morphology of these blends. Yang et al. investigated the effect of different annealing conditions on MDMO-PPV : PCBM blend morphology spin cast from chlorobenzene solutions [154]. It appeared that treatments at 60 °C induce
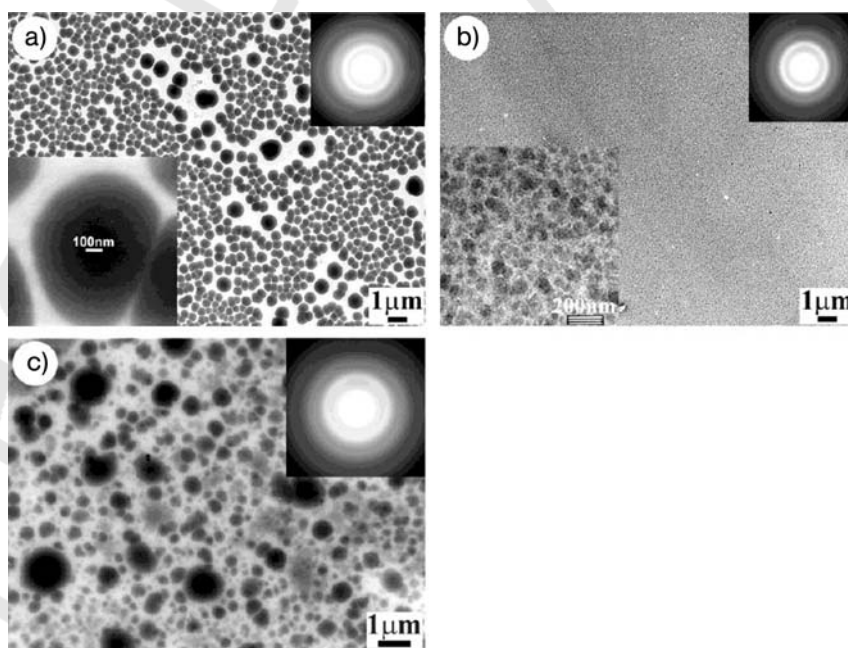

Fig. 11.34 Bright-field transmission electron microscope images of MDMO-PPV : PCBM films (1 : 4 weight ratio) prepared by spin coating from toluene (a) and chlorobenzene (b) and by drop casting from chlorobenzene (c). The *insets* represent the corresponding selected-area electron diffraction (SAED) patterns. (Reproduced with permission from [154]).
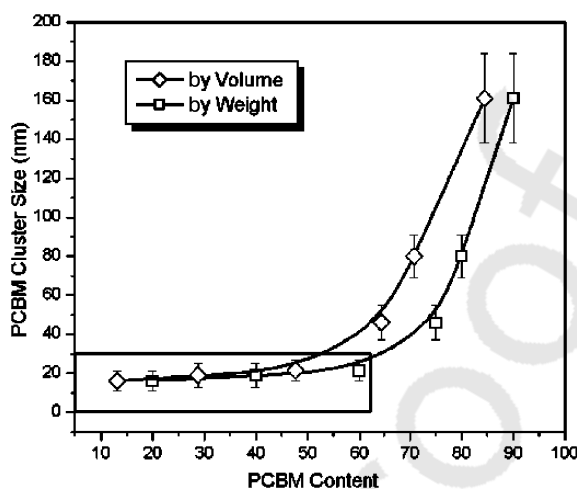
Fig. 11.35 Plot of the average size of PCBM-rich domains in MDMO-PPV:PCBM films spin coated from chlorobenzene solution versus the PCBM concentration in percentage weight and in percentage volume. The specific densities of MDMO-PPV ($\rho = 910$ kg/m^3) and PCBM ($\rho = 1500$ kg/m^3) films were used to convert weight into volume. The solid lines are guides to the eye. (Reproduced with permission from [154]).

a migration and agglomeration of PCBM molecules into large clusters. For higher temperatures (about 100 °C) monocrystals of several micrometers in length can be detected. This migration can even, in certain cases, induce the appearance of pinholes in the active layer [152]. It could then be concluded that PCBM tends to diffuse in the amorphous MDMO-PPV matrix. The morphology obtained by spin coating is frozen in a metastable equilibrium that does relax with time and temperature. This explains as well why techniques with slower solvent evaporation like drop casting lead to coarser morphologies (Fig. 11.34).

The effect of temperature treatment on the performances of P3HT:PCBM solar cells has been the object of numerous studies since the first report of drastic enhancement upon annealing [120]. Despite some discrepancies concerning the optimum time and duration of the treatment, all the reports agree on the positive effect of heat treatment that can increase the overall efficiency of the cells by 50% [127, 128, 157]. This effect was shown to be less marked in the case of films spin cast from low-evaporation solvents [157, 158]. Moreover, electron and hole transport have been observed to be less dispersive and their respective mobility slightly higher after thermal treatment [159]. Several different explanations for this effect have been proposed. TEM studies on pristine and annealed blend have revealed clear morphological changes upon annealing [160]. Figure 11.36 shows that P3HT:PCBM (1:1) films spin cast from 1,2-dichlorobenzene (DCB) is composed of fibrillar-like P3HT crystals embedded in a matrix believed to be made of nanocrystals of PCBM and amorphous P3HT. Upon annealing at 120 °C for 60 min, the length of these fibrils increases by 50%, indicating an

Fig. 11.36 Transmission electron microscopy (TEM) images showing (a) the overview, (b) a zoom in, and (c) the corresponding schematic representation of a pristine photoactive layer of a P3HT/PCBM plastic solar cell. The *inset* is the corresponding SAED pattern. (Reproduced with permission from [160]).

increased crystallinity of P3HT (Fig. 11.37) [128, 160]. Moreover, the darker phase on the TEM image suggests a slight demixing of the PCBM, that tends to cluster. This phase separation and the increase in P3HT crystallinity might explain the enhancement of the transport of charge carriers after the treatment [128]. But another effect might contribute to the overall enhancement of the solar cell performance. Indeed, it has been reported that the amelioration of the device quality is much larger when the annealing step is performed after the deposition of the metallic top electrode [128]. This observation suggests that a better contact between the top electrode of the photoactive blend is achieved, probably due to metal diffusion or direct chemical reaction [161].

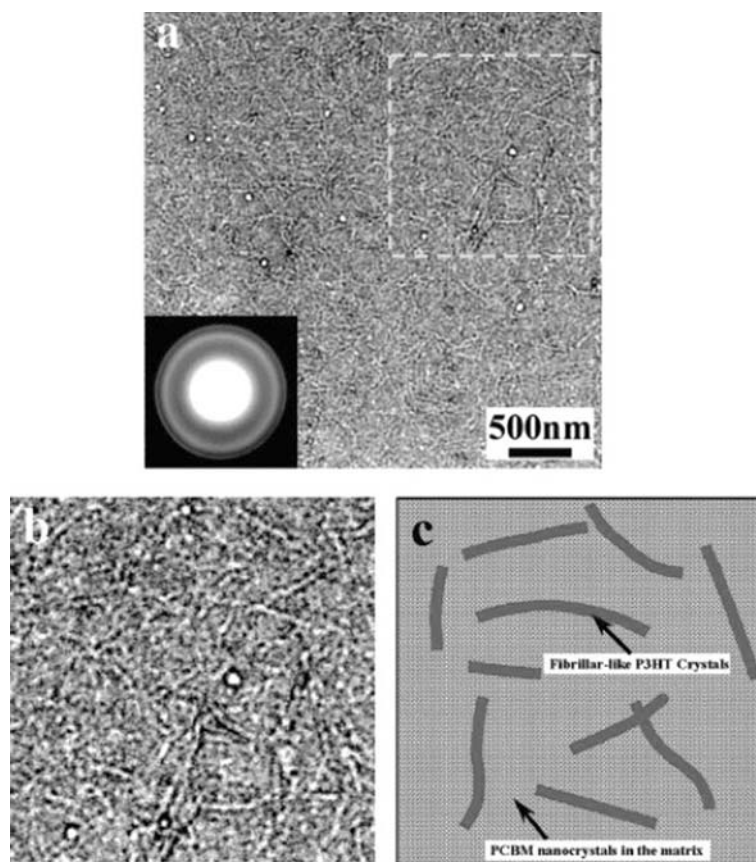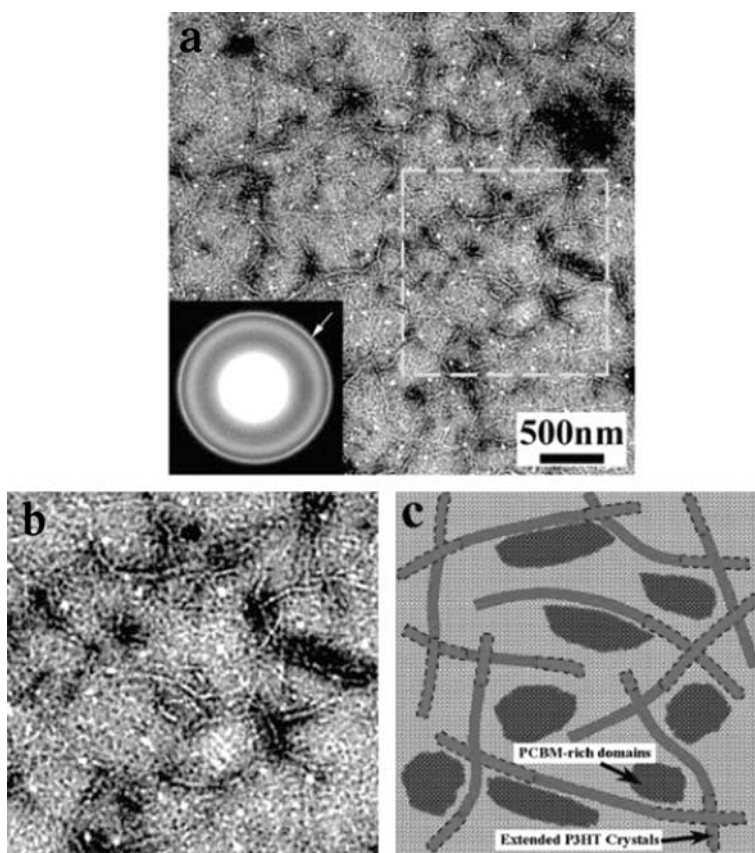**Fig. 11.37** TEM images showing (a) the overview, (b) a zoom in, and (c) the corresponding schematic representation of a thermal annealed photoactive P3HT:PCBM layer. The inset is the corresponding SAED pattern. The arrow indicates the increased intensity of (020) Debye–Scherrer ring from P3HT crystals compared to the SAED pattern shown in the inset of. In (c), the dash-line bordered regions represent the extension of existing P3HT crystals in the pristine film or newly developed PCBM-rich domains during the annealing step. (Reproduced with permission from [160]).

<QA>32 Please give reference to figure.

11.4.4
Charge-Carrier Transport in Bulk-Heterojunction Blends

Once free charge carriers have been created within the photoactive blend, they have to be extracted to participate in the energy conversion. This extraction depends on the mobility of the charge carriers, and on their probability of recombining before they reach the electrodes. Both parameters will be discussed below.

11.4.4.1 **Charge-Carrier Mobility**

Since this topic is largely detailed in another chapter of this book, we will only briefly address it herein, and focus mainly on its study in the case of conjugated polymer: fullerene bulk heterojunctions.

Although other phenomenological formalisms like the Marcus-type jump [162] can be used, the hopping rate between localized states is generally described by the Miller-Abrahams form [163]:

$$v_{ij} = v_0 \exp\left(-2\gamma a \frac{\Delta R_{ij}}{a}\right) \left\{ \begin{array}{ll} \exp\left(-\dfrac{\varepsilon_j - \varepsilon_i}{kT}\right) & \varepsilon_j > \varepsilon_i \\ 1; & \varepsilon_j < \varepsilon_i \end{array} \right. \tag{5}$$

where v_{ij} is the hopping rate between site i and j with energy ε_i and ε_j, v_0 is the attempt-to-jump frequency, a is the Bohr radius or "localization radius" of the charge, and $\Delta R_{i,j}$ is the spatial separation of sites i and j. The first exponential in Eq. (5) describes the electronic wavefunctions overlap, and the second describes a Boltzmann factor for sites upwards in energy. Equation (5) postulates that charge-carrier hops to sites higher in energy are thermally activated, and are accelerated by the electric field. Thus, the mobility of charge carriers is often expressed by the empirical equation [164]:

$$\mu(E, T) = \mu(0, T) \cdot \exp(\gamma\sqrt{E}) \tag{6}$$

where $\mu(0, T)$ is the zero-field mobility. A prefactor that accounts for the Poole-Frenkel effect in disordered materials [165], γ, is given by [166]:

$$\gamma = \left(\frac{1}{k \cdot T} - \frac{1}{k \cdot T_0}\right) \cdot B \tag{7}$$

where T_0 and B are constant. The zero-field mobility, $\mu(0, T)$, is yielded by:

$$\mu(0, T) = \mu_0 \cdot \exp\left(-\frac{\Delta}{k \cdot T}\right) \tag{8}$$

where Δ is the activation energy. Experimentally, the Arrhenius type dependence of $\mu(0, T)$ as been reported several times for pure polymers like PPV derivatives [167, 168].

Alternatively, the temperature and electric-field dependence of mobility can be analyzed within the framework of the disorder formalism [56], which yields:

$$\mu(T, E) = \mu_0 \exp\left[-\frac{2}{3}\left(\frac{\sigma}{kT}\right)^2\right] \exp\left\{ C\left[\left(\frac{\sigma}{kT}\right)^2 - \Sigma^2\right] E^{1/2} \right\} \tag{9}$$

where σ is the width of the Gaussian density of states, Σ is a parameter characterizing the positional disorder, μ_0 is a prefactor mobility in the energetically disorder-free system, E is the electric field, and C is a fitting parameter. This

formalism attributes the temperature and the electric-field dependences of the mobility to two main parameters, namely the energetic and the positional disorders. The former is related to the width σ of the Gaussian DOS normalized to kT. The latter, on the other hand, arises from fluctuation of the intersite coupling, either due to variation of intersite distance between the charge transport sites, or simply the variation of the overlap between corresponding electronic orbitals. Equation (9) predicts a non-Arrhenius-type activation of the mobility extrapolated to zero electric field following [169, 170]:

$$\log[\mu(0, T)] \propto \frac{1}{T^2} \tag{10}$$

and a potentially negative field dependence of the mobility, experimentally observed by Mozer et al. in the case of P3HT [171].

In the case of bulk-heterojunction solar cells based on conjugated polymer : fullerene blends, the study of the charge-carriers' mobility in the respective phases sounds mandatory. Interestingly, the onset of the photocurrent versus the acceptor concentration has been found to be shifted compared to the quenching of the PL of the donor. This effect was interpreted in term of three-dimensional percolation of fullerene molecules [89] offering a continuous path for the electrons to reach their extracting electrode. In the case of pristine materials, electron mobility in PCBM and hole mobility in MDMO-PPV has been reported to be about 10^{-3} cm^2 V^{-1} s^{-1} [172] and 10^{-6} cm^2 V^{-1} s^{-1} [93, 173], respectively. However, when blended together, PCBM and MDMO-PPV can yield almost balanced hole and electron mobilities [174, 175]. Figure 11.38 illustrates the evolution of these mobilities versus the ratio PCBM/MDMO-PPV. One can observe that both electron and hole mobilities do increase by 2 orders of magni-

<QA>24. 11.4.3.1 This effect was interpreted i / Please check my insertion of "path"
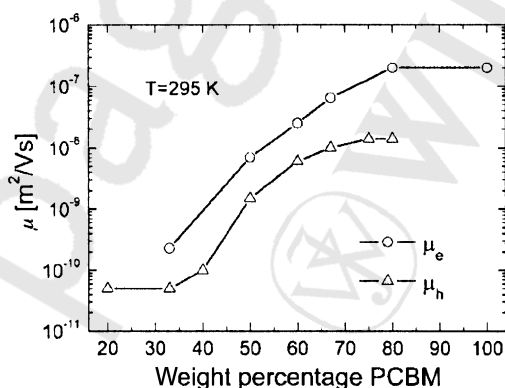

Fig. 11.38 Electron (μ_e) and hole (μ_h) zero-field mobility in MDMO-PPV : PCBM blends as a function of PCBM concentration, at room temperature (295 K). The mobilities were calculated from space-charge-limited currents. (Reproduced with permission from [204]).

tude upon increasing the PCBM concentration. While the increase in electron mobility can be interpreted in terms of decreasing distance between transporting sites, the increase in hole mobility still remains unclear. Pacios et al. proposed that a change in the film morphology upon increasing the PCBM concentration may result in an enhanced intermolecular interaction between polymer chains, and hence in an improved charge transfer between adjacent molecules [176]. The same type of study revealed that hole mobility also increases with increasing PCBM concentration in the case of polyfluorene [177], yet the opposite trend was observed for P3HT : PCBM blends [178, 179].

Finally, we should mention that the charge-carrier mobility in disordered organic semiconductors has been proposed to depend on the charge-carrier concentration. Tanase et al. have reported that the several-orders-of-magnitude-higher charge-carrier mobility observed in field-effect transistors than in LEDs can originate from the increased charge-carrier mobility at higher charge-carrier densities, especially $> 10^{16}$ cm^{-3} [180]. Similarly, it was demonstrated that the enhanced space-charge-limited current in poly(p-phenylenevinylene) diodes at higher applied voltages is due to the enhancement of the charge-carrier mobility at higher charge-carrier densities rather than the effect of the (positive) electric-field dependence of mobility as previously assumed [181]. On the other hand, Arkhipov et al. argued that the mobility may also decrease in disordered materials with increasing charge-carrier concentration due to the effect of additional Coulomb traps introduced by charge-carrier doping [182].

11.4.4.2 Recombination of Charge Carriers

The overall number of charge carriers contributing to the PV effect is dictated by the competing effects of charge-carrier generation and charge-carrier recombination, as expressed in Eq. (27). The kinetics of charge-carriers' recombination can be of two different natures, namely monomolecular (first order) or bimolecular (second order), according to:

$$\frac{dn}{dt} = -\alpha \cdot n - \beta \cdot n^2 \tag{11}$$

where α and β are the monomolecular and bimolecular recombination coefficient, respectively.

First estimation of the limiting recombination regime is usually carried out by investigating the light-intensity (P_{Light}) dependence of the SC current.

$$J_{\text{SC}} \sim P_{\text{Light}}^{\theta} \tag{12}$$

$\theta = 1$ suggests a monomolecular regime, while $\theta = 1/2$ leads to the conclusion of a bimolecular-recombination-controlled kinetics [183]. In the case of MDMO-PPV : PCBM device Riedel et al. reported $\theta \sim 0.94$ at 320 K, concluding a mainly first-order recombination kinetics [184] induced by defects and impurities. How-

ever, it has been recently proposed that linear dependence can also be found when the bimolecular regime dominates [185].

But more detailed considerations of the recombination kinetics have to take into account that solar cells are not meant to be operated under the SC condition, but rather between SC and OC conditions, that is under reduced electric field. It is commonly accepted in this case, that the extended Coulomb radius r_c – expressed by

$$r_c = \frac{e^2}{4 \cdot \pi \cdot \varepsilon \cdot \varepsilon_0 \cdot k \cdot T} \tag{13}$$

where e is the electron charge, ε (ε_0) the relative (absolute) dielectric permittivity, k the Boltzmann constant, and T the temperature – induces highly probable bimolecular recombination between an electron and a hole. Indeed, taking $\varepsilon \approx 3$ in the case of MDMO-PPV:PCBM blend yields a value of r_c close to 15 nm, which considerably enlarges the recombination cross section compared to inorganic materials.

Schultz et al. followed the decay of the light-induced electron spin resonance (LESR) signal of PCBM$^-$ and PPV$^+$ after photoexcitation of a 90% MDMO-PPV:10% PCBM blend at 40 K [186]. As illustrated in Fig. 11.39, they observed a persistent signal extending to several hours, independently of the temperature within the range 10–40 K. They explained this phenomenon in terms of direct tunneling of randomly distributed trapped carriers, as proposed by Shklovskii et al. [187].

Montanari et al. employed time-domain transient absorption spectroscopy (TAS) to investigate the decay of MDMO-PPV$^+$ charges in MDMO-PPV:PCBM blends [188]. As shown in Fig. 11.40, the authors reported that the decay dynamics can be approximated by two distinct regimes: a first fast component
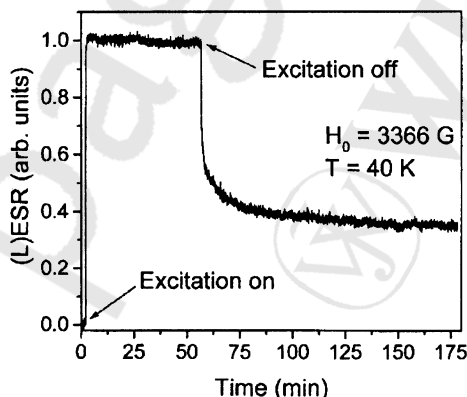

Fig. 11.39 Rise and decay of the PCBM-related LESR signal in MDMO-PPV:PCBM blends after the photoexcitation has been turned on and off, respectively. (Reproduced with permission from [186]).

(several tens of nanoseconds) dependent upon excitation density, and a second slower component that exhibits a power-law decay obeying:

$$\Delta OD \sim t^{-\theta} \tag{14}$$

where ΔOD is the variation of the optical density, and $\theta = 0.4$ at 300 K (0.3 at 200 K). This second component was found (a) to extend up to the millisecond range, (b) to depend on light intensity up to a certain threshold (~1 μJ cm^{-2}), (c) to be independent of the PCBM content in the blend, and (d) to be thermally active (Fig. 11.41) [189]. Nelson et al. interpreted these results in the framework of a model based on Miller-Abrahams formalism [163], driving thermally activated diffusion of MDMO-PPV$^+$ towards PCBM$^-$ [190], and neglecting any coulombic interactions between the charges. According to this model, the distinct slow and fast regimes appear because of a bimodal DOS: localized charge carriers evolving in the deep levels of the exponential DOS recombine much more slowly than the ones located above the mobility edge of MDMO-PPV. Monte Carlo calculations allowed the evaluation of localized states to about 10^{17} cm^{-3}, which explained the saturation of the slow regime for high light intensities. Moreover, the lifetime of the charge carriers was evaluated to 10 μs, independently of the ratio MDMO-PPV:PCBM. This model was found to hold for temperatures down to 200 K, and predicts purely tunneling-driven recombination kinetics for very low temperatures as suggested by Schultz et al. Thus, Nelson et al. concluded that recombination kinetics are dominated by second-order effects.

It should be mentioned that the same type of measurements had been performed earlier by Meskers et al. on a P3HT:PCBM blend. Though less detailed, these studies revealed the same type of decay, showing a power law with an exponent 0.2 (80 K) for the slowest component [191].

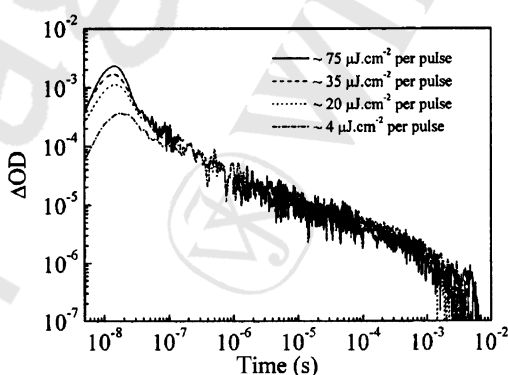

<QA>8. Figure legend Fig. 11.40 / Please define ΔOD

Fig. 11.40 Transient absorption decay kinetics (collected at 940 nm) observed for a MDMO-PPV:PCBM blend on the nanosecond-to-millisecond timescale. (Reproduced with permission from [188]).
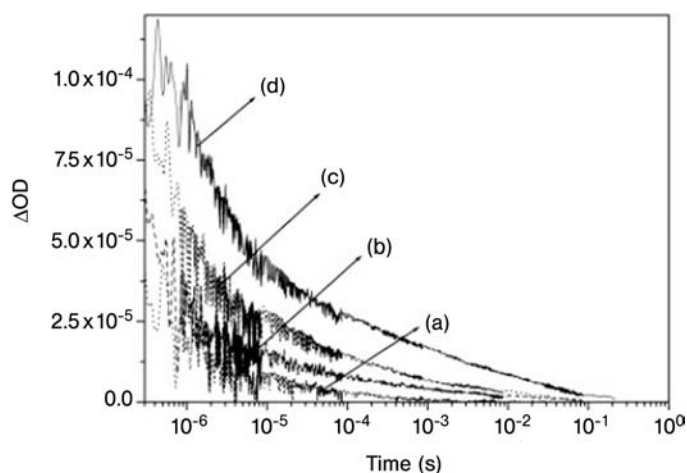
Fig. 11.41 Transient absorption kinetics (collected at 940 nm) observed for a MDMO-PPV:PCBM (1:4) blend as a function of sample temperature: *a* 300 K, *b* 220 K, *c* 150 K, *d* 80 K. Excitation intensity of 70 μJ m^{-2} per pulse. *OD* Optical density. (Reproduced with permission from [189]).

The assignment of distinct fast and slow phases has been supported by measurements based on flash photolysis time-resolved microwave conductivity (FP/TRMC) [192]. In the case of MDMO-PPV:PCBM blends with high (80%) concentration of PCBM, Savenije et al. reported a second-order kinetics [193]. The same phenomenon was observed in the case of MDMO-PPV blended with a poly(cyanoetherphenylenevinylene) (PCNEPV). Moreover, a slow decay following a power law with an exponent around 0.33 was shown, suggesting an energetic relaxation of charges which perform a diffusional motion in a disordered-energy landscape with an exponential DOS [194].

All the works mentioned above were performed on contactless samples, that is, under conditions relatively far from those of an operating solar cell. Quite recently, a new technique was proposed to study the charge transport in working devices: the photoinduced charge-carrier extraction by linearly increasing voltage technique (photo-CELIV) [195]. Photo-CELIV was shown to allow the determination of charge-carrier mobility, recombination kinetics and lifetime in conjugated polymers [196]. A short laser pulse (nanosecond range) is absorbed by the device to be characterized; the charge carriers created are forced to recombine in the device thanks to an offset bias applied to compensate the V_{OC} of the solar cell, which ensures flat-band conditions; after a certain delay time τ_{del}, the remaining charges are extracted by a linearly increasing voltage applied in the reverse, noninjecting polarization of the photodiode. Mozer et al. used photo-CELIV to study charge transport in a MDMO-PPV:PCBM (1:4) blend sandwiched between ITO and Al [175]. The authors reported a purely bimolecular recombination kinetics under flat-band conditions, with a decay of charge carriers obeying the equation:

$$n(t) = \frac{n_0}{1 + (t + \tau_B)} \quad \text{with } \tau_B = \frac{1}{n_0 \cdot \beta} \tag{15}$$

where n_0 is the number of charge carriers at $t=0$, τ_B is the bimolecular lifetime, and β is the bimolecular recombination coefficient. Such decays clearly distinguish themselves from straight lines (simple power law) in log–log graphs. Figure 11.42 exhibits mobility and charge-carrier concentration decay measured for 20% MDMO-PPV:80% PCBM blends at different temperature [169]. The time-dependent mobility was explained by a thermalization effect inducing an energy relaxation of the charge carriers towards the tail-states of a Gaussian DOS. During this thermalization, the diffusion coefficient D decreases as well, and a dispersive recombination dynamics appears. According to the diffusion-controlled theory of Smoluchovsky et al., the bimolecular recombination coefficient β can be expressed by

$$\beta = 4\pi f R D \tag{16}$$

where f is the fraction of charge annihilated after encounter, R is the charge interaction radius and D is the sum of the charge-carrier diffusion coefficient [197]. Thus, a time-dependent diffusion coefficient $D(t)$ gives rise to a time-dependent bimolecular recombination coefficient:

$$\beta(t) = \beta_0 \cdot t^{-(1-\gamma)} \tag{17}$$

where β_0 and γ are time-dependent parameters, γ accounting for the dispersive character of the dynamics. The Eq. (15) has to be modified, according to:

$$n(t) = p(t) = \frac{n(0)}{1 + (t/\tau_B)^\gamma} \tag{18}$$

where τ_B, called the "effective" bimolecular lifetime, can be expressed as follows:

$$\tau_B = \left(\frac{\gamma}{n(0) \cdot \beta_0}\right)^{\frac{1}{\gamma}} \tag{19}$$

The solid line visible in Fig. 11.42 are fits obtained with Eq. (18), showing a good agreement between the dispersive bimolecular recombination model and the experimental data. The parameter γ was found to evolve from 0.4 to 1 (non-dispersive limit, see Fig. 11.43) and τ_B from 319 μs to 4 μs, with temperature increasing from 120 to 300 K. Finally Mozer et al. concluded a Langevin-type bimolecular recombination, in good agreement between the Langevin bimolecular recombination $\beta_L = e\mu/\varepsilon\varepsilon_0$ [198] and the values of β extracted from the data. Dennler et al. performed the same type of investigation on a MDMO-PPV:PCBM blend with PCBM ratios between 0 and 80% [199]. They confirmed a Langevin-type dispersive bimolecular recombination dynamics for all the
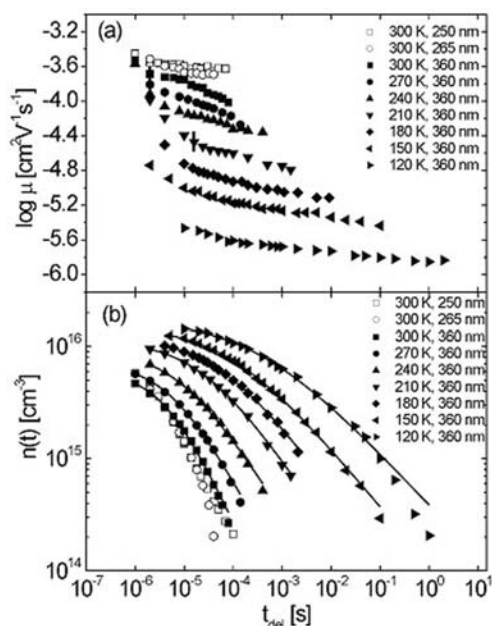
Fig. 11.42 Mobility values (a) and concentration (b) of extracted charge carriers versus time for samples with different active-layer thickness. The mobility and concentration values measured for the 360 nm device at various temperatures are also displayed. (Reproduced with permission from [169].

<QA>9. Figure legend Fig. 11.42 / Please define t_{del}
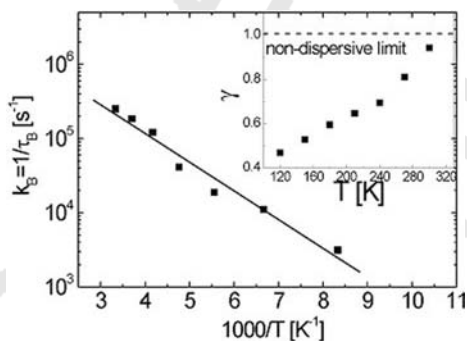
Fig. 11.43 Arrhenius plot of the "effective" bimolecular recombination rate k_b The *inset* shows the temperature dependence of the dispersion parameter γ. (Reproduced with permission from [169]).

blends investigated and reported a constant product $\mu \times \tau_B$, μ evolving from 3×10^{-6} to 3×10^{-4} cm^2 V^{-1} s^{-1} and τ_B from 120 to 2 μs with increasing PCBM concentration. Interestingly, n_0 was found to be independent of the PCBM content, as reported by Nelson et al. for the slow-decay regime.

Although Langevin-type bimolecular recombination is expected to dominate in low-mobility materials where the coulombic radius is larger the hopping distance [200], surprising results have recently been reported. While bimolecular recombination has been shown to be of Langevin nature in regiorandom P3HT [201, 202], PPV [173] and in MDMO-PPV:PCBM blends [169, 199], the situation is very different in P3HT:PCBM blends. Indeed, Pivrikas et al. measured a ratio β/β_L of about 10^{-4}, indicating bimolecular recombination kinetics 4 orders of magnitude slower than expected [203]. This phenomenon is not yet understood, and is still under investigation.

Finally, as mentioned above, several works based on models fitting steady-state solar cells I–V curves concluded that Langevin-type diffusion-controlled bimolecular recombination dynamics does dominate in operating solar cells [185, 204].

11.4.5
Modeling Bulk-Heterojunction-Device Operation

All the important processes taking place in bulk-heterojunction cells and contributing to the energy conversion can be incorporated into a device model. Such a model is highly desirable since it could allow the determination of the factors limiting the overall performance of the device, and estimate the potential of materials and device geometries. However, the incorporation of all influencing physical aspects render the realization of efficient models quite complex. We have chosen to present here several relatively simple approaches proposed in the literature, but beyond our nonexhaustive selection, other interesting formalisms can be found [185, 190], considering, for example, the degree of intermixing of the donor and the acceptor [205].

11.4.5.1 Simple One-Diode Equivalent Circuit
The simple one-diode equivalent circuit, elaborated for p–n inorganic solar cells [206], has been massively applied to bulk-heterojunction solar cells, since it provides a first approximation of the working principle of the device. This model is based on the equivalent circuit displayed in Fig. 11.44 and comprises (a) a diode, (b) a current source, (c) a series resistance R_s, and (d) a parallel resistance R_p. The I–V curve can in this case be expressed by the Shockley equation:

$$I = I_0 \left[\exp\left(\frac{q(V - I \cdot R_s)}{n \cdot k \cdot T} \right) - 1 \right] + \frac{V - I \cdot R_s}{R_p} - I_{\text{Light}} \tag{20}$$

where I is the current flowing in the device, q the elementary charge, V the applied voltage, n the ideality factor of the diode ($n=2$ or below), k the Boltzmann's constant, T the temperature, and I_{Light} the current photogenerated. I_0, the saturation current of the device, is given by [121, 206]:
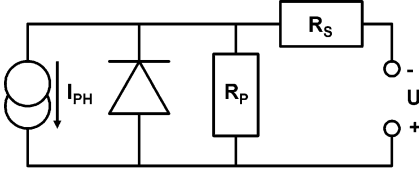
Fig. 11.44 Equivalent circuit used in the simple one-diode model.

$$I_0 = q \cdot N_V \cdot N_C \cdot \exp\left(-\frac{E_G}{kT}\right) \cdot \left(\frac{L_n}{n_n \cdot \tau_n} + \frac{L_p}{n_n \cdot \tau_p}\right) \tag{21}$$

where N_V and N_C are the effective densities of states in the valence and in the conduction bands respectively, E_G is the semiconductor gap, L_n, L_p, n_n, n_p, τ_n, τ_p are the diffusion lengths, the carrier densities, and the lifetimes of electrons and holes, respectively.

In Eq. (20), the term IR_s accounts for the drop of the voltage due to R_s, and the second term or the equation $(V - IR_s)/R_p$ illustrates the current flowing in the parallel resistance. Both R_s and R_p illustrate some internal characteristics of the device. R_s accounts for the resistance of the electrode, the semiconductor-electrode contact, and the active material. Therefore, minimum R_s are required for high efficiency solar cells. It has been reported that R_s decreases with increasing temperature [183], probably due to an increase of the charge-carriers' mobility (Fig. 11.45), but stays constant independently of the light intensity [207]. Moreover, R_s has been shown to scale linearly with the thickness of the semiconductor, suggesting that R_s is primarily governed by the ohmic resistance of the photoactive material [208] when the electrodes are highly conducting
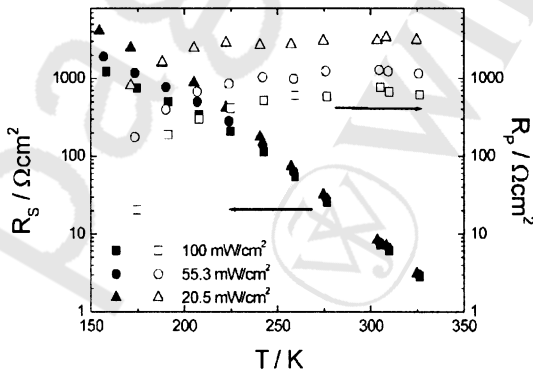
Fig. 11.45 Temperature dependence of series (solid symbols) and parallel (open symbols) resistance of an ITO/PEDOT:PSS/MDMO-PPV:PCBM/Al device, at the indicated light intensities. (Reproduced with permission from [183]).
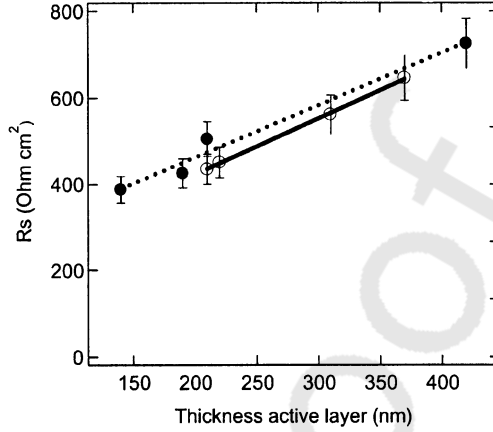
Fig. 11.46 Series resistance versus active-layer thickness in the case of ITO/MDMO-PPV:PCBM/Al with (solid symbols) and without (open symbols) PEDOT:PSS. (Reproduced with permission from [208]).

(Fig. 11.46). On the other hand, R_p aims to implement the leaking character of the diode. Therefore, maximum R_s is required for high efficiency solar cells. R_p was found to decrease linearly with increasing thickness [208], and to be almost constant with varying temperature. Moreover, in contrast to R_s, R_p was observed to decrease drastically with increasing light intensity.

One of the main limitations of Eq. (20) arises from the fact that it does not take into account the voltage dependence of I_{Light} [207]. Indeed, I_{Light} is often taken equal to the SC current. However, subtracting light and dark I–V curves shows that I_{Light} does vary by up to two orders of magnitude between OC and SC conditions [172]. Moreover, the only light-dependent parameter in Eq. (20) is I_{Light}. Since photoactive materials used in solar cells show an important PC, one can expect that the light influences the resistance used in this simple one-diode model.

11.4.5.2 The Extended One-Diode Model

The extended one-diode model has been proposed by Schilinsky et al. to overcome the limitations of the simple one-diode model, as far as voltage dependence of I_{Light} and light dependence of R_p are concerned [126]. This model states that bulk heterojunctions can be considered as intimate mixtures of n- and p-type organic semiconductor, in such a way that the disordered phases in the two-component blend do not determine a distinct diffusion direction for the mobile charges. Therefore, the charge-carrier movement is considered to be dictated by the drift induced by the electric field present in the device. The mean distance covered by a charge carrier is given by:

$$l_{drift} = \mu \cdot \tau \cdot E \tag{22}$$

where μ is the mobility of the charge, τ the lifetime of the charge, and E the electric field present in the device. This latter is expressed by:

$$E = \frac{V - V_{bi}}{d} \tag{23}$$

where V is the applied voltage, V_{bi} is the built-in voltage, and d the thickness of the device. This formalism states that only charge carriers created within the distance l_{drift} to the collecting electrode will be extracted and participate in the photocurrent. Thus, the voltage dependence of I_{Light} is yielded by:

$$I_{Light} = \begin{cases} |I_{SC}| \rightarrow \mu \cdot \tau \cdot \dfrac{V - V_{bi}}{d} \geq d \\ |I_{SC}| \cdot \mu \cdot \tau \cdot \dfrac{V - V_{bi}}{d^2} \rightarrow \mu \cdot \tau \cdot \dfrac{V - V_{bi}}{d} \leq d \end{cases} \tag{24}$$

where the first condition implies that all the carriers are extracted while the second expresses an extraction limited by low mobility, and/or short lifetime, and/or small field.

The second specificity of the extended one-diode model is to take into account the importance influence of the PC on the parallel resistance. As mentioned above, though the light intensity does not influence R_s, R_p drastically decreases with increasing light, which has to be considered for accurate fits. Therefore, Waldauf et al. introduced a so-called photoshunt R_{pLight} expressed as follows [209]:

$$R_{pLight} = \left(\frac{q \cdot P \cdot A \cdot n \cdot \mu}{d} + \frac{1}{R_{PDark}} \right)^{-1} \tag{25}$$

where q is the elementary charge, A the active surface area, and n the light-dependent density of charge carriers, and R_{pDark} the parallel resistance in the dark. P_c, called the permeability of the contact, represents the probability that charge carriers of one type penetrate the barrier presented by the selective electrodes.

This extended one-diode model was shown to fit accurately the voltage dependence of the current flowing in a bulk-heterojunction solar cell, and the light dependence of I–V. Moreover, this formalism not only permits determination of the values of R_s and R_p but also more fundamental parameters such as charge-carrier mobility, lifetime, permeability of electrodes and built-in field.

11.4.5.3 Electric-Field-Assisted Dissociation of Electron–Hole Pairs

Koster et al. [210] and Mihailetchi et al. [211] have recently proposed a model based on the usual transport equations, which are:

- The Poisson equation:

$$\frac{d^2}{dx^2}\psi(x) = \frac{q}{\varepsilon \cdot \varepsilon_0}[n(x) - p(x)] \tag{26}$$

where ψ is the electric potential in the device, and $n(x)$ and $p(x)$ the electron and hole densities, respectively.

- The current continuity equation:

$$\frac{d}{dx}J_n(x) = \frac{d}{dx}J_p(x) = q[G(x) - R(x)] \tag{27}$$

where $J_n(x)$ and $J_p(x)$ are the electron and hole current densities, respectively, $G(x)$ the generation rate of charge carriers, and $R(x)$ the recombination rate of charge carriers.

- The current transport equations for electrons and holes:

$$J_n(x) = -q \cdot n(x) \cdot \mu_n \cdot \frac{d}{dx}\psi + q \cdot D_n \frac{d}{dx}n(x) \tag{28}$$

$$J_p(x) = -q \cdot p(x) \cdot \mu_p \cdot \frac{d}{dx}\psi + q \cdot D_p \frac{d}{dx}p(x) \tag{29}$$

where μ_n and μ_p are the electron and the holes mobility, respectively. D_n and D_p, the electron and hole diffusion coefficient are assumed to obey the Einstein relation:

$$D_{n,p} = \mu_{n,p} \cdot \frac{k \cdot T}{q} \tag{30}$$

The recombination R is considered purely bimolecular:

$$R(x) = \beta \cdot n \cdot p \tag{31}$$

and β is assumed to follow the Langevin law, as suggested by Tessler and Rappaport [212].

<QA>25. 11.4.4.3 The basis / Please check this change.

The basis of this model is to consider that the dissociation of exciton does not directly lead to free charge carriers, but to electron–hole pairs, as proposed by Barker et al. in the case of bilayer solar cells [213]. According to Braun's theory based on Onsager's model [6], these pairs have a finite lifetime before they either decay to the ground state with a decay rate k_f, or dissociate unto free charge carrier with a dissociation rate k_{diss} [214]. The probability of electron–hole pair dissociation, for a given electron–hole pair distance x is given by

$$p(x, T, E) = \frac{k_{diss}(x, T \cdot E)}{k_{diss}(x, T, E) + k_f(T)} \tag{32}$$

and depends on both the temperature and the electric field E, since.

$$k_{\text{diss}}(x, T, E) = \frac{3R}{4 \cdot \pi \cdot x^3} \exp\left(-\frac{E_B}{k \cdot T}\right) \cdot J_1\left(\frac{2\sqrt{-2b}}{\sqrt{-2b}}\right) \tag{33}$$

where E_B is the binding energy of the electron–hole pair, J_1 the Bessel function and

$$b = \frac{q^3 \cdot E}{8 \cdot \pi \cdot \varepsilon_0 \cdot \varepsilon \cdot k^2 \cdot T^2} \tag{34}$$

Thus, in contrast to the field-dependent extraction model presented above, it is assumed here that the photocurrent in bulk-heterojunction solar cells is dominated by the field and temperature dependence of the dissociation of the electron–hole pairs.

The calculations based on this model converge to several specific results. At OC conditions, a nonzero electric field is present in the device in such a way that the drift current equals the diffusion current. For voltages slightly below V_{OC}, the photocurrent is proposed to be dominated by diffusion, and follows a linear dependence with the applied voltage. For conditions getting closer to the SC, the drift phenomenon gains importance, and the generation of free charge carriers is constantly enhanced by the increasing field in the device. In the case of MDMO-PPV:PCBM, about 60% of the electron–hole pairs are estimated to be separated under SC conditions. Finally, at large negative voltages, the photocurrent saturates since all the electron–hole pairs are dissociated.

11.5
From Basics to Applications

11.5.1
Production Scheme

As illustrated in Fig. 11.22, bulk-heterojunction-based devices consist of a quite simple structure made of one photoactive organic layer sandwiched between conductive electrodes. Up to now, the most widely used bottom transparent electrode is ITO deposited by reactive sputtering on either rigid glass or flexible polymer foils like poly(ethyleneterephthalate) (PET). In order to compensate the roughness of this electrode, a layer of PEDOT highly doped with PSS can be applied. On the top of this latter, the active donor–acceptor blend is deposited. Finally, the back electrode is evaporated after having deposited a small layer of LiF, known to enhance the cell performances as mentioned above.

The obvious advantage of plastic solar cells compared to their inorganic counterparts comes from the possibility of producing large-area flexible devices with processing technologies employed in the long-experienced printing indus-

try [215]. While for small samples, the spin casting technique is commonly carried out, large-scale devices call for other approaches like ink-jet printing [216] or doctor blading [217]. Shaheen et al. showed even the applicability of screen printing, paving the route to potentially large-scale and very fast roll-to-roll processing (Fig. 11.47) [218].

Figure 11.48 shows the characteristics of a 6×6 cm flexible cell in comparison to a polycrystalline Si cell in a linear plot, where the I–V characteristics in the 4th quadrant can be seen more precisely for the determination of the FF. Although the polycrystalline Si cell is referenced with 13.3% power efficiency under AM 1.5, one can see clearly that under these specific illumination conditions (10 mW cm^2, 488 nm), efficiency considerably decreases, while the plastic solar cell does still work decently: owing to its low optical density, the plastic solar cells can sustain appreciable performance at low light intensities. This is confirmed by Fig. 11.49 that shows V_{OC}, V_{mpp}, I_{SC} and I_{mpp} for a 0.7 cm^2 flexible MDMO-PPV:PCBM solar cell versus light intensity of a typical fluorescent lamp (comprising four main lines at 545, 485, 435, and 405 nm respectively) [219]. Under AM 1.5 (110 000 Lux of white light), this nonoptimized cell (no LiF, trivial design) delivers a V_{OC} of about 650 mV, a I_{SC} 1.75 mA cm^{-2} and a FF of 0.38. Interestingly, in spite of the logarithmic decrease of V_{OC} with decreasing lighting, V_{mpp} is almost constant with decreasing light intensity. This phenomenon originates in the increase of FF with decreasing illuminance induced by a lower contribution of R_s. Thus, these flexible polymer solar cells can still easily deliver a V_{OC} of about 500 mV at normal indoor fluorescent light intensity (1000 Lux). Moreover, the current intensity that follows a perfect linear evolution with lighting still shows decent values at 1000 Lux (I_{SC} about 4.7 μA cm^{-2}). Thus, such PV cells are suitable for charging batteries of low energy consumption devices like remote controls, watches, small displays, and back-up security systems.

It should be mentioned here that an optimization of the device design is mandatory to achieve high efficiencies over large areas. Indeed, the bottom transparent electrodes usually possess sheet resistance about 10 Ω/square on ri-
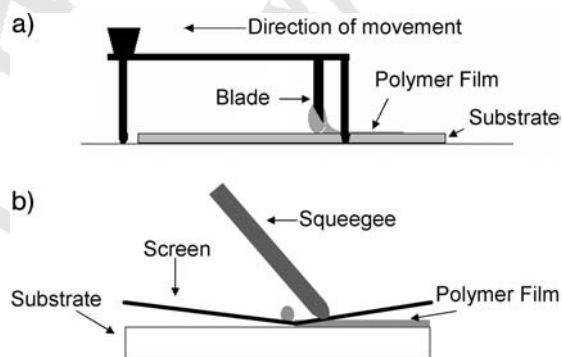
Fig. 11.47 Schemes of the (a) doctor blading and (b) screen printing techniques.
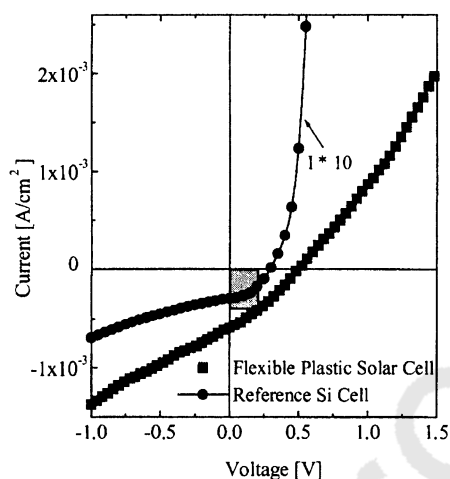
Fig. 11.48 *I–V* characteristic of a large-area conjugated polymer:fullerene solar cell illuminated with 488 nm at 10 mW cm^{-2}. As a reference, the photocurrent of a polycrystalline solar cell is plotted, reduced 10 times. (Reproduced with permission from [215]).
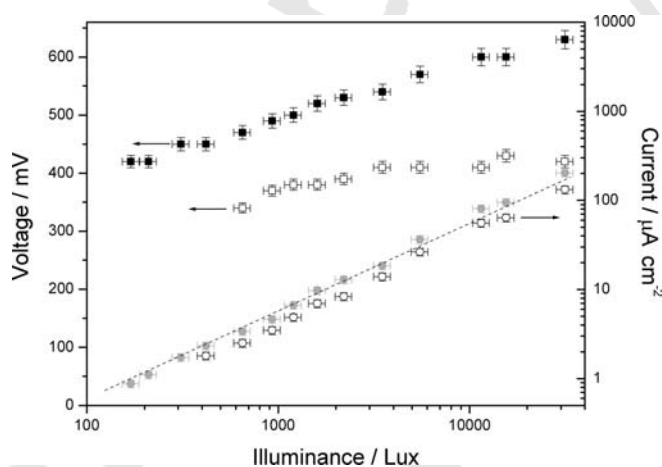
Fig. 11.49 V_{OC} (solid squares), V_{mpp} (open squares), I_{SC} (solid circles) and I_{mpp} (open circles) of a flexible 3×24 mm^2 ITO/PEDOT:PSS/MDMO-PPV:PCBM/Al solar cell under various fluorescent lamp illuminances. (Reproduced with permission from [219]).

gid substrates, and several times larger on flexible substrates. Therefore, the serial resistance induced by this part of the device can dramatically reduce the charge collection. A solution to overcome this problem is to limit the path of the charge carrier in this electrode, that is, to design individual cells that have large width but short length, as in the case of a transistor channel. Further-

<QA>26. 11.5.1 Indeed, the bottom transparent electrodes / Please clarify — ohm per square what?

more, since bulk-heterojunction organic solar cells usually possess a V_{mpp} of several hundred millivolts, the realization of modules delivering several volts need efficient series connection of a large number of individual cells. Such connections, already used to produce inorganic thin-film solar cell modules for a long time, have to ensure minimized surface-area losses, and optimized connection of the anode of one cell to the cathode of the next cell. To achieve such integration, the cells should be precisely aligned and their size perfectly controlled. Moreover, such a process should be compatible with roll-to-roll production at high speed, thus avoiding any masking steps. Different strategies to pattern organic devices have been proposed. They mostly rely on ink-jet printing [216], photolithography [220], soft lithography [221], and laser etching [222].

It has recently been shown that a patterning technique based on Nd:YAG laser etching can easily shape self-aligned series-connected solar cells into large-scale modules [223]. This technique, inspired by the state-of-the-art processing used in amorphous silicon thin-film solar cell production [224], relies on selective etching of the photoactive material and the electrode of the cell. Figure 11.50 shows the absorption spectra of ITO, MDMO-PPV:PCBM blend, and the emission lines of the fundamental and the second harmonic of a Nd:YAG laser. ITO can be etched by the 1064 nm line while the organic photoactive material is much more sensitive to the 532 nm line. This selective absorption allows accessing complex patterns with one single laser without any mask or lithographic operation. Figure 11.51 shows the successive steps for the production of large modules made of series-connected cells:

- deposition of ITO and PEDOT:PSS all over the substrate;
- structuring of the ITO and PEDOT:PSS by ablation with the 1064 nm Nd:YAG laser line to separate the cells;
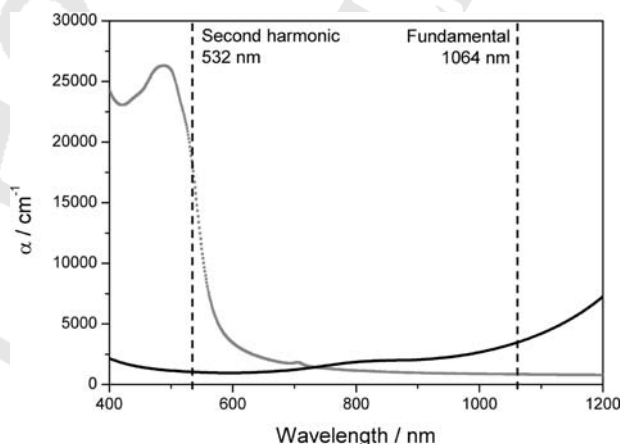
Fig. 11.50 Absorption of ITO (full line) and MDMO-PPV:PCBM (solid squares) compared to the fundamental and second harmonic of a Nd:YAG laser. (Reproduced with permission from [223]).

<QA>28. 11.5.1 It has recently been shown that a / Did you mean "series-connected" or "series of connected" here? Please check, throughout.
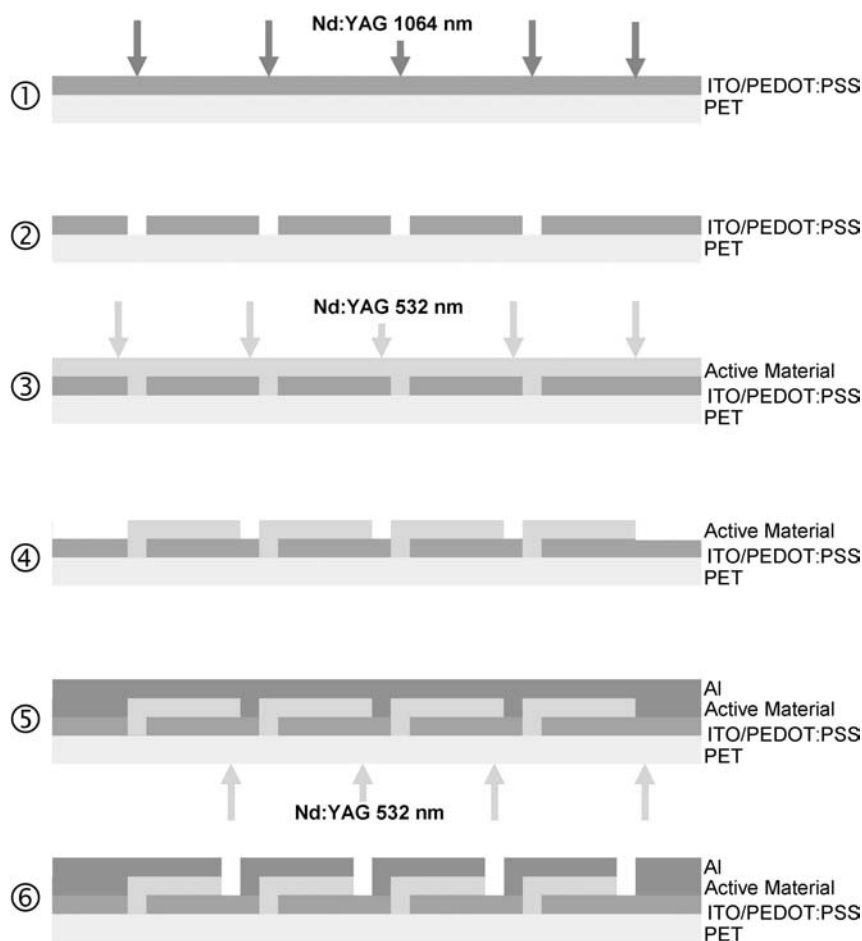
Fig. 11.51 Successive steps of Nd:YAG laser patterning of MDMO-PPV:PCBM-based solar cells connected in series. (Reproduced with permission from [223]).

- deposition of the photoactive material allover the surface of the device;
- Structuring of the MDMO-PPV:PCBM material by ablation with the 532 nm Nd:YAG laser line to open paths to the underlying ITO electrodes;
- deposition of the top electrode all over the surface of the device;
- structuring of the top electrode by lift-off due to ablation of the MDMO-PPV:PCBM blend with the 532 nm Nd:YAG laser to separate the individual cells.

Using a 30-kHz pulsed laser, etching speed up to 300 mm s^{-1} have been achieved, suggesting that this facile way of creating tightly packed series-connected cells might be entirely compatible with roll-to-roll processes [223].

<QA>27. 11.5.1 Structuring of the MDMO-PPV:PCBM / Please check this change.

11.5.2
Encapsulation of Flexible Solar Cells

Conjugated polymers such as poly(*p*-phenylenevinylene) (PPV) are known to be rather unstable in air [225], being particularly susceptible to photodegradation induced by oxygen and moisture [226, 227]. The mechanism involves the binding of oxygen atoms to vinyl bonds, which breaks the conjugation and leads to the formation of carbonyl groups [228, 229]. Spectroscopic ellipsometry studies showed that during simultaneous exposure to air and light, the thickness of the active layer increases while its refractive index and absorption coefficient drastically decrease [230]. Moreover, the material for the low-work-function electrode is usually chosen from metals like Al and Ca, in order to maximize the OC voltage of the solar cells, as explained above. These metals rapidly undergo oxidation when exposed to air. This leads to the formation of thin, insulating oxide barriers [231], hindering electric conduction and collection of the charge carriers. Besides, it has been reported that water can affect the interface between the metallic contact and organic semiconductors by an electrochemical process that causes delamination of the electrode [232]. This effect is directly connected to the formation of dark spots in OLEDs.

While all these phenomena drastically complicate the use of OLEDs in air, conjugated polymer : fullerene blends have been shown to be slightly less sensitive than pure conjugated polymer. Neugebauer et al. studied the degradation of MDMO-PPV, PCBM, and blend of the two materials by attenuated total reflection/Fourier transform infrared (ATR/FTIR) [233]. The authors observed that the MDMO-PPV signal decreases by 50% within 5 h under illumination and pure oxygen atmosphere. However, when mixed with an electron acceptor, the stability of the MDMO-PPV is drastically increased. This effect can be explained by two distinct effects. Firstly, since the electrochemical potential of the photoexcited state of conjugated polymer is relatively high, it might immediately lead to direct electrochemical interactions with oxygen and water vapor present in its vicinity. The ultrafast electron transfer from the LUMO of the conjugated polymer to the LUMO of the acceptor empties the excited state of the polymer and lowers the electrochemical energy of the excited electron. Secondly, the intersystem crossing of the polymer can produce triplet excited states that may create singlet oxygen by energy transfer [234]. This highly reactive form of oxygen is expected to react with the polymer backbone creating carbonyl type defects. As shown above, the ultrafast photoinduced electron transfer does quench the inert-system crossing to the triplet state, hindering this degradation route.

Several studies have focused on the lifetime investigation of conjugated polymer : fullerenes solar cells. In the case of MDMO-PPV : PCBM cells encapsulated between glass plates, Neugebauer et al. reported a decrease of 40% of the V_{OC} and 60% of the I_{SC} within 3000 h, whereas unprotected cells last only couple of hours (Fig. 11.52, [233]). Accelerated lifetime test showed that the degradation is about 10 times faster at 80 °C than at 25 °C [235]. Moreover, the degradation was found to be influenced by some morphological components. Indeed, Jeranko et
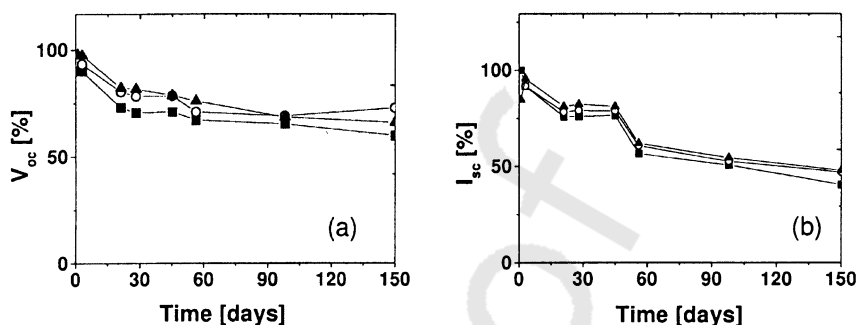
Fig. 11.52 V_{OC} (a) and I_{SC} (b) of ITO/MDMO-PPV:PCBM/Al cells encapsulated between rigid glass plates versus storage time (shelf lifetime). (Reproduced with permission from [233]).

al. investigated the aging effect by photocurrent imaging, which revealed the formation of islands of higher efficiency [236]. Finally, deterioration of the electron-collecting electrode–polymer interface has been proposed as a determining factor [237, 238]. Several attempts have been tried to reduce the degradation of the active materials, by replacing the easily oxidized Al by more stable Au [239], or by blending the photoactive polymer with a potentially protecting host matrix [240]. However, efficient encapsulation solutions seem mandatory to ensure extended lifetime to this type of device. And to fully enjoy the opportunities offered by soluble materials like conjugated polymers, these solutions have to be mechanically flexible.

The ability of oxygen and moisture to cross an encapsulating membrane is quantified by the oxygen transmission rate (OTR) and the water vapor transmission rate (WVTR). It is generally accepted that the lifetime of OLED devices above 10 000 h requires WVTR and OTR of about 10^{-6} g m^{-2} day^{-1} and 10^{-4} cm^3 m^{-2} day^{-1} atm^{-1}, respectively [241]. As illustrated in Fig. 11.53 these values are about 6–8 orders of magnitude lower than the corresponding values of commercially available polymer films. However, since conjugated polymer:fullerene-based solar cells are slightly less sensitive to oxidative agents, it is commonly considered that WVTR around 10^{-4} g m^{-2} day^{-1} might be sufficient for this type of devices. It has to be noted here that WVTR and OTR are inversely proportional to the thickness of a homogeneous membrane. This arises from the fact that these parameters are experimentally evaluated by placing the membrane in between a fully saturated and a fully depleted atmosphere (under constant flux of inert drain gas): The concentration of diffusing species within the cross section of the membrane follows a linear decrease. Thus, in order to decrease by 4 orders of magnitude the OTR of a 50-μm-thick PET substrate, one would have to increase its thickness by the same factor. Another solution consists of using inorganic gas barrier thin-film deposited on thin polymer substrate.

Transparent thin-film barrier coatings against permeation of gases and vapors deposited onto flexible polymer substrates have been intensively studied for ap-

<QA>17. 11.5.2 However, since conjugated polymer / I've assumed this should be fullerene; please check.

<QA>29. 11.5.2 It is generally accepted that / SI units are preferred (pascals rather than atmospheres).
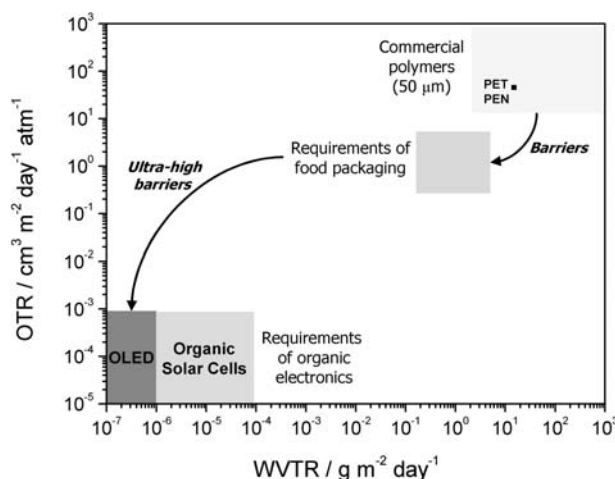
Fig. 11.53 Oxygen transmission rate (*OTR*) versus water vapor transmission rate (*WVTR*) of commercially available polymer films, food packaging requirements and organic electronics requirements.

plications in food and pharmaceutical packaging, where improving the barrier capabilities of the bare plastic films by 1–3 orders of magnitude is usually considered sufficient (Fig. 11.53). It has been shown that silicon-based dielectric coatings deposited by plasma-enhanced chemical vapor deposition (PECVD) on plastic films can be used as single-layer permeation barriers yielding barrier improvement factors (BIF) of up to 3 orders of magnitude [242, 243]. Permeation through those barrier materials has been proven to be a phenomenon controlled by nanometer-size structural defects present in the barrier coating, mainly caused by intrinsic or extrinsic surface roughness [242, 244, 245]. Moreover, theoretical calculations have shown that the total permeation rate through many small pinholes is much higher than that corresponding to the same total pinhole area combined in a few larger defects [246, 247]. This can be explained by lateral diffusion which is of crucial importance when the diameters of the defects are small compared with the thickness of the substrate. Thus, BIF beyond 3 orders of magnitude cannot be achieved with single inorganic layers.

The most common technique used to achieve ultrahigh barrier properties is based on alternating organic–inorganic multilayers: sandwiching inorganic barriers between polymeric buffers has been reported to reduce the number of pinholes significantly [248]. This can be explained in terms of smoothing of the coated surface, reduction of mechanical strains and increased thermal stability [241]. Moreover, repeating the alternating process yields stacked structures that allow the organic layers to epitaxially "decouple" the defects from neighboring inorganic layers. Polyacrylate/Al_2O_3 alternating coatings produced in a multistep process [249] have been used to encapsulate OLEDs. The organic layer is typically produced by flash evaporation of an acrylic monomer that is subsequently
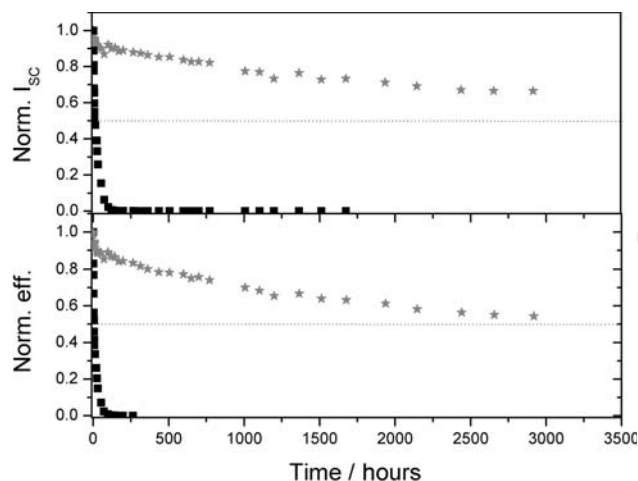
Fig. 11.54 Normalized I_{SC} and efficiency (*eff.*) of solar cells encapsulated with uncoated PET (squares) and with flexible ultrahigh gas barrier material (stars) versus storage time in the dark under ambient air. (Reproduced with permission from [252]).

cured by UV light while the inorganic coating is usually deposited by reactive sputtering. WVTR of about 2×10^{-6} g m^{-2} day^{-1} has been reported [250], yielding a 5-mm^2 OLED lifetime of 2500 h [251].

In the case of conjugated polymer:fullerene solar cells, the usage of another type of ultrahigh barrier was reported. This one, entirely produced by PECVD of alternative organic/SiO$_x$ on 175-μm-thick PET substrate, succeeded in the accelerated "calcium test" (50 °C, 85% relative humidity) for more than 1000 h, which corresponds to at least 10 000 h under normal ambient conditions [252]. Dennler et al. showed that MDMO-PPV:PCBM cells realized on and encapsulated with such substrates exhibit shelf-lifetime about 3000 h (Fig. 11.54) in

<QA>17. 11.5.2 However, since conjugated polymer / I've assumed this should be fullerene; please check.
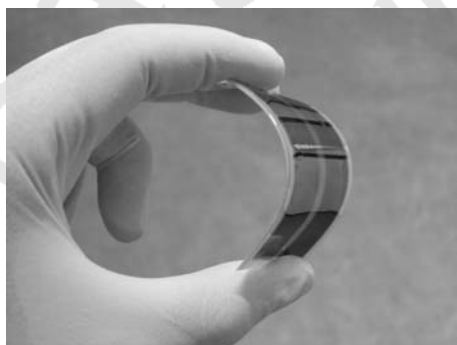
Fig. 11.55 Picture of a large scale ITO/PEDOT/MDMO-PPV:PCBM/Al device encapsulated with flexible, transparent, ultrahigh gas barrier [252].

spite of their appreciable mechanical flexibility (Fig. 11.55). These results are comparable to those reported by Neugebauer et al. (Fig. 11.52) obtained in the case of a cell encapsulated between glass plate. This observation reveals that the encapsulation may not be the limiting factor, and that the combined usage of more stable conjugated polymers with ultrahigh barrier could lead to very long lifetimes [235].

11.5.3
Routes for Improvements

11.5.3.1 **Hybrid Solar Cells**

In order to overcome certain drawbacks of organic semiconductors, the idea of the so-called hybrid solar cells using simultaneously organic and inorganic materials has been proposed [253]. As mentioned above, common conjugated polymers suffer from too-low charge-carrier mobility and too-narrow absorption spectrum. By replacing the acceptor with an inorganic semiconductor, more efficient charge collection can be expected. Moreover, the synthesis of semiconducting quantum dots, exhibiting strongly size-dependent optical properties [254], opened the route to optical band-gap tuning and potentially sensitization of conjugated polymers by mixing them with such nanoparticles.

In 1996, Greenham et al. reported a charge transfer between photoexcited MEH-PPV and quantum dots made of CdS and CdSe [253]. Upon mixing the conjugated polymer with these 5 nm nanoparticles, significant PL quenching and increases in PC were recorded, without evidence of any ground-state charge transfer [253, 255]. The PV devices made of these blends gave the best results for 90% (in weight) of nanoparticles, achieving V_{OC} about 0.5 V and an overall efficiency about 0.2% under AM 1.5.

Further improvements were triggered by the chemical synthesis of exotic newly shaped nanocrystals like CdSe nanorods, nanoarrows, and tetrapods (Fig. 11.56) [256, 257]. Huynh et al. studied blend of P3HT with nanorods of various aspect ratios [258]. They showed that by controlling the nanorod length, the distance over which electrons are transported through the film can be tuned (Fig. 11.57). Moreover, by using different rod radii, the authors were able to extend the absorption spectrum of the blend towards the red (Fig. 11.57). PV devices based on 90% in weight 7×60 nm nanorods mixed with P3HT were reported to exhibit a V_{OC} of 0.7 V and an efficiency of 1.7% under AM 1.5. A better charge collection could be ensured by replacing the rods with tetrapods [257, 259]. This enhancement was explained in terms of improvement of the electron transport perpendicular to the plane of the device, since unlike rods, tetrapods are unable to lie flat within the plane of the device [260]. Thus, by mixing CdSe tetrapods with MDMO-PPV, efficiencies up to 2.8% have been reported, with V_{OC} about 0.76 V and *FF* about 0.44 [261].

Other semiconductor nanoparticles have been investigated, yet showing lower efficiencies than in the case of CdSe. Arici et al. employed $CuInS_2$ mixed with
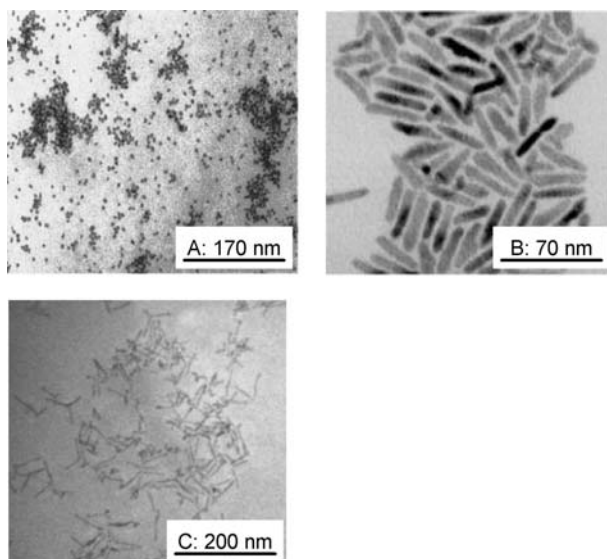
Fig. 11.56 CdSe nanodots (a), nanorods (b) and tetrapods (c) used in hybrid solar cells (adapted with permission from [258, 253]).

either P3HT [262] or PEDOT:PSS [263] and measured IPCE extended up to 900 nm [263]. Gunes et al. further enlarged the sensivich of hybrid solar cell up to 1500 nm by mixing P3HT with HgTe nanoparticles [264].

Finally, inspired by the principle of the dye-sensitized solar cell (Grätzel cells) [2], several works focused on the use of metal oxides. In order to overcome the difficulties of filling pores of mesoporous TiO_2 with conjugated polymer [265], TiO_2 nanoparticles blended with conjugated polymer [266] as well as chemically synthesized MDMO-PPV:TiO_2 bulk-heterojunctions [267] have been employed.
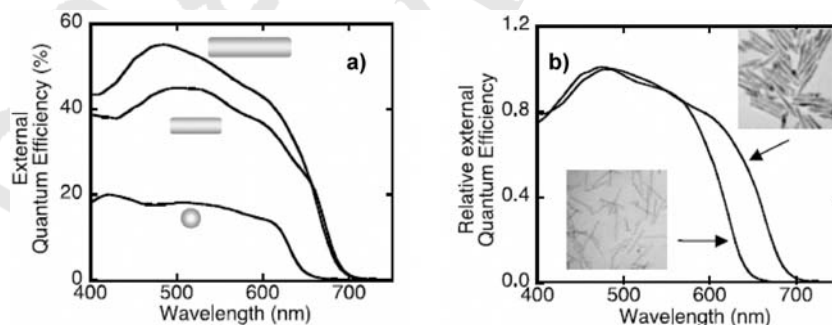
Fig. 11.57 (a) IPCE of devices based on P3HT blended with 7-nm-diameter CdSe nanorods with lengths 7, 30, and 60 nm. (b) Photocurrent spectra for two devices based on P3HT blended with 60-nm-long nanorods with diameters 7 and 3 nm. (Reproduced with permission from [258]).

Compared to TiO$_2$, ZnO used either as nanoparticles [268] or directly mixed with MDMO-PPV via a precursor route [269] has been shown to give much better results. Indeed, Beek et al. reported that MDMO-PPV:ZnO blends chemically synthesized can reach 1.1% efficiency, which is about 5 times better than in the case of TiO$_2$.

11.5.3.2 Metal Nanoparticles

The use of another type of nanoparticle did show promising enhancements of organic solar cells, yet these cells were not based on conjugated polymers but on small molecules. Stenzel et al. used Cu nanoparticles of about 3 nm on the top of the ITO electrode [270]. Up to a threefold increase in the conversion efficiency was reported. The authors explain this effect in terms of resonant surface plasmon frequency: In a semiconductor-based device structure, electromagnetic radiation incident on the semiconductor gives rise to an optical transition rate that is proportional to the duration of the interaction between the photon and the semiconductor, that is, to the transit time of the photon per unit thickness of the semiconductor. In comparison, for an electromagnetic field in a semiconductor arising from a surface-plasmon excitation in a proximate metal nanoparticle, the duration of the interaction between the field and the semiconductor will be determined by the lifetime of the surface plasmon excitation. Experimental observations of the lifetime and dephasing of nanoparticle surface-plasmon resonances have typically yielded values of 5–10 fs [271] which compares favorably with the photon transit time (1 fs) across the semiconductor region within which the surface plasmon field would be present (100 nm). Furthermore, the peak amplitude of the surface-plasmon-induced electromagnetic field is expected to be much greater than that of the incident electromagnetic field. Thus, the increased field amplitude and increased interaction time between the field and the semiconductor are believed to increase the absorption of incident electromagnetic energy near the nanoparticles [272]. Interestingly, the very same effect has been reported in the case of Au nanoparticles deposited on the top surface of Si *p–n* junctions: An increase of the photocurrent up to 50% was measured, and a direct impact of the nanoparticle size on the IPCE of the cells has been demonstrated [273]. However, it should be noted that another interpretation of the phenomenon has been proposed by Westphalen et al., who suggested a plasmon-enhanced excitation of electrons in the metal particle that can then be transferred to the surrounding dielectric material [274].

11.5.3.3 Carbon Nanotubes

We would like to mention here several works that have aimed to use carbon nanotubes (CNTs) as electron acceptor. This approach has been triggered by the tremendous geometric, electrical, and mechanical characteristics of CNTs [275]. The first conjugated polymer:CNT solar cells were performed by Ago et al., using a bilayer of PPV with multiwalled carbon nanotubes (MWNTs) [276]. A

significant increase in the IPCE was observed compared to pure PPV. The authors further reported quenching of PL and of the triplet state of the PPV, when blended with MWNTs. Their photophysical investigations concluded on a nonradiative energy transfer from the PPV to the MWNT as the predominant electronic interaction [277]. On the other hand, Kymakis et al. studied blends of single wall carbon nanotubes (SWNTs) and P3HT [278]. They measured a V_{OC} close to 0.75 V, a I_{SC} about 0.2 mA cm^{-2} and a *FF* of 0.4 inducing an overall efficiency of about 0.06% under AM 1.5 [279].

Finally, one should mention that the potentially high conductivity and high transparence of CNTs [280] have been shown to allow their use as conductive electrodes in the case of P3HT:PCBM solar cells fabricated on glass substrate [281].

11.6
Conclusions

After few years of research and development, OPVs has made impressive progresses. While the very first devices based on sublimated merocyanines and phthalocyanines developed in the late 1980s showed efficiency of 1%, recent reports have announced record efficiencies of 5%. This rapid progress is predominantly based on achievements in the material science. Novel generations of conjugated polymers reaching purities comparable to some inorganic semiconductors can no longer be compared to the first organic semiconductors, such as polyacetylene. Beyond the enhancement of the semiconducting and optical properties of the photoactive materials, however, other important developments have to be carried out, like gaining improved control over the solid-state morphology of donor–acceptor composites. The near future will show exciting developments, some of which are already anticipated, like self-assembled materials, nanosized device geometries to release the requirements on the proper morphology, metallic nanoparticles and plasmon absorption and highly complex molecules which fulfill all functions in distinct parts of the molecule. Simultaneously, further developments of the solution-based techniques such as inkjet, screen, or flexographic printing (a form of rotary web letterpress using flexible relief plates) for the production of organic thin-film solar cells will occur. Moreover important economic factors addressing the balance-of-system costs will have to be addressed, like novel semiconducting electrodes to replace ITO, low-cost barriers against water and oxygen permeation as well as flexible electronic components to be combined with flexible PV power supply.

Thus, it is much likely that efficiencies close to 10% will be achieved in the relatively short term. The future of alternative renewable PVs appears bright.

References

1 A. Jäger-Waldau, *PV Status Report 2003*. Office for Official Publications of the European Communities, **2003**.

2 B. O'Regan, M. Grätzel, *Nature* **1991**, *353*, 737.

3 B.A. Gregg, M.C. Hanna, *J. Appl. Phys.* **2003**, *93*, 3605.

4 N.S. Sariciftci (ed.) *Primary Photoexcitation in Conjugated Polymers: Molecular Exciton Versus Semiconductor Band Model*. World Scientific, Singapore, **1997**.

5 B.A. Gregg, *J. Phys. Chem. B* **2003**, *107*, 4688.

6 L. Onsager, *Phys. Rev.* **1938**, *54*, 554.

7 B. Schweitzer, H. Bässler, *Synth. Met.* **2000**, *109*, 1.

8 A. Haugeneder, M. Neges, C. Kallinger, W. Spirkl, U. Lemmer, J. Feldmann, U. Scherf, E. Harth, A. Gügel, K. Müllen, *Phys. Rev. B* **1999**, *59*, 15346.

9 D. Vacar, E.S. Maniloff, D.W. McBranch, A.J. Heeger, *Phys. Rev. B* **1997**, *56*, 4573.

10 E.S. Maniloff, V. Klimov, D. McBranch, *Phys. Rev. B* **1997**, *56*, 1876.

11 M. Theander, A. Yartsev, D. Zigmantas, V. Sundström, W. Mammo, M.R. Andersson, O. Inganäs, *Phys. Rev. B* **2000**, *61*, 12957.

12 T. Stübinger, W. Brütting, *J. Appl. Phys.* **2001**, *90*, 3632.

13 Z.D. Popovic, A.-M. Hor, R.O. Loutfy, *Chem. Phys.* **1988**, *127*, 451.

14 V.I. Arkhipov, E.V. Emelianova, H. Bässler, *Phys. Rev. Lett.* **1999**, *82*, 1321.

15 D.M. Basko, E.M. Conwell, *Synth. Met.* **2003**, *139*, 819.

16 N.S. Sariciftci, A.J. Heeger, in H.S. Nalwa (ed.) *Handbook of Organic Conductive Molecules and Polymers, Vol. 1.* Wiley, New York, **1997** ● AQ13.

17 Y. Wang, *Nature* **1992**, *356*, 585.

18 N.S. Sariciftci, L. Smilowitz, A.J. Heeger, F. Wudl, *Science* **1992**, *258*, 1474.

19 S. Morita, A.A. Zakhidov, K. Yoshino, *Solid State Commun.* **1992**, *82*, 249.

20 N.S. Sariciftci, L. Smilowitz, A.J. Heeger, F. Wudl, *Synth. Met.* **1993**, *59*, 333.

21 K. Yoshino, X.H. Yin, S. Morita, T. Kawai, A.A. Zakhidov, *Solid State Commun.* **1993**, *85*, 85.

22 S. Morita, A.A. Zakhidov, K. Yoshino, *Jpn. J. Appl. Phys.* **1993**, *32*, L873.

23 N.S. Sariciftci, A.J. Heeger, *Int. J. Mod. Phys. B* **1994**, *8*, 237.

24 K. Yoshino, T. Akashi, K. Yoshimoto, S. Morita, R. Sugimoto, A.A. Zakhidov, *Solid State Commun.* **1994**, *90*, 41.

25 N.S. Sariciftci, *Prog. Quantum Electron.* **1995**, *19*, 131.

26 N.S. Sariciftci, A.J. Heeger, *Synth. Met.* **1995**, *70*, 1359.

27 G. Zerza, C.J. Brabec, G. Cerullo, S. De Silvestri, N.S. Sariciftci, *Synth. Met.* **2001**, *119*, 637.

28 C.H. Lee, G. Yu, N.S. Sariciftci, D. Moses, K. Pakbaz, C. Zhang, A.J. Heeger, F. Wudl, *Phys. Rev. B* **1993**, *48*, 15425.

29 X. Wei, Z.V. Vardeny, N.S. Sariciftci, A.J. Heeger, *Phys. Rev. B* **1996**, *53*, 2187.

30 L. Smilowitz, A.J. Heeger, *Synth. Met.* **1992**, *48*, 193.

31 M.J. Rice, Y.N. Gartenstein, *Phys. Rev. B* **1997**, *53*, 10764.

<QA>13. References 16, 39, 40, 42, 60 / Please provide page numbers.

32 A. J. Heeger, S. Kievelson, J. R. Schrieffer, W. P. Su, *Rev. Mod. Phys.* **1988**, *60*, 781.

33 J. Bruening, B. Friedman, *J. Chem. Phys.* **1997**, *106*, 9634.

34 B. Kraabel, D. McBranch, N. S. Sariciftci, D. Moses, A. J. Heeger, *Phys. Rev. B* **1994**, *50*, 18.

35 C. J. Brabec, G. Zerza, G. Cerullo, S. De Silvestri, S. Luzzati, J. C. Hummelen, N. S. Sariciftci, *Chem. Phys. Lett.* **2001**, *340*, 232.

36 G. Cerullo, M. Nisoli, S. Stagiro, S. De Silvestri, *Opt. Lett.* **2000**, *316*, 356.

37 K. Lee, E. K. Miller, N. S. Sariciftci, J. C. Hummelen, F. Wudl, A. J. Heeger, *Phys. Rev. B* **1996**, *54*, 10525.

38 H. Johannson, C. J. Brabec, H. Neugebauer, J. C. Hummelen, R. A. J. Janssen, N. S. Sariciftci, *Synth. Met.* **1999**, *101*, 192.

39 G. Zerbi, M. Gussoni, C. Castiglioni, in J. L. Brédas, R. Silbey (eds.) *Conjugated Polymers*. Kluwer, **1991**.

40 G. Zerbi, C. Castiglioni, M. Del Zoppo, in K. Müllen, G. Wegner (eds.) *Electronic Materials: The Oligomer Approach*. Wiley-VCH, Weinheim, **1998**.

41 Z. Vardeny, E. Ehrenfreund, O. Brafman, A. J. Heeger, F. Wudl, *Synth. Met.* **1987**, *18*, 183.

42 H. Neugebauer, A. Neckel, N. Brinda-Konopik, in H. Kuzmany, M. Mehring, S. Roth (eds.) *Electronic Properties of Polymers and Related Compounds*, Springer Series in Solid State Sciences. Springer, Berlin, **1985**.

43 E. Ehrenfreund, Z. V. Vardeny, *J. Int. Opt. Eng.* **1997**, *3145*, 324.

44 A. Girlando, A. Painelli, Z. G. Soos, *J. Chem. Phys.* **1993**, *98*, 7459.

45 K. H. Lee, R. A. J. Janssen, N. S. Sariciftci, A. J. Heeger, *Phys. Rev. B* **1994**, *49*, 5781.

46 V. Dyakonov, G. Zoriniants, M. C. Scharber, C. J. Brabec, R. A. J. Janssen, J. C. Hummelen, N. S. Sariciftci, *Phys. Rev. B* **1999**, *59*, 8019.

47 P. M. Allemand, G. Srdanov, A. Koch, K. Khemani, F. Wudl, Y. Rubin, F. N. Diederich, M. M. Alvarez, S. J. Anz, R. L. Whetten, *J. Am. Chem. Soc.* **1991**, *113*, 2780.

48 I. D. Parker, *J. Appl. Phys.* **1994**, *75*, 1656.

49 W. R. Salaneck, S. Strafström, J. L. Brédas (eds.) *Conjugated Polymer Surfaces and Interfaces: Electronic and Chemical Structure of Interfaces for Polymer Light Emitting Devices*. Cambridge University Press, Cambridge, **1996**.

50 I. G. Hill, A. Rajagopal, A. Kahn, Y. Hu, *Appl. Phys. Lett.* **1998**, *73*, 662.

51 H. Ishii, K. Sugiyama, E. Ito, K. Seki, *Adv. Mater.* **1999**, *11*, 605.

52 R. I. Frank, J. G. Simmons, *J. Appl. Phys.* **1967**, *38*, 832.

53 S. Nespurek, J. Sworakowski, *Radiat. Phys. Chem.* **1990**, *36*, 3.

54 V. I. Arkhipov, E. V. Emelianova, Y. H. Tak, H. Bässler, *J. Appl. Phys.* **1998**, *84*, 848.

55 T. van Woudenbergh, P. W. M. Blom, M. C. J. M. Vissenberg, J. N. Huiberts, *Appl. Phys. Lett.* **2001**, *79*, 1697.

56 H. Bässler, *Phys. Status Solidi B* **1993**, *175*, 15.

57 P. Würfel, *Physica E* **2002**, *14*, 18.

58 J. Rostalski, D. Meissner, *Sol. Energy Mater. Sol. Cells* **2000**, *61*, 87.

<QA>11. References 36 / Please provide an initial for Cerullo.

<QA>12. References 39 / Please provide the publisher's location.

<QA>13. References 16, 39, 40, 42, 60 / Please provide page numbers.

59 ASTM G-173-03, ISO 9845-1:1992.

60 J. Kanicki, in T. A. Skotheim (ed.) *Handbook of Conducting Polymers, Vol. 1.* Dekker, New York, **1985**.

61 G. Horovitz, *Adv. Mater.* **1989**, *2*, 287.

62 S. Glenis, G. Tourillon, F. Garnier, *Thin Solid Films* **1986**, *139*, 221.

63 R. N. Marks, J. J. M. Halls, D. D. Bradley, R. H. Friends, A. B. Holmes, *J. Phys. Condensed Matter* **1994**, *6*, 1379.

64 J. H. Burroughes, D. D. C. Bradley, A. R. Brown, R. N. Marks, K. Mackay, R. H. Friend, P. L. Burn, A. B. Holmes, *Nature* **1990**, *347*, 539.

65 D. Braun, A. J. Heeger, *Appl. Phys. Lett.* **1991**, *58*, 1982.

66 G. Yu, C. Zhang, A. J. Heeger, *Appl. Phys. Lett.* **1994**, *64*, 1540.

67 G. Yu, K. Pakbaz, A. J. Heeger, *Appl. Phys. Lett.* **1994**, *64*, 3422.

68 G. Gustafsson, M. Sundberg, O. Inganäs, C. Svensson, *J. Mol. Electron.* **1990**, *6*, 105.

69 H. Antoniadis, B. R. Hsieh, M. A. Abkowitz, M. Stolka, S. A. Jenekhe, *Polym. Preprints* **1993**, *34*, 490.

70 H. Antoniadis, B. R. Hsieh, M. A. Abkowitz, S. A. Jenehke, M. Stolka, *Synth. Met.* **1994**, *62*, 265.

71 S. Karg, W. Riess, V. Dyakonov, M. Schwörer, *Synth. Met.* **1993**, *54*, 427.

72 S. Karg, W. Riess, M. Meier, M. Schwörer, *Mol. Cryst. Liq. Cryst.* **1993**, *79*, 236.

73 W. Riess, S. Karg, V. Dyakonov, M. Meier, M. Schwörer, *J. Lumin.* **1994**, *60/61*, 906.

74 D. Wöhrle, D. Meissner, *Adv. Mater.* **1991**, *3*, 129.

75 G. A. Chamberlain, *Sol. Cells* **1983**, *8*, 47.

76 H. Spanggaard, F. C. Krebs, *Sol. Energy Mater. Sol. Cells* **2004**, *83*, 125.

77 C. W. Tang, *US Patent 4164431, August 14, 1979.*

78 C. W. Tang, *Appl. Phys. Lett.* **1986**, *48*, 183.

79 N. S. Sariciftci, D. Baun, C. Zhang, V. I. Srdanov, A. J. Heeger, G. Stucky, F. Wudl, *Appl. Phys. Lett.* **1993**, *62*, 585.

80 J. J. M. Halls, K. Pichler, R. H. Friend, S. C. Moratti, A. B. Holmes, *Appl. Phys. Lett.* **1996**, *68*, 3120.

81 L. S. Roman, W. Mammo, L. A. A. Pettersson, M. R. Andersson, O. Inganäs, *Adv. Mater.* **1998**, *10*, 774.

82 J. J. M. Halls, R. H. Friend, *Synth. Met.* **1997**, *85*, 1307.

83 M. Hiramoto, M. Suezaki, M. Yokoyama, *Chem. Lett.* **1990**, *3*, 327.

84 P. Peumans, A. Yakimov, S. R. Forrest, *J. Appl. Phys.* **2003**, *93*, 3693.

85 C. Y. Yang, A. J. Heeger, *Synth. Met.* **1996**, *83*, 85.

86 J. C. Hummelen, B. W. Knight, F. LePeq, F. Wudl, J. Yao, C. L. Wilkins, *J. Org. Chem.* **1995**, *60*, 532.

87 G. Yu, J. Gao, J. C. Hummelen, F. Wudl, A. J. Heeger, *Science* **1995**, *270*, 1789.

88 S. Hotta, S. D. D. V. Rughooputh, A. J. Heeger, *Synth. Met.* **1987**, *22*, 79.

89 M. Sahimi, *Application of Percolation Theory.* Taylor & Francis, London, **1984**.

90 Y. Cao, G. Yu, C. Zhang, R. Menon, A. J. Heeger, *Synth. Met.* **1997**, *87*, 171.

<QA>14. References 59 / Please provide more detail for this reference

<QA>13. References 16, 39, 40, 42, 60 / Please provide page numbers.

91 S. Karg, J.C. Scott, J.R. Salem, M. Angelopoulos, *Synth. Met.* **1996**, *80*, 111.

92 C.J. Brabec, S.E. Shaheen, C. Winder, N.S. Sariciftci, P. Denk, *Appl. Phys. Lett.* **2002**, *80*, 1288.

93 L.S. Hung, C.W. Tang, M.G. Mason, *Appl. Phys. Lett.* **1997**, *70*, 152.

94 W.J.H. van Gennip, J.K.J. van Duren, P.C. Thüne, R.A.J. Janssen, J.W. Niemantsverdriet, *J. Chem. Phys.* **2002**, *117*, 5031.

95 T. Munsters, T. Martens, L. Goris, V. Vrindts, J. Manca, L. Lutsen, W. De Ceuminck, D. Vanderzande, L. De Shepper, J. Gelan, N.S. Sariciftci, C.J. Brabec, *Thin Solid Films* **2002**, *403/404*, 247.

96 A.J. Mozer, P. Denk, M. Scharber, H. Neugebauer, N.S. Sariciftci, P. Wagner, L. Lutsen, D. Vanderzande, *J. Phys. Chem. B* **2004**, *108*, 5235.

97 S.E. Shaheen, C.J. Brabec, N.S. Sariciftci, F. Padinger, T. Fromherz, J.C. Hummelen, *Appl. Phys. Lett.* **2001**, *78*, 841.

98 G. Yu, A.J. Heeger, *J. Appl. Phys.* **1995**, *78*, 4510.

99 J.J.M. Halls, C.A. Walsh, N.C. Greenham, E.A. Marseglia, R.H. Friend, S.C. Moratti, A.B. Holmes, *Nature* **1995**, *376*, 498.

100 M. Granström, K. Petritsch, A.C. Arias, A. Lux, M.R. Andersson, R.H. Friend, *Nature* **1998**, *395*, 257.

101 P. Würfel, *Physics of Solar Cells,* Wiley-VCH, Weinheim, **2004**.

102 U. Dutta, P. Chatterjee, *J. Appl. Phys.* **2004**, *96*, 2261.

103 Y.R. Shen, *The Principles of Nonlinear Optics.* Wiley, New York, **1984**.

104 I.H. Campbell, T.W. Hagler, D.L. Smith, J.P. Ferraris, *Phys. Rev. Lett.* **1996**, *76*, 1900.

105 T.M. Brown, J.S. Kim, R.H. Friend, F. Cacialli, R. Daik, W.J. Feast, *Appl. Phys. Lett.* **1999**, *75*, 1679.

106 T.M. Brown, R.H. Friend, I.S. Millard, D.L. Lacey, J.H. Burroughes, F. Cacialli, *Appl. Phys. Lett.* **2000**, *77*, 3096.

107 T.M. Brown, R.H. Friend, I.S. Millard, D.L. Lacey, T. Butler, J.H. Burroughes, F. Cacialli, *J. Appl. Phys.* **2003**, *93*, 6159.

108 J. Liu, Y. Shi, Y. Yang, *Adv. Funct. Mater.* **2001**, *11*, 420.

109 C.M. Ramsdale, J.A. Baker, A.C. Arias, J.D. MacKenzie, R.H. Friend, N.C. Greenham, *J. Appl. Phys.* **2002**, *92*, 4266.

110 C.J. Brabec, A. Cravino, D. Meissner, N.S. Sariciftci, M.T. Rispens, L. Sanchez, J.C. Hummelen, T. Fromherz, *Thin Solid Films* **2002**, *403/404*, 368.

111 H. Kim, S.-H. Jin, H. Suh, K. Lee, *Proc. SPIE* **2004**, *5215*, 111.

112 A. Gadisa, M. Svensson, M.R. Andersson, O. Inganäs, *Appl. Phys. Lett.* **2004**, *84*, 1609.

113 H. Frohne, S.E. Shaheen, C.J. Brabec, D. Müller, N.S. Sariciftci, K. Meerholz, *Chem. Phys. Chem.* **2002**, *9*, 795.

114 C.J. Brabec, A. Cravino, D. Meissner, N.S. Sariciftci, T. Fromherz, M.T. Rispens, L. Sanchez, J.C. Hummelen, *Adv. Funct. Mater.* **2001**, *11*, 374.

115 L.J. Brillson, *Surf. Sci. Rep.* **1982**, *2*, 123.

116 C.M. Heller, I.H. Campbell, D.L. Smith, N.N. Barashkov, J.P. Ferraris, *J. Appl. Phys.* **1997**, *81*, 3227.

117 V. D. Mihailetchi, P. W. M. Blom, J. C. Hummelen, M. T. Rispens, *J. Appl. Phys.* **2003**, *94*, 6849.

118 V. D. Mihailetchi, L. A. J. Koster, P. W. M. Blom, *Appl. Phys. Lett.* **2004**, *85*, 970.

119 J. K. J. van Duren, Y. Yang, J. Loos, C. W. T. Bulle-Lieuwma, A. B. Sieval, J. C. Hummelen, R. A. J. Janssen, *Adv. Funct. Mater.* **2004**, *14*, 425.

120 F. Padinger, R. S. Ritterberger, N. S. Sariciftci, *Adv. Funct. Mater.* **2003**, *13*, 85.

121 E. A. Katz, D. Faiman, S. M. Tuladhar, J. M. Kroon, M. M. Wienk, T. Fromherz, F. Padinger, C. J. Brabec, N. S. Sariciftci, *J. Appl. Phys.* **2001**, *90*, 5343.

122 L. J. A. Koster, V. D. Mihailetchi, R. Ramaker, P. W. M. Blom, *Appl. Phys. Lett.* **2005**, *86*, 123509.

123 H. A. M. van Mullekom, J. A. J. M. Vekemans, E. E. Havinga, E. W. Meijer, *Mater. Sci. Eng. Rep.* **2001**, *32*, 1.

124 L. B. Groenendaal, F. Jonas, D. Freitag, H. Pielartzik, J. R. Reynolds, *Adv. Mater.* **2000**, *12*, 481.

125 I. F. Perepichka, D. F. Perepichka, H. Meng, F. Wudl, *Adv. Mater.* **2005**, *17*, 2281.

126 P. Schilinsky, C. Waldauf, J. Hauch, C. J. Brabec, *J. Appl. Phys.* **2004**, *95*, 3816.

127 G. Li, V. Shrotriya, Y. Yang, *J. Appl. Phys.* **2005**, *98*, 043704.

128 W. Ma, C. Yang, X. Gong, K. Lee, A. J. Heeger, *Adv. Funct. Mater.* **2005**, *15*, 1617.

129 C. Winder, N. S. Sariciftci, *J. Mater. Chem.* **2004**, *14*, 1077.

130 J. Roncali, *Chem. Rev.* **1997**, *97*, 173.

131 M. Bergren, G. Gustafsson, O. Inganäs, M. R. Andersson, T. Hjertberg, O. Wennerström, *Appl. Phys. Lett.* **1994**, *65*, 1489.

132 M. R. Andersson, M. Berggren, O. Inganäs, G. Gustaffson, J. C. Gustafsson-Carlberg, D. Selse, T. Hjertberg, O. Wennerström, *Macromolecules* **1995**, *28*, 7525.

133 M. R. Andersson, O. Thomas, W. Manno, M. Svensson, M. Theander, O. Inganäs, *J. Mater. Chem.* **1999**, *9*, 1933.

134 A. Dkhissi, F. Louwet, L. Groenendaal, B. Beljonne, R. Lazzaroni, J. L. Brédas, *Chem. Phys. Lett.* **2002**, *359*, 472.

135 A. Dhanabalan, J. K. J. van Duren, P. A. van Hal, J. L. J. Van Dongen, R. A. J. Janssen, *Adv. Funct. Mater.* **2001**, *11*, 255.

136 F. Zhang, E. Perzon, X. Wang, W. Mammo, M. R. Andersson, O. Inganäs, *Adv. Funct. Mater.* **2005**, *15*, 745.

137 X. Wang, E. Perzon, F. Oswald, F. Langa, S. Admassie, M. R. Andersson, O. Inganäs, *Adv. Funct. Mater.* **2005**, *15*, 1665.

138 X. Wang, E. Perzon, J. L. Delgado, P. de la Cruz, F. Zhang, F. Langa, M. R. Andersson, O. Inganäs, *Appl. Phys. Lett.* **2005**, *85*, 5081.

139 T. Fromherz, F. Padinger, D. Gebeyehu, C. J. Brabec, J. C. Hummelen, N. S. Sariciftci, *Sol. Energy Mater. Sol. Cells* **2000**, *63*, 61.

140 M.M. Wienk, J.M. Kroon, W.J.H. Verhees, J. Krol, J.C. Hummelen, P.A. van Hal, R.A.J. Janssen, *Angew. Chem.* **2003**, *115*, 3493.

141 J.W. Arbogast, C.S. Foote, *J. Am. Chem. Soc.* **1991**, *113*, 8886.

142 P. Peumanns, V. Bulovic, S.R. Forrest, *Appl. Phys. Lett.* **2000**, *76*, 2650.

143 L.S. Roman, O. Inganäs. T. Granlund, T. Ryberg, M. Svensson, M.R. Andersson, J.C. Hummelen, *Adv. Funct. Mater.* **2000**, *12*, 189.

144 M. Niggemann, M. Glatthaar, A. Gomvert, A. Hinsch, V. Wittwer, *Thin Solid Films* **2004**, *451/452*, 619.

145 H. Hoppe, N.S. Sariciftci, D. Meissner, *Mol. Cryst. Liq. Cryst.* **2002**, *385*, 113.

146 L.A.A. Petterson, L.S. Roman, O. Inganäs, *J. Appl. Phys.* **1999**, *86*, 487.

147 H. Hoppe, N. Arnold, D. Meissner, N.S. Sariciftci, *Sol. Energy Mater. Sol. Cells* **2003**, *80*, 105.

148 J.-F. Eckert, J.-F. Nicoud, J.-F. Nierengarten, S.-G. Liu, G. Hadziioannou, *J. Am. Chem. Soc.* **2000**, *122*, 7467.

149 M.A. Loi, P. Denk, H. Hoppe, H. Neugebauer, C. Winder, D. Meissner, C.J. Brabec, N.S. Sariciftci, A. Gouloumis, P. Vasquez, T. Torres, *J. Mater. Chem.* **2003**, *13*, 700.

150 F. Zhang, M. Svensson, M.R. Andersson, M. Maggini, S. Bucella, E. Menna, O. Inganäs, *Adv. Funct. Mater.* **2001**, *13*, 1871.

151 A. Cravino, N.S. Sariciftci, *Nature Mater.* **2003**, *2*, 360.

152 H. Hoppe, M. Niggemann, C. Winder, J. Kraut, R. Hiesgen, A. Hinsch, D. Meissner, N.S. Sariciftci, *Adv. Funct. Mater.* **2004**, *14*, 1005.

153 T. Martens, J. D'Haen, T. Munsters, Z. Beelen, L. Goris, J. Manca, M. D'Olieslaeger, D. Vanderzande, L. De Schepper, R. Andriessen, *Synth. Met.* **2003**, *138*, 243.

154 X. Yang, J.K. van Duren, R.A.J. Janssen, M.A.J. Michels, J. Loos, *Macromolecules* **2004**, *37*, 2151.

155 C.W.T. Bulle-Lieuwma, W.J.H. Van Gennip, J.K.J. van Duren, P. Jonkheijm, R.A.J. Janssen, J.W. Niemantsverdriet, *Appl. Surf. Sci.* **2003**, *203/204*, 547.

156 X. Yang, J.K.J. van Duren, M.T. Rispens, J.C. Hummelen, R.A.J. Janssen, M.A.J. Michels, J. Loos, *Adv. Mater.* **2004**, *16*, 802.

157 Y. Kim, S.A. Choulis, J. Nelson, D.D.C. Bradley, S. Cook, J.R. Durrant, *Appl. Phys. Lett.* **2005**, *86*, 063502.

158 M. Al-Ibrahim, O. Ambacher, S. Sensfuss, G. Gobsch, *Appl. Phys. Lett.* **2005**, *86*, 201120.

159 J. Huang, G. Li, Y. Yang, *Appl. Phys. Lett.* **2005**, *87*, 112105.

160 X. Yang, J. Loos, S.C. Veenstra, W.J.H. Verhees, M.M. Wienk, J.M. Kroon, M.A.J. Michels, R.A.J. Janssen, *Nano Lett.* **2005**, *5*, 579.

161 J. Birgerson, M. Fahlman, P. Broms, W.R. Salaneck, *Synth. Met.* **1996**, *80*, 125.

162 R.A. Marcus, *Rev. Mod. Phys.* **1993**, *65*, 599.

163 A. Miller, E. Abrahams, *Phys. Rev.* **1960**, *120*, 745.

164 D.M. Pai, *J. Chem. Phys.* **1970**, *52*, 2285.

165 J. Frenkel, *Phys. Rev.* **1938**, *54*, 647.

166 W. D. Gill, *J. Appl. Phys.* **1972**, *43*, 5033.

167 L. Bozano, S. A. Carter, J. C. Scott, G. G. Mallarias, P. J. Brock, *Appl. Phys. Lett.* **1999**, *74*, 1132.

168 P. W. M. Blom, M. J. M. de Jong, M. G. van Muster, *Phys. Rev. B* **1997**, *55*, 656.

169 A. J. Mozer, G. Dennler, N. S. Sarificti, M. Westerling, A. Pivrikas, R. Österbacka, G. Juska, *Phys. Rev. B* **2005**, *72*, 035217.

170 S. V. Rakhmanova, E. M. Conwell, *Synth. Met.* **2001**, *116*, 389.

171 A. J. Mozer, N. S. Sariciftci, A. Pivrikas, R. Österbacka, G. Juska, L. Brassat, H. Bässler, *Phys. Rev. B* **2005**, *72*, 035214.

172 V. D. Mihailetchi, J. K. J. van Duren, P. W. M. Blom, J. C. Hummelen, R. J. Janssen, J. M. Kroon, M. T. Rispens, W. J. H. Verhees, M. M. Wienk, *Adv. Funct. Mater.* **2003**, *13*, 43.

173 P. W. M. Blom, M. J. M. de Jong, S. Breedijk, *App. Phys. Lett.* **1997**, *71*, 930.

174 C. Melzer, E. J. Koop, V. D. Mihailetchi, P. W. M. Blom, *Adv. Funct. Mater.* **2004**, *14*, 865.

175 A. J. Mozer, N. S. Sariciftci, L. Lutsen, D. Vanderzande, R. Österbacka, M. Westerling, G. Juska, *Appl. Phys. Lett.* **2005**, *86*, 112104.

176 R. Pacios, D. D. C. Bradley, J. Nelson, C. J. Brabec, *Synth. Met.* **2003**, *137*, 1469.

177 R. Pacios, J. Nelson, D. D. C. Bradley, C. J. Brabec, *Appl. Phys. Lett.* **2003**, *83*, 4764.

178 E. von Hauff, J. Parisi, V. Dyakonov, *Thin Solid Film*, in press.

179 J.-I. Nakamura, K. Murata, K. Takahashi, *Appl. Phys. Lett.* **2005**, *87*, 132105.

180 C. Tanase, E. J. Meier, P. W. M. Blom, D. M. de Leeuw, *Phys. Rev. Lett.* **2003**, *91*, 216601.

181 P. W. M. Blom, M. J. M. de Jong, J. J. M. Vleggaar, *Appl. Phys. Lett.* **1996**, *68*, 3308.

182 V. I. Arkhipov, P. Heremans, E. V. Emelianova, G. J. Adriaenssens, H. Bässler, *Appl. Phys. Lett.* **2003**, *82*, 3245.

183 I. Riedel, J. Parisi, V. Dyakonov, L. Lutsen, D. Vanderzande, J. C. Hummelen, *Adv. Funct. Mater.* **2004**, *14*, 38.

184 I. Riedel, V. Dyakonov, *Phys. Status Solidi A* **2004**, *201*, 1332.

185 H. H. P. Gommans, M. Kemerink, J. M. Kramer, R. A. J. Janssen, *Appl. Phys. Lett.* **2005**, *87*, 122104.

186 N. A. Schultz, M. C. Scharber, C. J. Brabec, N. S. Sariciftci, *Phys. Rev. B* **2001**, *64*, 245210.

187 B. I. Shklovskii, H. Fritzsche, S. D. Baranovskii, *Phys. Rev. Lett.* **1989**, *62*, 2989.

188 I. Montanari, A. F. Nohueira, J. Nelson, J. Durrant, C. Winder, M. A. Loi, N. S. Sariciftci, C. J. Brabec, *Appl. Phys. Lett.* **2002**, *81*, 3001.

189 A. F. Nogueira, I. Montanari, J. Nelson, J. R. Durrant, C. Winder, N. S. Sariciftci, C. J. Brabec, *J. Phys. Chem. B* **2003**, *107*, 1567.

190 J. Nelson, *Phys. Rev. B* **2003**, *67*, 155209.

<QA>15. References 178, 199, 252, 264 / Please update these references, if possible.

191 S. C. J. Meskers, P. A. van Hal, A. J. H. Spiering, J. C. Hummelen, R. A. J. Janssen, *Phys. Rev. B* **2000**, *61*, 9917.

192 J. E. Kroeze, T. J. Savenije, M. J. W. Vermeulen, J. M. Warman, *J. Phys. Chem. B* **2003**, *107*, 7696.

193 T. J. Savenije, J. E. Kreoze, M. M. Wienk, J. M. Kroon, J. M. Warman, *Phys. Rev. B* **2004**, *69*, 155205.

194 P. A. C. Quist, T. J. Savenije, M. K. Koetse, S. C. Veenstra, J. M. Kroon, L. D. A. Siebbeles, *Adv. Funct. Mater.* **2005**, *15*, 469.

195 G. Juška, K. Arlauskas, M. Viliūnas, J. Kočka, *Phys. Rev. Lett.* **2000**, *84*, 4946.

196 G. Juska, K. Arlauskas, M. Viliūnas, K. Genevicius, R. Österbacka, H. Stubb, *Phys. Rev. B* **2000**, *62*, 16235.

197 M. V. Smoluchovsky, *Z. Phys. Chem. Stoechiom. Verwandtschaftsl.* **1917**, *92*, 129.

198 P. Langevin, *Ann. Chem. Phys.* **1903**, *28*, 289.

199 G. Dennler, N. S. Sariciftci, A. J. Mozer, A. Pivrikas, R. Österbacka, G. Juska, in press.

200 M. Pope, C. E. Swenberg, *Electronic Processes in Organic Crystals and Polymers*, 2nd edn. Oxford University Press, New York, **1999**.

201 R. Österbacka, A. Pivrikas, G. Juska, K. Genevicius, K. Arlauskas, H. Stubb, *Curr. Appl. Phys.* **2004**, *4*, 534.

202 A. Pivrikas, G. Juška, R. Österbacka, M. Westerling, M. Villiūnas, K. Arlauskas, H. Stubb, *Phys. Rev. B* **2005**, *71*, 125205.

203 A. Pivrikas, G. Juska, A. J. Mozer, M. Scharber, K. Arlauskas, N. S. Sariciftci, H. Stubb, R. Österbacka, *Phys. Rev. Lett.* **2005**, *94*, 176806.

204 V. D. Mihailetchi, L. J. A. Koster, P. W. M. Blom, C. Melzer, B. de Boer, J. K. J. van Duren, R. A. J. Janssen, *Adv. Funct. Mater.* **2005**, *15*, 795.

205 J. O. Härter, S. V. Chasteen, S. A. Carter, *Appl. Phys. Lett.* **2005**, *86*, 164101.

206 S. M. Sze, *Semiconductor Devices.* Wiley, New York, **1985**.

207 V. Dyakonov, *Appl. Phys. A* **2004**, *21–25*, 21.

208 T. Aernouts, W. Geens, J. Poortmans, P. Heremans, S. Borghs, R. Mertens, *Thin Solid Films* **2002**, *403/404*, 297.

209 C. Waldauf, P. Schilinsky, J. Hauch, C. J. Brabec, *Thin Solid Films* **2004**, *451/452*, 503.

210 L. J. A. Koster, E. C. P. Smits, V. D. Mihailetchi, P. W. M. Blom, *Phys. Rev. B* **2005**, *72*, 085205.

211 V. D. Mihailetchi, L. J. A. Koster, J. C. Hummelen, P. W. M. Blom, *Phys. Rev. Lett.* **2005**, *93*, 216601.

212 N. Tessler, N. Rappaport, *J. Appl. Phys.* **2004**, *96*, 1083.

213 J. A. Barker, C. M. Ramsdale, N. C. Greenham, *Phys. Rev. B* **2005**, *67*, 075205.

214 C. L. Braun, *J. Chem. Phys.* **1984**, *80*, 4157.

215 C. J. Brabec, J. C. Hummelen, R. A. J. Janssen, N. S. Sariciftci, *Synth. Met.* **1999**, *102*, 861.

<QA>15. References 178, 199, 252, 264 / Please update these references, if possible.

216 H. Sirringhaus, T. Kawase, R. H. Friend, T. Shimoda, M. Inbasekaran, W. Wu, E. P. Woo, *Science* **2000**, *290*, 2123.

217 C. J. Brabec, N. S. Sariciftci, J. C. Hummelen, *Adv. Funct. Mater.* **2001**, *11*, 15.

218 S. E. Shaheen, R. Radspinner, N. Peyghambarian, G. E. Jabbour, *Appl. Phys. Lett.* **2001**, *79*, 2996.

219 G. Dennler, N. S. Sariciftci, *Proc. IEEE* **2005**, *93*, 1429.

220 T. Mäkelä, S. Pienimaa, S. Jussila, *Synth. Met.* **1999**, *101*, 705.

221 T. Granlund, T. Nyberg, L. S. Roman, M. Svensson, O. Inganäs, *Adv. Mater.* **2000**, *12*, 269.

222 Y.-H. Tak, C.-N. Kim, M.-S. Kim, K.-B. Kim, M.-H. Lee, S.-T. Kim, *Synth. Met.* **2003**, *138*, 497.

223 G. Dennler, C. Lungenschmied, H. Neugebauer, N. S. Sariciftci, A. Labouret, *J. Mater.Res.* **2005**, *20*, 3224.

224 U. Akimasa, K. Susumu, *Patent US6168968*, **2001**.

225 J. Morgado, R. H. Friend, F. Cacialli, *Synth. Met.* **2000**, *114*, 189.

226 D. G. J. Sutherland, J. A. Carlisle, P. Elliker, G. Fox, T. W. Hagler, I. Jimenez, H. W. Lee, K. Pakbaz, L. J. Terminello, S. C. Williams, F. J. Himpsel, D. K. Shuh, W. M. Tong, J. J. Lia, T. A. Callcott, D. L. Ederer, *Appl. Phys. Lett.* **1996**, *68*, 2046.

227 H. Y. Low, *Thin Solid Films* **2002**, *413*, 160.

228 R. D. Scurlock, B. Wang, P. R. Ogilby, J. R. Sheats, R. L. Clough, *J. Am. Chem. Soc.* **1995**, *117*, 10194.

229 B. H. Cumpston, I. D. Parker, K. F. Jensen, *J. Appl. Phys.* **1997**, *81*, 3716.

230 S. Kumar, A. K. Biswas, V. K. Shukla, A. Awasthi, R. S. Anand, J. Narain, *Synth. Met.* **2003**, *139*, 751.

231 L. M. Do, E. M. Han, Y. Nidome, M. Fujihira, T. Kanno, S. Yoshida, A. Maeda, A. J. Ikushima, *J. Appl. Phys.* **1994**, *76*, 5118.

232 M. Schaer, F. Nüesch, D. Berner, W. Leo, L. Zuppiroli, *Adv. Funct. Mater.* **2001**, *11*, 116.

233 H. Neugebauer, C. J. Brabec, J. C. Hummelen, N. S. Sariciftci, *Sol. Energy Mater. Sol. Cells* **2000**, *61*, 35.

234 G. D. Hale, S. J. Oldenburg, N. J. Halas, *Phys. Rev. B* **1997**, *55*, 16069.

235 S. Shuller, P. Schilinsky, J. Hauch, C. J. Brabec, *Appl. Phys. A* **2004**, *79*, 37.

236 T. Jeranko, H. Tributsch, N. S. Sariciftci, J. C. Hummelen, *Sol. Energy Mater. Sol. Cells.* **2004**, *83*, 247.

237 F. C. Krebs, J. E. Carlé, N. Cruys-Bagger, M. Andersen, M. R. Lilliedal, M. A. Hammond, S. Hvidt, *Sol. Energy Mater. Sol. Cells* **2005**, *86*, 499.

238 J. M. Kroon, M. M. Wienk, W. J. H. Verhees, J. C. Hummelen, *Thin Solid Films* **2002**, *403-404*, 223.

239 Y. Sahin, S. Alem, R. De Bettignies, J.-M. Nunzi, *Thin Solid Films* **2005**, *476*, 340.

240 C. J. Brabec, F. Padinger, N. S. Sariciftci, J. C. Hummelen, *J. Appl. Phys.* **1999**, *85*, 6866.

241 J. S. Lewis, M. S. Weaver, *IEEE J. Select. Topics Quantum Electron.* **2004**, *10*, 45.

242 A. S. da Silva Sobrinho, M. Latreche, G. Czeremuszkin, J. E. Klemberg-Sapieha, M. R. Wertheimer, *J. Vac. Sci. Technol. A* **1998**, *16*, 3190.

243 Y. Leterrier, *Prog. Mater. Sci.* **2003**, *48*, 1.

244 A. S. da Silva Sobrinho, G. Czeremuszkin, M. Latreche, G. Dennler, M. R. Wertheimer, *Surf. Coat. Technol.* **1999**, *116–119*, 1204.

245 G. Dennler, A. Houdayer, Y. Ségui, M. R. Wertheimer, *J. Vac. Sci. Technol. A* **2001**, *19*, 2320.

246 G. Russi, M. Nulman, *J. Appl. Phys.* **1993**, *74*, 5471.

247 A. S. da Silva Sobrinho, G. Czeremuszkin, M. Latreche, M. R. Wertheimer, *J. Vac. Sci. Technol. A* **2000**, *18*, 149.

248 J. D. Affinito, M. E. Gross, C. A. Coronado, G. L. Graff, E. N. Greenwell, P. M. Martin, *Thin Solid Films* **1996**, *290/291*, 63.

249 J. D. Affinito, M. E. Gross, P. A. Mournier, M. K. Shi, G. L. Graff, *J. Vac. Sci. Technol. A* **1999**, *17*, 1974.

250 M. S. Weaver, L. A. Michalski, K. Rajan, M. A. Rothman, J. A. Silvernail, P. E. Burrows, G. L. Graff, M. E. Gross, P. M. Martin, M. Hall, E. Mast, C. Bonham, W. Bennett, M. Zumhoff, *Appl. Phys. Lett.* **2002**, *81*, 2929.

251 A. B. Chwang, M. A. Rothman, S. Y. Mao, R. H. Hewitt, M. S. Weaver, J. A. Silvernail, K. Rajan, M. Hack, J. J. Brown, X. Chu, L. Moro, T. Krajewski, N. Rutherford, *Appl. Phys. Lett.* **2003**, *83*, 413.

252 G. Dennler, C. Lungenschmied, H. Neugebauer, N. S. Sariciftci, M. Latrèche, G. Czeremuszkin, M. R. Wertheimer, *Thin Solid Film*, in press.

253 N. C. Greenham, X. Peng, A. P. Alivisatos, *Phys. Rev. B* **1996**, *54*, 17628.

254 A. P. Alivisatos, *Science* **1996**, *271*, 933.

255 D. S. Ginger, N. C. Greenham, *Phys. Rev. B* **1999**, *59*, 10622.

256 X. Peng, L. Manna, W. Yang, J. Wickham, E. Scher, A. Kadavanich, A. P. Alivisatos, *Nature* **2000**, *404*, 59.

257 L. Manna, E. Scher, A. P. Alivisatos, *J. Am. Chem. Soc.* **2000**, *122*, 12700.

258 W. U. Huynh, J. J. Dittmer, A. P. Alivisatos, *Science* **2000**, *295*, 2425.

259 Z. A. Peng, X. Peng, *J. Am. Chem. Soc.* **2002**, *124*, 3343.

260 B. Sun, E. Marx, N. C. Greenham, *Nano Lett.* **2003**, *3*, 961.

261 B. Sun, H. J. Snaith, A. S. Dhoot, S. Westenhoff, N. C. Greenham, *J. Appl. Phys.* **2005**, *97*, 014914.

262 E. Arici, H. Hoppe, F. Schäffler, D. Meissner, M. A. Malik, N. S. Sariciftci, *Appl. Phys. A* **2004**, *79*, 59.

263 E. Arici, D. Meissner, N. S. Sariciftci, *Adv. Funct. Mater.* **2003**, *13*, 165.

264 S. Günes, H. Neugebauer, N. S. Sariciftci, J. Roither, M. Kovalenko, G. Pillwein, W. Heiss, *Adv. Funct. Mater., in press*.

265 K. M. Coakley, M. D. McGehee, *Appl. Phys. Lett.* **2003**, *83*, 3380.

266 C. Y. Kwong, A. B. Djurisic, P. C. Chui, K. W. Cheng, W. K. Chan, *Chem. Phys. Lett.* **2004**, *384*, 372.

<QA>15. References 178, 199, 252, 264 / Please update these references, if possible.

<QA>15. References 178, 199, 252, 264 / Please update these references, if possible.

267 P. A. van Hal, M. M. Wienk, J. M. Kroon, W. J. H. Verhees, L. H. Slooff, W. J. H. van Gennip, P. Jonkheijm, R. A. J. Janssen, *Adv. Mater.* **2003**, *15*, 118.

268 W. J. E. Beek, M. M. Wienk, R. A. J. Janssen, *Adv. Mater.* **2004**, *16*, 1009.

269 W. J. E. Beek, L. H. Stooff, M. M. Wienk, J. M. Kroon, R. A. J. Janssen, *Adv. Funct. Mater.* **2005**, *15*, 1703.

270 O. Stenzel, S. Wilbrandt, A. Stendal, U. Beckers, K. Voigtsberger, C. von Borczyskowski, *J. Phys. D* **1995**, *28*, 2154.

271 F. Stietz, J. Bosbach, T. Wenzel, T. Vartanyan, A. Goldmann, F. Träger, *Phys. Rev. Lett.* **2000**, *84*, 5644.

272 S. Hayashi, K. Kozaru, K. Yamamoto, *Solid State Commun.* **1991**, *79*, 763.

273 D. M. Shaardt, B. Feng, E. T. Yu, *Appl. Phys. Lett.* **2005**, *86*, 63106.

274 M. Westphalen, U. Kreibig, J. Rostalski, H. Luth, D. Meissner, *Sol. Energy Mater. Sol. Cells* **2000**, *61*, 97.

275 M. S. Dresselhaus, G. Dresselhaus, P. C. Eklund, *Science of Fullerenes and Carbon Nanotubes.* Academic, New York, **1996**.

276 H. Ago, K. Petrisch, M. S. P. Shaffer, A. H. Windle, R. H. Friend, *Adv. Mater.* **1999**, *11*, 1281.

277 H. Ago, M. S. P. Shaffer, D. S. Ginger, A. H. Windle, R. H. Friend, *Phys. Rev. B* **2000**, *61*, 2286.

278 E. Kymakis, G. A. J. Amaratunga, *Appl. Phys. Lett.* **2002**, *80*, 112.

279 E. Kymakis, I. Alexandrou, G. A. J. Amaratunga, *J. Appl. Phys.* **2003**, *93*, 1764.

280 Z. Wu, Z. Chen, X. Du, J. M. Logan, J. Sippel, M. Nikolou, K. Kamaras, J. R. Reynolds, D. B. Tanner, A. F. Hebard, A. G. Rinzler, *Science* **2004**, *305*, 1273.

281 A. du Pasquier, H. E. Unalan, A. Kanwal, S. Miller, M. Chhowalla, *Appl. Phys. Lett.* **2005**, *87*, 203511.